Sustainability and degradation of chemical deicers in the Gardermoen Aquifer

Iron and manganese redox processes

Andrea Waade

Thesis submitted for the degree of
Master in Environmental Geosciences
60 credits

Geosciences
Faculty of mathematics and natural sciences

UNIVERSITY OF OSLO

Spring 2022

Sustainability and degradation of chemical deicers in the Gardermoen Aquifer

Iron and manganese redox processes

Andrea Waade

Abstract

Oslo Airport is situated above the Gardermoen Aquifer, which is Norway's largest unconfined aquifer. During the winter season the airport uses the deicing chemicals propylene glycol for airplanes and potassium formate for runways. The airport follows strict governmental guidelines to ensure no long-term changes occur to the groundwater so that it may be preserved for future use. The area along the western runway is an important area of study because of the shallow groundwater table and the higher loads of deicing chemicals in this area. Monitoring wells along the western runway have found increased levels of manganese and iron compared to reference wells outside the airport. These increased levels indicate the role of manganese and iron oxides as terminal electron acceptors in the degradation of deicing chemicals.

The goal of this research study is to determine the sustainability of deicer usage by analyzing how manganese and iron oxide dissolution and precipitation processes are affected by seasonal changes to the redox state. Additionally, this research study seeks to answer what the likely flow pathways are along the western runway and if vertical flow in the saturation zone is a probable pathway. This work uses field data from four boreholes that were drilled in June 2020 by Avinor along the western runway. Two of the boreholes are multilevel wells (ML1 and ML2) that were drilled to a depth of 26m and included three filters. Data collection in the field was done between June 2020 and April 2022 and consisted of sediment sampling, groundwater sampling and hydraulic head measurements.

Grain size analysis of the boreholes shows the heterogeneity of the sediment from the foreset unit of the Gardermoen aquifer. The hydraulic head data shows that there are no confining units. Temperature and water chemistry analysis of the three filters of each multilevel well show that there may be an area of low-flow between Filter B and C in the two wells, which is between approximately 12.5m and 23.5m depth.

Oxalate extraction and diathonite-citrate-bicarbonate (DCB) experiments were conducted to determine the amount of amorphous and crystalline iron oxides in the aquifer with respect to distance from the western runway. The results of the experiment show that the average amorphous iron oxide content in the unsaturated zone is between 0.2-0.3 g/100g dry sediment and there is not a significant difference with respect to distance from the runway. Total manganese oxide content was found to be 0.01 g/100g dry sediment in the unsaturated zone 167 meters downgradient from the runway (ML2) compared to 0.002 g/100g dry sediment for the well 11m downgradient from the runway (ML1). This indicates that amorphous iron may be able to re-precipitate at a fast enough rate that in the saturated zone and along the water table there is not noticeable depletion relative to the sampled borehole further from the runway. The lower concentration of amorphous manganese oxides nearer to the runway may be due to the higher concentration of deicers infiltrating in this area.

The seasonal input of deicers near the runway create variable redox conditions that affect the precipitation and dissolution dynamics of iron and manganese. Chemical speciation calculations in PHREEQC indicate that there are periods in late summer and early fall when it may be favorable for ferrihydrite to precipitate in the aquifer despite highly reducing conditions observed in the summer. Sediment analysis with a scanning electron microscope (SEM) show iron oxide precipitate on grains in the unsaturated zone and along the water table. The iron precipitate observed in SEM was primarily crystalline iron and not the more

readily available amorphous iron oxide in both ML1 and ML2. Speciation calculations show that manganese oxide is not likely to precipitate and was not observed with SEM.

The sustainability of using the unsaturated zone as an attenuation zone is also dependent on rainwater and snow melt infiltration patterns. The relationship between infiltration and seasonal dissolved iron and manganese was analyzed for season 2020-2021 using historical water chemistry data from Avinor. The highest levels of dissolved iron and manganese were related to likely infiltration periods of deicing chemicals. During this year, higher levels of dissolved iron and manganese were found 44m downgradient of the runway and there was a reduction to background levels approximately 115 meters downgradient from the runway. This season was warmer than usual and there was less chemical deicer usage than normal.

The overall sustainability of electron acceptors was modeled using a PHREEQC equilibrium model. The model simulated the amount of iron and manganese that is reduced following a pulse injection of chemical deicers using previously observed concentrations. The results of this model indicate that deicers have the potential to quickly reduce the electron acceptor pool of amorphous iron over the course of 16.8 years if the amorphous iron is not able to re-precipitate.

Acknowledgment

Contents

List of Figures

List of Tables

Chapter 1

Introduction

The field study was conducted at Gardermoen International Airport (OSL), which is located in Northern Romerike. OSL is situated in the recharge area of the Northern Romerike Aquifer, which is the largest unconfined aquifer in Norway. The Norwegian government requires the aquifer to remain a potential source of drinkable water for the future. The Northern Romerike Aquifer (also called the Gardermoen Aquifer) includes protected landscapes, including ravines in the south-west and kettle hole lakes in the north-west. For these reasons, Oslo Airport is legally obligated to not alter the groundwater chemistry of the aquifer.

Oslo Airport uses large quantities of deicing chemicals on airplanes and runways during the winter season. The airport uses propylene glycol ($C_3H_8O_2$) and potassium formate ($KCHO_2$) for deicing purposes. Propylene glycol (PG) is used to deice airplanes prior to take-off which occurs along one of OSL's three deicing platforms. Approximately 80% of all PG that is used is drained from the platforms and further treated [Hansen et al., 2020a]. During take-off, the propylene glycol that remains on the plane will disperse into the air and deposit in the soil along the runways. Potassium formate is used to deice runway platforms. Clearing of snow along the platforms results in the spreading of formate up to approximately 40 meters from the runway [Hansen et al., 2020a].

Oslo Airport is allowed to use the unsaturated zone for attenuation of deicing chemicals [Wejden and Øvstedal, 2006]. Numerous monitoring wells are located throughout the airport and outside the airport boundary to monitor potential effects of deicing chemicals on groundwater chemistry. OSL monitors for both potential changes to groundwater chemistry and so that it does not violate threshold concentration limits for chemical deicers. Exceeding such limits on chemical deicer concentrations outside the airport boundary will result in a large fine for the airport [Hansen et al., 2020a].

OSL's "Grunnvann 2030" project has the objective of studying the sustainability of deicing chemicals usage given the goals for the groundwater reserve. Determining the sustainability of deicer usage is particularly important since there has been a large increase in airport traffic and use of deicing chemicals over the past 20 years. During the winter seasons 2017-2018 and 2018-2019 there was an almost doubling in the usage of deicing chemicals [Hansen et al., 2020a]. The effect of climate change on weather patterns may also play a role in the increase in deicer usage [French, 2008].

This research study focuses specifically on degradation processes of deicers along the western runway. The area along the western runway is an area of concern for Oslo Airport since it has the most flight traffic and it also has a shallow groundwater table. The shallow groundwater table means that there is less time in the unsaturated zone for deicing chemicals to degrade. Groundwater near the western runway shows heightened levels of iron, manganese and potassium compared to control wells.

1.1 Objectives

The aim of this study is to analyze iron and manganese dissolution and precipitation processes to better understand the sustainability of deicer usage. Iron and manganese oxides and hydroxides are important electron acceptors in the soil and thus are essential to degradation of deicers in the unsaturated and saturated zone. Depending on the redox conditions in the soil and groundwater these metals may dissolve or precipitate. A high redox potential indicates that the dissolved iron and manganese will precipitate and low redox potential leads to the reduction and dissolution of these metals in the groundwater.

This research study includes analysis of water and sediment from four boreholes drilled in the summer of 2020. Two of the boreholes are multilevel wells. The first well was drilled approximately 11m downgradient of the runway while the second was drilled approximatley 167m downgradient. The wells both include three filters which allow for the observation of changes in water chemistry with depth. The total manganese and iron in sediments samples is determined with XRF and further mineral analysis is conducted with XRD. Quantification of the amount of iron and manganese oxide is done with dithionite-citrate-bicarbonate (DCB) and oxalate extraction experiments. Quantification of the amount of electron acceptors available provides insight into the sustainability of chemical deicers usage in the aquifer. A PHREEQC speciation model calculates the saturation index of minerals. The effect of adding deicers on the reduction of iron and manganese oxides is evaluated with a PHREEQC reaction model.

Hydraulic head data from the two wells and grain-size analysis are used to analyze flow patterns in the area along the western runway. Flow patterns indicate how chemical deicers may travel through the groundwater. Oslo Airport is located along a groundwater divide, which causes vertical flow pathways near the divide. Vertical flow could transport chemical deicers deeper into the aquifer where they are less likely to be degraded [Hansen et al., 2020a].

This research study seeks to answer the following questions for the area along the western runway at Oslo Airport:

1. What are the likely groundwater flow pathways along the western runway?

2. How do chemical deicers affect iron and manganese reduction and precipitation processes?

3. Is chemical deicer infiltration sustainable in the long term given the availability of manganese and iron electron acceptors?

Chapter 2

Background

2.1 Study Area

2.1.1 Geographic Location

The location of the study area is in the Northern Romerike region in south-eastern Norway, approximately 60km north-east of Oslo. The data was collected at the Gardermoen International Airport, which is located at the border of the Nannestad and Ullensaker municipalities. Oslo Airport sits atop the Gardermoen Aquifer. The study location can be shown in Figure 2.1, which is along OSL's western runway.
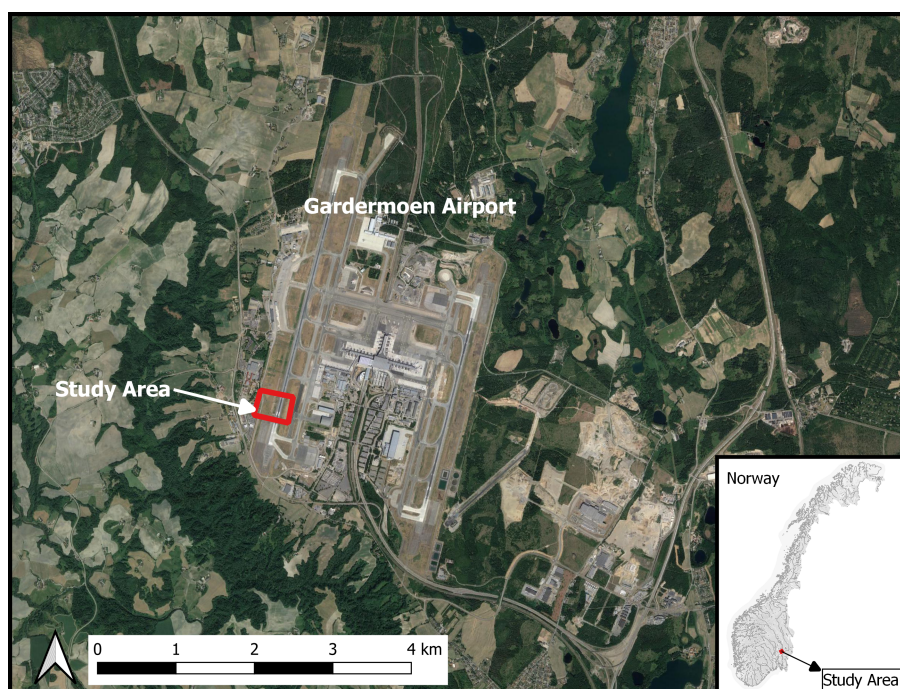
Figure 2.1: Geographic location of the study area along the western runway at Oslo Airport (Google Earth).

Sampling Locations

The data in this thesis is based on water and soil samples from 4 boreholes named BR29-ML1, BR29-ML2, BR29-JordC and BR29-JordB (referred to in this study as ML1, ML2, JordB and JordC, respectively). Two of the boreholes BR29-ML1 and BR29-ML2, are multilevel wells. The soil samples were collected between June 8th-15th, 2021 and water samples were collected in August and November of 2021. The locations of wells is seen in Figure 2.2.
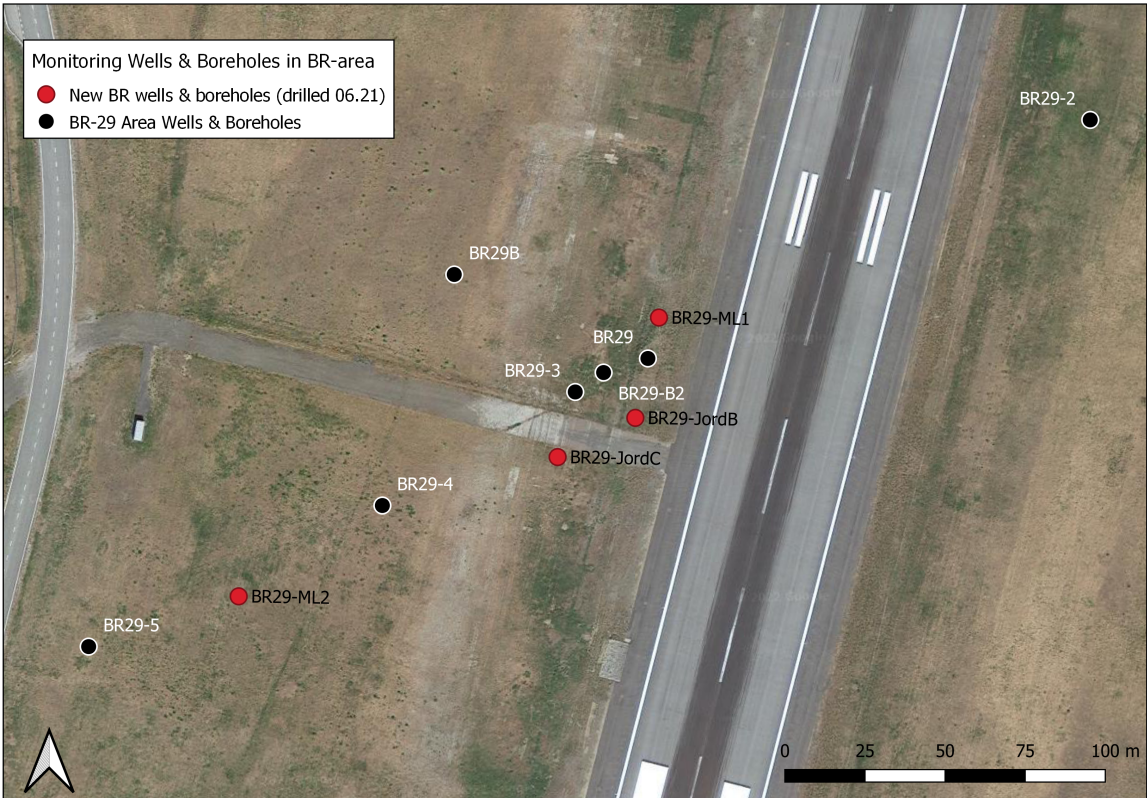
Figure 2.2: Position of the multilevel sampling wells in the research study, BR29-ML1 and BR29-ML2, and boreholes BR29-JordC and BR29-JordB, in red. Additional monitoring wells near the western runway are shown in black (Google Earth).

2.2 Northern Romerike Aquifer

The Northern Romerike Aquifer (also called the Gardermoen Aquifer) is Norway's largest unconfined aquifer and it covers an area of approximately 100 km^2. The aquifer comprises of the Gardermoen Delta Complex [Tuttle et al., 1997]. The Gardermoen Delta was formed during the last ice age in Scandinavia. Precipitation and groundwater supply water to Lake Hersjøoen, which further drains into river Risa in the northern part of the aquifer. In the southwest, water flows through ravines, which feed the Sogna River. Groundwater-fed kettlelakes dot the landscape and are depositional features from deglaciation. Marine clays border the aquifer and provide an impermeable barrier (Figure 2.3). The bedrock below the aquifer is composed of the Eastern Norwegian Precarbian basement [Aagaard et al., 1996]. It is composed of 95% gneiss with the remaining granite-pegmatite. The gneises can be characterized as being predominantly plagioclase and quartz [Longva, 1987].

The aquifer has many different land-use types. There is a significant amount of agriculture within the aquifer and bordering it. The aquifer also contains forested lands, particularly in the central part of the aquifer. Oslo Airport, which opened in 1998, is located at the south-west portion of the aquifer (Figure 2.3).
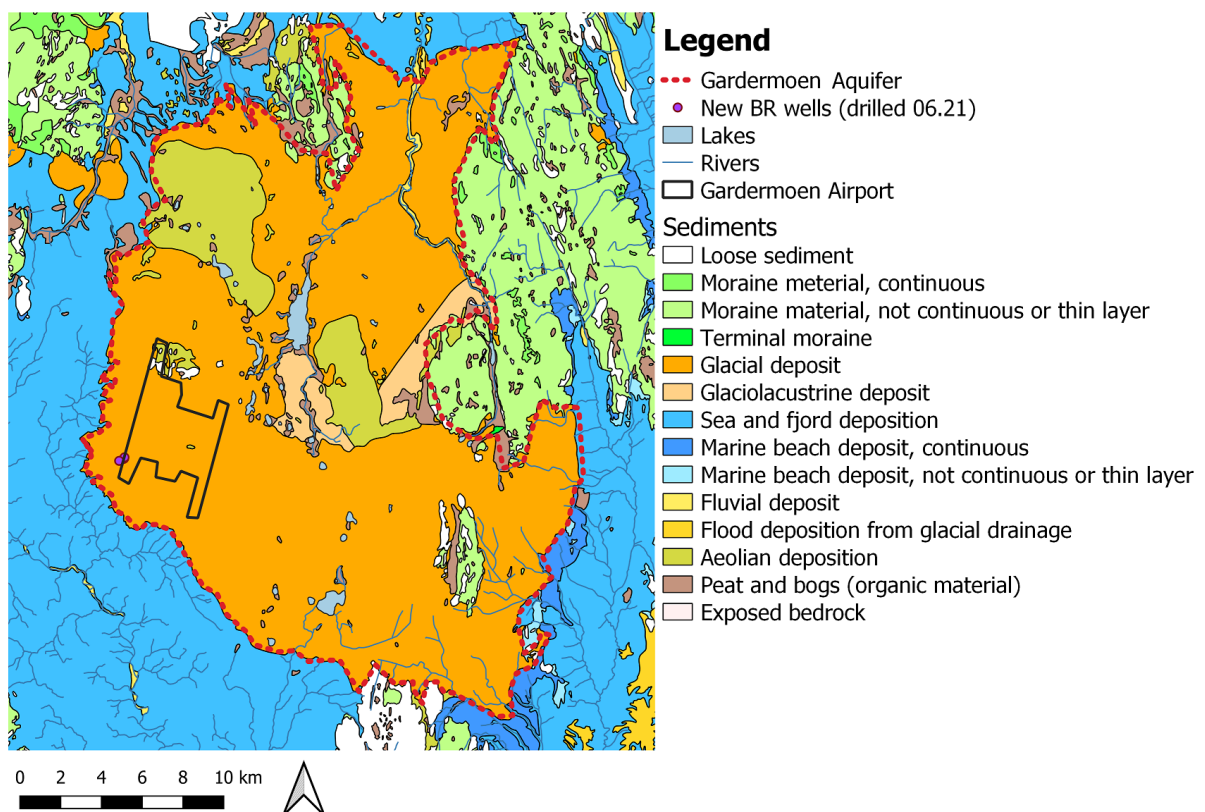
Figure 2.3: Sedimentary map showing the glacio-fluvial deposits that make up the Gardermoen Aquifer. The outline of Oslo Airport is shown in black and wells drilled in the study area along the south-western edge of the airport. Sedimentary dataset from NGU [of Norway , NGU].

2.2.1 Gardermoen Delta Complex

The Gardermoen Delta is an early Holocene ice-contact delta that developed in a marine fjordal basin around 9500 years BP [Tuttle, 1997]. The Gardermoen Delta is one of five ice-contact deltas that were deposited over a course of 400 years during the Weichselian deglaciation [Tuttle et al., 1997]. During this time, the Romerike fjord was undergoing rapid marine regression due to isostatic regional uplift [Tuttle et al., 1997, Longva and Thoresen, 1989]. The Gardermoen Delta Complex is the largest of the five ice-contact deltas. The formation of the Gardermoen Delta occured during melt-water discharge and high sedimentation rate. It is estimated that the Gardermoen Delta was deposited within a time span of 70 years [Tuttle et al., 1997]. The Gardermoen Delta consists of two main subdeltas, including the Trandum delta and the Li delta, with a total area of 79 km^2 (Figure 2.4). The deltas are generally coarser material, transported by high-energy glacial rivers (Figure 2.4). First-order channels from the final phase of delta deposition characterize the braidplain. The braidplain was unconfined and had a large channel network that spanned out in a 270°fan [Tuttle et al., 1997].

Stratigraphy

The delta can be divided into three units comprised of a topset, foreset and bottomset unit. These units are classified as a Gilbert type ice-contact delta-complex [Tuttle, 1997, Lønne, 1995]. The classification of these layers is based on studies of gravel-pit outcrops and ground-penetrating radar (GPR) technique [Tuttle et al., 1997].

The topset unit includes sand and coarse-grained deposits from subaerial braided rivers. The thickness of the topset decreases with distance due to less river energy from the melt-water channels in the distal parts of the aquifer [Jørgensen and Østmo, 1990]. Figure 2.4 shows this trend in the topset along an east-west cross section. The deposits are finer and more stratified in the distal areas [Tuttle, 1997]. The thickness of the delta top-set varies with respect to the distance from glacial meltwater portals. The topset is heterogeneous and is predominantly coarse material, including gravel and sand. It also contains finer material from channel backfill and overbank deposits [Kitterød, 2008].

The foreset unit contains submarine deposits from river mouth suspension fallout. This unit is influenced by meltwater channels and bedrock geometry. The foreset unit is composed of tilted beds, which dips between 15-30 degrees from the horizontal plane [Tuttle, 1997]. The composition of the foreset is around 95% fine sand with some sandy silt lenses [Kitterød, 2008]. Additionally, there is a small volume of gravel and sand with pebble and cobbles and decreasing grain size towards distal areas, where the study site is located [Tuttle, 1997, Kitterød, 2008].

The bottomset unit is composed of submarine and subhorizontal fine-grain sediment, including silt and clay. Additionally, this unit includes lenses of coarser-grained sediment which were deposited as fine-grained sediment due to suspension fallout from the river mouth. This unit also has some narrow beds with coarse-grained material that were deposited by gravity mass transport [Tuttle, 1997].
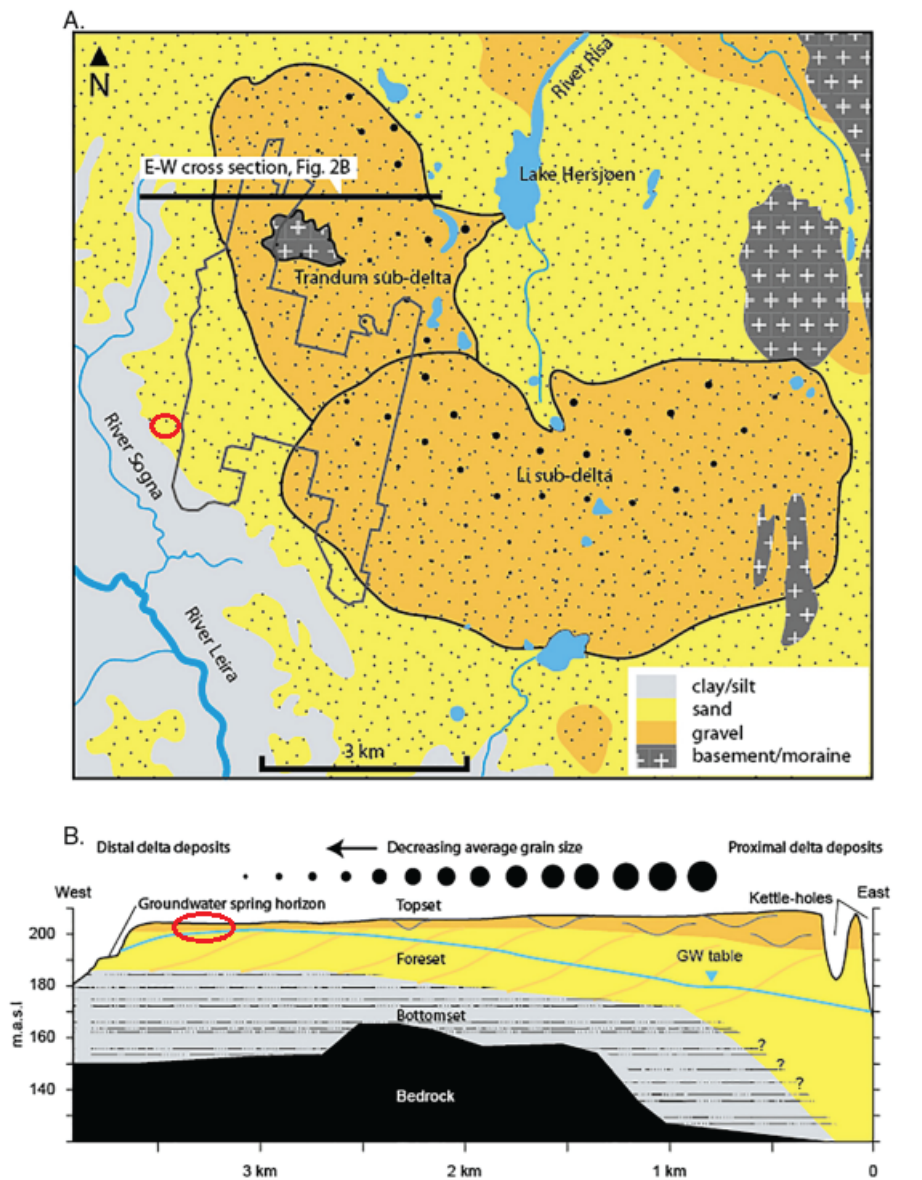
Figure 2.4: This figure is modified from Sundal et al. [2019] and based on a figure from Jørgensen et al. [1990].(A) A geological map of the Gardermoen aquifer which includes unconsolidated sediments deposited during the Holocene. Circled in red is the approximate location of the study site along the western runway. (B) E-W cross of the Gardermoen aquifer, with the location shown in Figure A above. The groundwater table is shown and decreasing grain size towards the distal area of the aquifer is shown. Circled in red is the projected location of the study site along the E-W cross section.

Hydrology

The Gardermoen Aquifer is unconfined and recharged by precipitation. Within the aquifer there is a groundwater divide that divides groundwater flowing either towards river Risa or towards ravines in the south-east that feed the Sogna River (Figure A.1). The drainage in the aquifer is dominated by outflow through the river Risa. Approximately 80% drains into Lake Hersjøen and River Risa in the north-east and 20% flows through south-west through the ravines [Jørgensen et al., 1990].

The depth to the groundwater table decreases with distance away from the groundwater divide and varies from 0 to 30 meters [Jørgensen and Østmo, 1990, Tuttle, 1997]. As shown in Figure 2.4, the deepest part of the groundwater table is located at Lake Hersjøen and the Risa river. At the location of the study site, the groundwater table is higher and flows towards the ravines [Tuttle, 1997].

Figure 2.5 shows the flow pattern at Oslo Airport and the groundwater divide. The groundwater divide is from the northwest to the southeast portion of the airport. At the groundwater divide the groundwater will move strongly in the vertical direction [Hansen et al., 2020b]. The yellow box in the figure shows the approximate location of the study site.
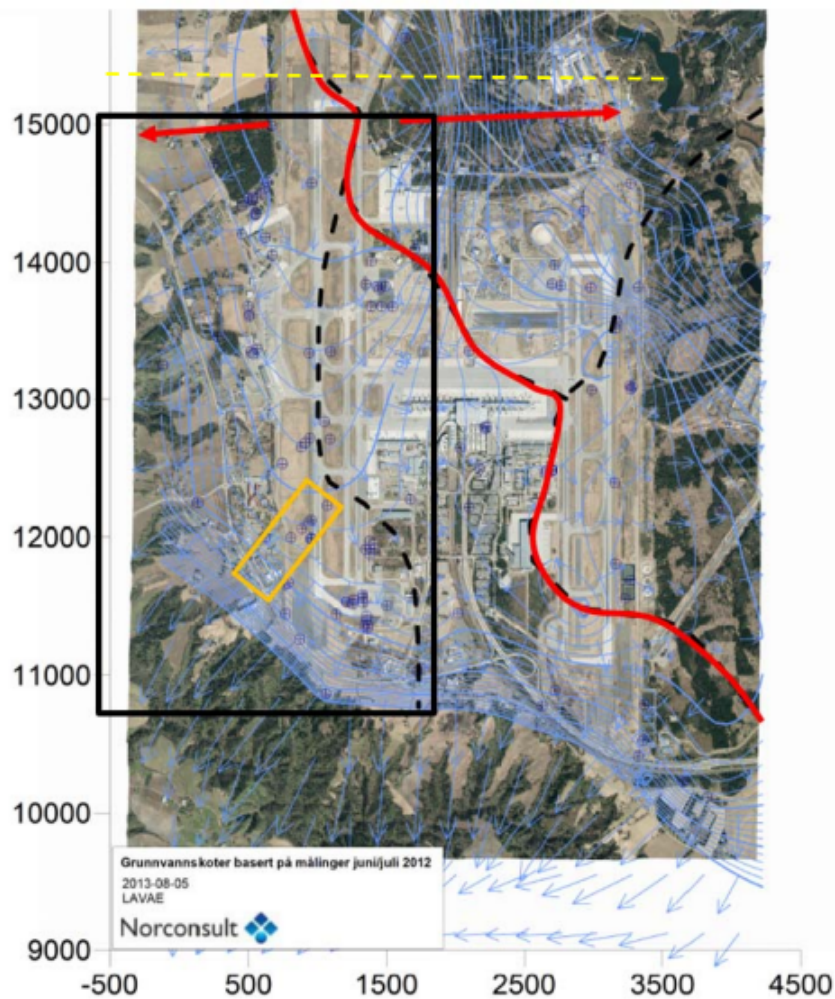
Figure 2.5: Figure from [Hansen et al., 2020b] shows groundwater flow patterns at Oslo Airport based on flow model by Nordconsult. The red line shows the groundwater divide and the yellow box shows the location of study site.

There are strict regulations from The Norwegian Water Resources and Energy Directorate (NVE) to uphold the water balance in the area. There is a tunnel below the groundwater table at Oslo Airport for the railway connected to the airport. The groundwater is pumped continuously underneath the continuously to ensure the water balance is maintained.

Water Budget

The water budget of Gardermoen Aquifer has previously detailed by Jørgensen and Østmo [1990]. The storage equation for the aquifer can be described by Equation 2.1. In this equation, precipitation (P) is the sum of evaporation (E), discharge (Q), subsurface drainage (D) and change in storage (ΔS).

$$P = E + Q + D + \Delta S \qquad (2.1)$$

Based on studies from between 1966-1974, the average annual precipitation is 794mm, including 508mm of rain and 250mm of snow Jørgensen and Østmo [1990]. Evapotranspiration is about 400mm [Jørgensen et al., 1990]. The remaining precipitation that has not evaporated is responsible for infiltration. The infiltration capacity of the sandy deposits is high and there is very little surface runoff [Jørgensen et al., 1990].

The aquifer recharge occurs primarily from snow melt (60%) which causes seasonal fluctuation in the groundwater level. During the winter, colder temperatures leads to the ground freezing and precipitation falling as snow. This causes the groundwater depth to sink during the winter. Snowmelt in the spring, caused by an increase in temperature and rain, causes a rise in groundwater. This rise in groundwater occurs approximately a month after snowmelt, over the course of 3 to 5 weeks [Jørgensen et al., 1990].

Discharge is fairly constant through the year and with an average value $0.85\text{m}^3\text{sec}^{-1}$ or the equivalent of 486mm based on the catchment area. Subsurface drainage is not possible to measure but is assumed to be much lower than discharge from the catchment.

A general residence time in the aquifer is approximately 30 years in the coarse-grained deposits and longer in fine-grained deposits [Jørgensen et al., 1990]. Thus, flow through the aquifer varies depending on the heterogeneous sediment characteristics in the aquifer.

Hydrostratigraphy

The water table is found in the tilted foreset beds and the topset unit is unsaturated [Basberg et al., 1998]. The unsaturated zone is the thickest in the eastern part of the aquifer, between 10-25 meters, compared to the western portion, 5-10 meters [Wejden and Øvstedal, 2006]. The study site is in the south-west where the water flows through finer-grained distal delta deposits to the ravines.

The hydrostratigraphy of the aquifer deviates some from the lithostigraphy [Tuttle, 1997]. There are four primary hydrostratigraphic units. There is a topset unit which contains coarser materials. This is followed by an upper foreset unit which contains the upper sandy unit. The lower foreset unit is silty-sandy and the percentage of silt and clay increases with depth. The lower foreset and bottomset units have similar hydraulic conductivities. The lower bottomset unit consists of silt and clay. The saturated zone contains the upper foreset, the lower foreset and the bottomset unit. The hydraulic conductivity generally decreases with depth and towards the increasingly fine sediments toward the distal areas.

The hydraulic conductivity in the aquifer generally decreases with depth. The topset unit has an average hydraulic conductivity of 10^{-3} to 10^{-4} [Tuttle, 1997]. The hydraulic conductivity generally decreases by at least an order of magnitude in each of the units [Sundal, 2006]. Hydraulic conductivity also decreases from the proximal to the distal parts of the aquifer given the changes in the sediment type. Figure 2.6 shows how the hydraulic conductivity changes
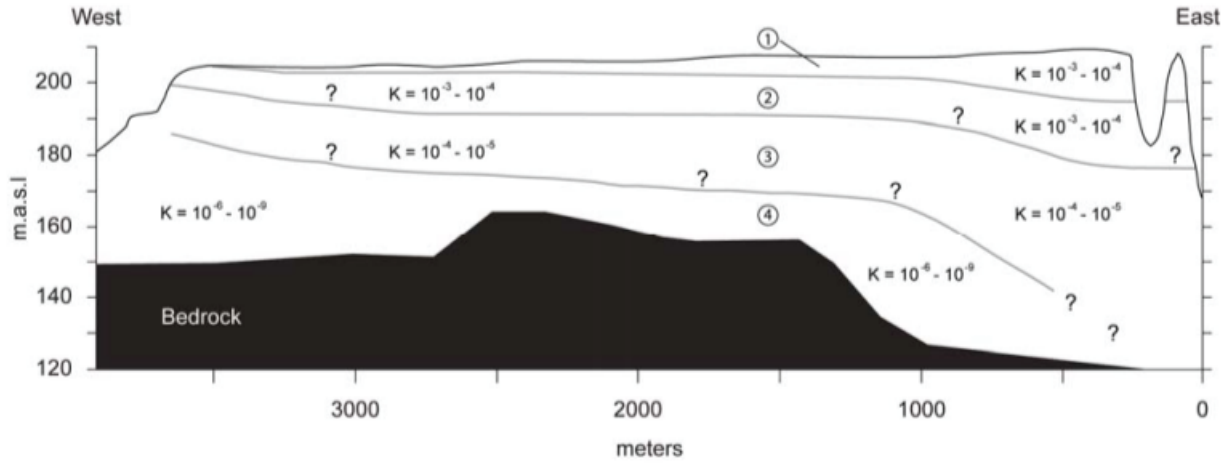
Figure 2.6: Hydrostratigraphic units from the Trandum Delta where K = hydraulic conductivity in m/s. The location of the E-W vertical cross section is shown in Figure 2.4. (1) is the topset unit, (2) is the upper foreset unit, (3) is the lower foreset unit and (4) is the lower bottomset unit. Figure is from Tuttle [1997] and modified by Sundal [2006].

along an E-W cross section that is drawn west of the southern tip of Lake Hersjøen. In this cross section from Sundal et al. [2019], hydraulic conductivity is at the highest nearer to Lake Hersjøen, with a value of 10^{-3} $\mathrm{m\,s^{-1}}$ and drops to 10^{-5} $\mathrm{m\,s^{-1}}$ along the west.

2.2.2 Gardermoen aquifer geochemistry

Water chemistry at Gardermoen is affected by both both mineral dissolution and rain water chemistry. Rainwater is generally low ionic strength. Previous rainwater studies near Gardermoen have found the rainwater to be acidic, with values between 4-6. Additionally, it is also affected by marine salts and farming. Previous downpour indicates rainfall is dominated of H^+, SO_4^{2-}, Na^+, Cl^-, NH_4^+, NO_3^- and also Ca^{2+}, Mg^{2+} and K^+ [Skarstad, 1996]. All the Na^+ and Cl^- was found to come from sea salt. Additionally, less than a quarter of K^+, SO_4^{2-} and Ca^{2+} come from sea salt. NH_4^+, H^+ and NO_3^- were entirely from other sources [Skarstad, 1996].

Previous analysis of sediment cores near Gardermoen have found the sediments to be predominantly composed of quartz [Dagestad, 1999] (Table 2.2). Additionally, hornblende (amphibole), micas, chlorite K-feldspar and plagioclase are important [Dagestad, 1999, Skarstad, 1996, Jørgensen et al., 1990]. Table 2.2 shows mineral assembleges based on previous experiments and modified from Dagestad [1999]. The study site Morepeen II has high content of plagioclase and micas in the sediment samples from Normoen is higher. Dagestad [1999] states that this may be due to the higher amount of finer sediments in this area.

ph	H^+	SO_4^{2-}	Na^+	Cl^-	NH_4^+	NO^{3-}	Mg^{2+}	Ca^{2+}	K^+
4.46	0.043	2.043	0.299	0.606	0.325	0.421	0.044	0.093	0.050

Table 2.1: Average rainwater compsition and pH for years 1990-1991 at Nordmoen from Skarstad [1996].

Location	Depth (m)	Amphibole	Mica	Chlorite	K-feldspar	Plagioclase	Quartz
Moreppen II	1-14	1	3	3	15	31	43
Moreppen I	1-8	1	2	6	8	18	65
Nordmoen	1-58	2	15	7	18	8	50

Table 2.2: Wt. % of minerals from locations at Gardermoen. Table modified from Dagestad [1999]. Nordmoen study from Jørgensen and Østmo [1990], Moreppen II study from Dagestad [1999] and Moreppen I study from Skarstad [1996].

Silicate weathering

The solubility of silicates is generally low. Chlorite $((Mg,Fe)_5(Al,Fe)_2Si_3O_{10}(OH)_8)$ provides the most Mg^{2+} and the dissolution of plagioclase-felspars such as anorthite $(CaAl_2Si_2O_8)$, provide Ca^{2+} ions to the water. Potassium is found in muscovite $(KAl_3Si_3O_{10}(OH)_2$ and biotite $(K(Mg,Fe)_3(AlSI_3O_{10})(OH)_2)$. Skarstad [1996] found a steady increase in potassium and showed that these ions dissolve throughout the profile. The dissolution of K-feldspar results in an increase in potassium and is shown in Equation 2.2. Plagioclase-feldspar, such as albite $(Na(AlSiO_8))$, will cause an increase in sodium.

$$2\,KAlSi_3O_8 + H_2O + 2\,H_2CO_3 \longrightarrow 2\,K^+ + 2\,HCO_3^- + Al_2Si_2O_5(OH)_4 + 4\,SiO_2 \qquad (2.2)$$
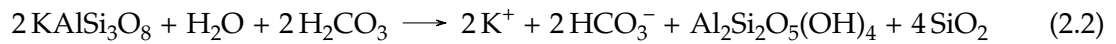
Pyrite

The sediments at Gardermoen have a significant amount of shale sediments that contain pyrite [Jørgensen et al., 1990]. Previous studies have found pyrite from 4 meters below the groundwater level [French, 2005]. Dagestad [1999] found pyrite in sediment from Nordmoen, which is north of Oslo Airport, and found that average pyrite is approximately 0.5 wt. %. between 19-58 meters at Nordmoen and approximately 1-1.5 wt % for Moreppen II.

Due to the oxidation of pyrite, the Gardermoen Aquifer has naturally lower oxygen levels [French, 2005]. Sulphide minerals, such as pyrite, generally have a low solubility. However, they are unstable in oxic environments or environments with ferric iron (Fe(III)) [Moses et al., 1987]. The oxidation of pyrite is also an important source of Fe(III) in the groundwater [Appelo and Postma, 2004].

The first step is the oxidation of pyrite, which can occur in two different pathways [Appelo and Postma, 2004]. The first pathway is by reacting with oxygen (Equation 2.3) and the second is by reacting with Fe(III) (Equation 2.4). The second pathway is more likely to take place in low pH conditions where Fe(III) remains in solution.

$$FeS_2 + \frac{7}{2}O_2 + H_2O \longrightarrow Fe^{2+} + 2\,SO_4^{2-} + 2\,H^+ \qquad (2.3)$$

$$FeS_2 + 14\,Fe^{3+} + 8\,H_2O \longrightarrow 15\,Fe^{2+} + 2\,SO_4^{2-} + 16\,H^+ \qquad (2.4)$$
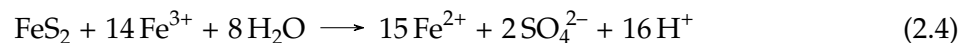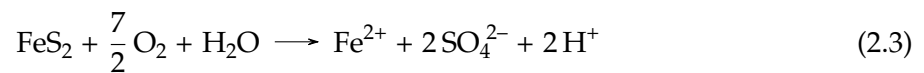
Both of the above equations indicate a significant decrease in pH. Following either pathway, Fe(II) can then be oxidized to Fe(III) following the reaction in Equation 2.5. This reaction takes place at a lower redox potential than for the reaction in Equation 2.3. Thus, in lower redox environments equation (Equation 2.5) will be less likely to occur, which will lead to a solution with increased levels of Fe(II) and SO_4^{2-} [Appelo and Postma, 2004].

$$Fe^{2+} + \frac{1}{4}O_2 + H^+ \longrightarrow Fe^{3+} + \frac{1}{2}H_2O \qquad (2.5)$$
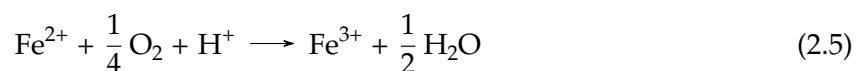
The Fe(III) which is produced by the reaction in Equation 2.5 is then likely to precipitate into iron oxides if the groundwater is not very acidic. This process is further discussed in subsection 2.3.4.

Calcite

Calcite is found in shale fragments at Gardermoen [Jørgensen et al., 1990]. Dagestad [1999] found calcite in the samples from Moreppen II and Normoen and found that there was an increase in calcite with depth. In sediment samples from Nordmoen calcite stabilized between approximately 2-2.5% around 20 meters depth. It was found that the amount of calcite increased to approximately 0.5 wt. % at 12 meters depth and a similar increase was found in sediment samples from Moreppen II at 8 meters depth. The slight increase in calcite shows the dissolution front of calcite in these areas.

The overall reaction for calcite dissolution follows three reactions (Equations 2.6, 2.7 and 2.8). Equation 2.8 quickly goes towards saturation and so Equation 2.6 and Equation 2.7 play the largest role in the groundwater chemistry.

$$CaCO_3 + H^+ \qquad\qquad = Ca^{2+} + HCO_3^- \qquad\qquad (2.6)$$

$$CaCO_3 + H_2CO_3 \qquad = Ca^{2+} + 2\,HCO_3^- \qquad\qquad (2.7)$$

$$CaCO_3 + H_2O \qquad\quad = Ca^{2+} + HCO_3^- + OH^- \qquad (2.8)$$
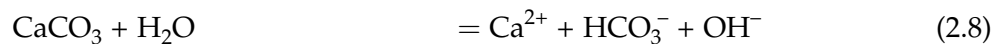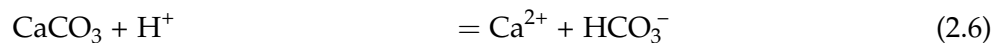
2.3 Chemical deicers and redox processes in the groundwater

2.3.1 Chemical deicer usage at Oslo Airport

The application of chemical deicers to planes and along runways is necessary during the cold winter climates in Norway. The two chemical deicers used include propylene glycol (PG) and potassium formate. Potassium formate is used to eliminate snow and ice from runways. The airport phased out acetate in 2001-2002 given the lower oxygen demand of potassium formate [Hansen et al., 2020a]. The amount of potassium formate used varies between season. The chemical deicer is usually applied between October-April. During the clearing of snow, potassium formate is spread approximately 40m from the runway [Hansen et al., 2020a]. Figure 2.7 shows the usage of formate for each season on the two different main runways at Gardermoen. The trend shows that there is a general increase in the usage. However, in the seasons 2020-2021 and 2021-2020 there was a reduction in the use of chemical deicers, due in part to significant cuts in air traffic during the COVID-19 pandemic.

Propylene glycol, also called 1,2-propanediol, is one of the most widely used chemical deicers in the world [Veltman et al., 1998]. It is an organic compound and at room temperature it is a colorless and viscous liquid (Figure 2.8). Propylene glycol (PG) is non-toxic and is used due to its ability to act as a freezing-point depressant and significantly lower the freezing point of water. Propylene glycol is applied in a solution to the aircraft using sprayers when deicing or removing snow. Additionally, propylene glycol may be reapplied for anti-icing purposes. The runoff from this is collected by Oslo Airport staff at their deicing platforms. However, during take-off some of this spreads into the air. Approximately 80% of the propylene glycol that is sprayed on planes is collected at the deicing platforms, which is either stored for future use or sent to treatment plants [French et al., 2010]. Approximately 10% remains on the plane and the remaining 10% is deposited below, alongside the runway [French et al., 2010].

The amount of propylene glycol used during each winter season varies and it is usually applied during the months of September through May. The maximum used during a season was 2017-2018 of 1,700 tonnes (Figure 2.7). Because propylene glycol is soluble in water it is
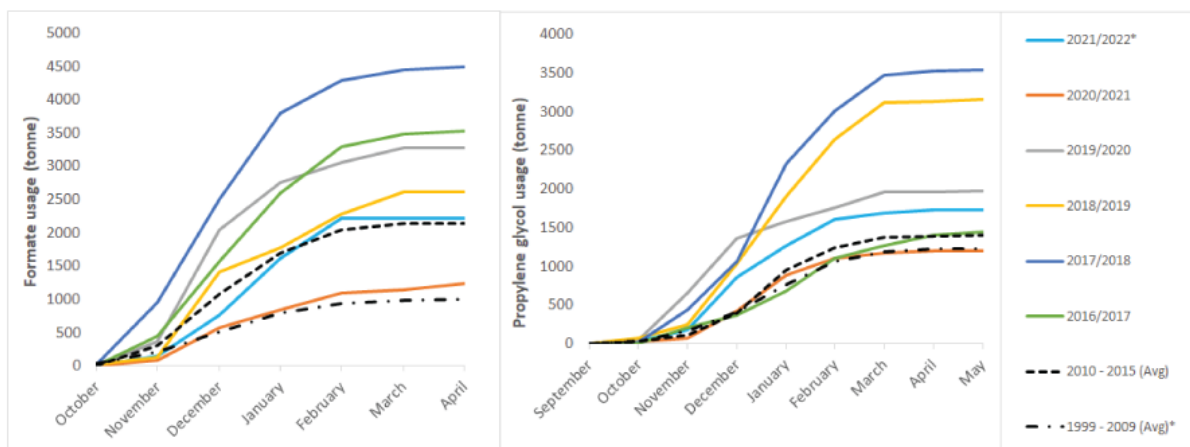
Figure 2.7: Cumulative monthly use of propylene glycol and formate at Oslo Airport, including both the western and eastern runways. A mean of years 1999-2009 and 2010-2015 is shown. *The season 2021-2022 is incomplete as it shows usage through April 20th and propylene glycol was still being used in small amounts at this time. *Propylene glycol reporting starts for season 1999-2000 and formate starts for season 2001-2002. This data has previously been reported in Hansen et al. [2020a]
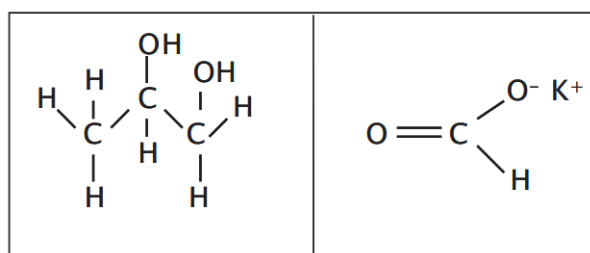
Figure 2.8: Chemical structure of propylene glycol (left) and potassium formate (right). Figure from Wejden and Øvstedal [2006].

easily transported in meltwater and groundwater [Wejden and Øvstedal, 2006]. Propylene glycol is considered degradable under both aerobic and anaerobic conditions [Wejden and Øvstedal, 2006]. It also has low octanol-water coefficient and therefore does not absorb to soil [French, 2008] .

Potassium formate is the potassium salt of formic acid (Figure 2.8). Formate is used along runways to clear snow and ice. Similar to PG, it works to significantly reduce the freezing point of water [Hellstén et al., 2005]. When the snow and ice is cleared it has shown to spread the chemical deicers a distance of up to 30 meters from the runway [Kraft and Roseth, 1999]. Similar to propylene glycol, formate is considered to be degradable under both aerobic and anaerobic conditions and it has a low octanol-water coefficient [French, 2008].

The highest use of deicing chemicals is when temperatures are between 0-2°C [French et al., 2010]. Figure 2.7 shows that there has been a significant increase in the PG usage for seasons 2017-2018, 2018-2019 and 2020-2021 . The formate trend fluctuates some but shows that usage between winter 2014 - winter 2019 were significantly higher than previous years. The increase is in part due to a new runway area in 2015 [French, 2005].

Oslo Airport has an agreement with the Norwegian Control Authority that the unsaturated zone may be used for attenuation of chemical deicers. It was assumed that biodegradation of chemical deicers in the unsaturated zone would be sufficient to protect groundwater from contamination [French et al., 2001]. If any PG or formate is detected in the groundwater at Oslo Airport, the airport uses extraction wells to remove the water [Wejden and Øvstedal,

2006]. While chemical deicers are not permitted to enter the groundwater outside the airport, detections of PG concentrations of 15mg/L are tolerated for short time periods.

2.3.2 Chemical deicer infiltration

The amount of chemical deicers that enter into the soil depends on temperature and permeability of the soil over the course of the winter season. The infiltration into the unsaturated zone has been monitored using field lysimeters and time-lapse electrical resistivity measurements [French et al., 2001]. During the winter season the air temperature remains around or below zero degrees. When the ground remains frozen over a long period of time, the chemical deicers build up in the snow and do not immediately infiltrate [French et al., 2001, Wejden and Øvstedal, 2006]. These chemicals infiltrate when the ground thaws in the spring. Previous studies have shown that there is rapid vertical flow during the first 3-5 weeks of snowmelt [French et al., 2010]. Meltwater can potentially move quickly through the unsaturated zone, especially if there are preferential flow pathways through the unsaturated zone. Since deicing chemicals melt more rapidly than snow they can infiltrate more rapidly into the unsaturated zone when the ground begins to thaw [French et al., 2010]. Studies have shown that over 90% of propylene glycol infiltrates into the ground [French et al., 2010]. The speed with which these chemicals move through the unsaturated zone is important to their ability to be degraded.

2.3.3 Degradation of chemical deicers

The concern with chemical deicers is that they could potentially alter groundwater chemistry if they do not degrade fully. The soil is vulnerable to concentrations of deicing chemicals and may have finite ability to degrade the chemicals [French et al., 2010]. The ability of the soil to degrade chemical deicers is dependent on many factors including residence time in the unsaturated zone, degradation rates, availability of electron acceptors and environmental conditions [French et al., 2010]. The thickness of the unsaturated zone and the amount of meltwater that enters into the unsaturated zone are both important risk factors [French et al., 2001]. Environmental conditions include temperature and pH levels. Chemical deicers are applied when the temperatures are negative or close to zero. The rate of degradation at these temperatures is reduced due to the colder temperatures [French and van der Zee, 2014].

The ability to degrade the chemical deicers depends on the availability of electron donors in the soil and groundwater. These processes are most often microbially mediated [Jakobsen and Postma, 1999]. Microorganisms will use the electron acceptor that provides the most energy and the highest redox potential. The general order of the electron acceptors in order of decreasing energy is O_2, NO_3^-, Mn^{4+}, Fe^{3+}, SO_4^{2-} and CO_2. The general order of electron acceptors follows Table 2.3. Not all redox zones are necessarily visible and redox zones can also overlap in aquifers [Appelo and Postma, 2004, Jakobsen and Postma, 1999]. The electron-transfer process allow microorganisms to grow and reproduce, which are inherently kinetic processes [Chapelle, 2000]. This is one reason determing redox conditions by assessing the pE can give an estimate of the redox conditions in the water but may not offer a complete understanding of the redox environment [Chapelle, 2000]. Studies have found that redox environment is complex and site-dependent [Petrunic et al., 2005].

The oxygen content in the unsaturated and saturated zone is dependent on different physical and geochemical factors. In the unsaturated zone, the flow of oxygen is governed by diffusive processes. When the depth of the unsaturated zone is thick, the travel time is usually long and organic matter will have more time to degrade [Appelo and Postma, 2004]. The permeability is also important because it effects the efficiency of diffusion. Once the oxygen is used up, additional anaerobic bacteria will take over. In the winter, when the ground is frozen, this reduces the oxygen that can be diffused.

14

Electron acceptor	Half-reaction	Eh
Oxygen	$O_2 + 4\,H^+ + 4\,e^- \longrightarrow 4\,H_2O$	>+ 100mV
Nitrate	$2\,NO_3^- + 12\,H^+ + 10\,e^- \longrightarrow N_2 + 6\,H_2O$	0 to 100mV
Manganese	$MnO_2 + 4\,H^+ + 2\,e^- \longrightarrow Mn^{2+} + 2\,H_2O$	0 to 100mV
Iron	$Fe_2O_3 + 6\,H^+ + 2\,e^- \longrightarrow Fe^{2+} + 3\,H_2O$	+100 til -100mV
Sulphate	$SO_4^{2-} + 9\,H^+ + 8\,e^- \longrightarrow HS^- + 4\,H_2O$	-100 to -300mV
Carbon dioxide	$CO_2 + 8\,H^+ + 8\,e^- \longrightarrow CH_4 + 2\,H_2O$	<-300mV

Table 2.3: Electron acceptors and half reactions. Data from Appelo and Postma [2004] and Hansen et al. [2020b].

In the saturated zone, the amount of oxygen present in the groundwater and the rate of flow is important [Lovley and Goodwin, 1988]. Groundwater generally carries oxygen within it if it has not been significantly affected by high levels of natural or anthropogenic sources of organic matter. If there is a source input into the groundwater, such as through chemical deicers during spring melt, redox zonation along the infiltration path can occur [Petrunic et al., 2005]. The next available electron acceptor will generally occur in order of decreasing energy. After oxygen is used up, nitrate is the next electron acceptor (Table 2.3). Nitrate has several different valences and its reduction series can be written as Equation 2.9 [Appelo and Postma, 2004].

$$NO_3^- \longrightarrow NO_2^- \longrightarrow N_2(g) \longrightarrow NH_4^+ \tag{2.9}$$

Where ammonium NH_4^+ is the most reduced form in the series. The electron acceptors continue in the order shown in Table 2.3.

Numerous studies have looked into degradation pathways and kinetics of propylene glycol [Veltman et al., 1998, Schoenberg et al., 2001]. Propylene glycol has a higher chemical oxygen demand (COD) than formate. The chemical oxygen demand is 1.68 g COD/g for propylene glycol. Degradation has been shown to occur at temperatures around -2°C [French et al., 2001]. The half-life of propylene glycol has been found to be 2.6 – 54 days shown to follow first-order degradation rates [French et al., 2001, French, 2008]. Although degradation of propylene glycol is possible in anaerobic conditions, its degradation is dependent on microorganism environment [Veltman et al., 1998]. Under anaerobic conditions, it will degrade to form acetate as an intermediate product before being fully degraded into methane (CH_4) and bicarobonate (HCO_3^-) (Equation 2.13).

$$\underset{\text{propyleneglykol}}{CH_3CH(OH)CH_2OH} \longrightarrow 0.5\,\underset{\text{propionate}}{CH_3CH_2COO^-} + 0.5\,H^+ + 0.5\,\underset{\text{n-propanol}}{CH_3CH_2CH_2OH} + 0.5\,H_2O \tag{2.10}$$

$$\underset{\text{n-propanol}}{CH_3CH_2CH_2OH} + 0.5\,H_2O \longrightarrow \underset{\text{propionate}}{CH_3CH_2COO^-} + H^+ + 2\,H_2 \tag{2.11}$$

$$\underset{\text{propionate}}{CH_3CH_2COO^-} + 3\,H_2O \longrightarrow \underset{\text{acetate}}{CH_3COO^-} + H^+ + HCO_3^- + 3\,H_2 \tag{2.12}$$

$$\underset{\text{acetate}}{CH_3COO^-} + H_2O \longrightarrow \underset{\text{methane}}{CH_4} + HCO_3^- \tag{2.13}$$
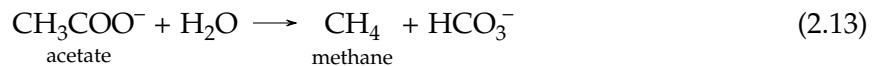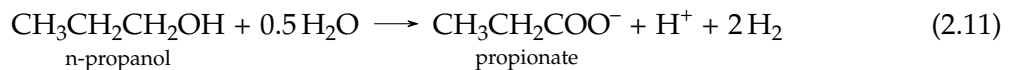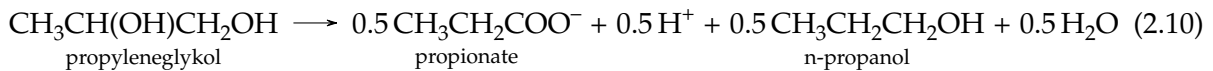
Potassium formate, which is the salt of formic acid, has a lower chemical oxygen demand (COD) of 0.35 g COD/g compared to PG. Potassium formate has a half-life of 2 - 34 days and
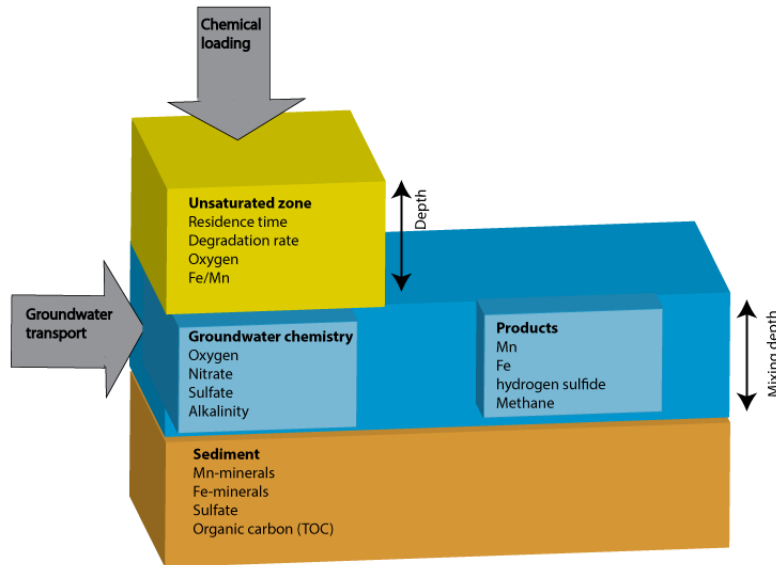
Figure 2.9: Schematic of box model created by Breedveld [2001] for the different degradation processes occurring in the unsaturated and saturated zone along the western runway at Oslo Airport.

has been shown to degrade under cold conditions [Hellstén et al., 2005]. Potassium formate has been found to be quickly degraded in the unsaturated zone and at low temperatures, between -2°C to +6°C in microcosm experiments [Hellstén et al., 2005]. The half-reaction of formate is shown in Equation 2.14.

$$KHCO_2 \longrightarrow K^+ + CO_2 + H^+ + 2\,e^- \tag{2.14}$$
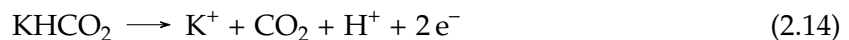
The degradation processes and geochemical conditions at Gardermoen have been modeled previously. Breedveld [2001] created a box model was used to include these differing processes. Threshold limits were determined between 1998-1999 for the western runway [Breedveld, 2001]. The calculations are based on how much chemical deicers can be degraded over the course of a year. These threshold limits vary with respect to groundwater depth. This box model found that along the western runway the degradation capacity was being exceed. However, previous analysis has shown that there is no long-term effect on chemical composition even though it is locally affected by short-term spill events [Wejden and Øvstedal, 2006].

2.3.4 Iron sources and reduction in groundwater

The effect of increased chemical deicers into the system has an important role on iron speciation in the system. When there is an absence of dissolved oxygen or nitrate, iron and manganese oxides may become the electron acceptors during anaerobic microbial decompositon (Lovley, 1997). Given that there is usually a high concentration of iron in sediments, it can often play a large role in the redox enivronment. Dissolved iron content is controlled by dissolution, precipitation and adsorption processes [Heron et al., 1994]. The speciation of iron depends on pH and Eh [Spiteri et al., 2006].

Iron is found in the soil as both primary and secondary (pedogenic) minerals. Iron is released during the weathering of primary minerals, which will then form secondary iron minerals [Cornell et al., 2003]. Dissolution of primary minerals is very slow and thus a rate limiting process [Appelo and Postma, 2004]. Once Fe(II) is mobilized following dissolution, its fate is primarily dependent on redox conditions and soil pH [Colombo et al., 2014]. Additional

16
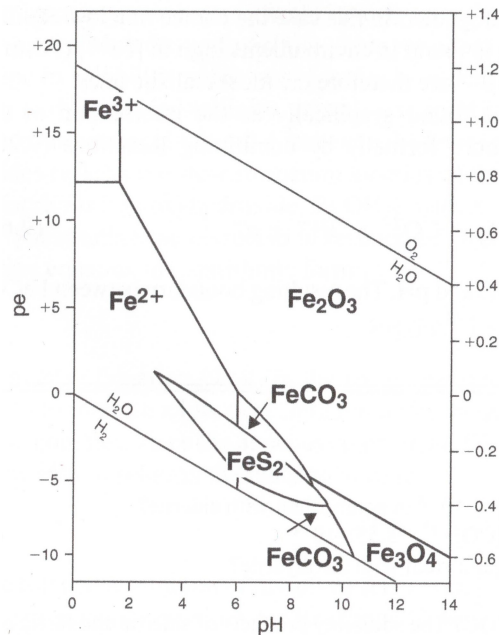
Figure 2.10: Iron stability diagram from Appelo and Postma [2004] at 25°C and TIC = 1M.

factors include moisture and temperature [Schwertmann and Taylor, 1989]. Under oxic conditions, iron oxides may be formed. Under reducing conditions, iron carbonates, sulphides and phosphates can also form [Cornell et al., 2003]. As the soil becomes more weathered, most of the iron from primary iron minerals is converted to secondary iron oxides [Appelo and Postma, 2004].

Iron exists in two oxidation states, Fe(II) and ferric (III). Iron oxidation occurs when electrons are transferred between Fe(II) to Fe(III). The stability of iron depends both the pE and pH (Figure 2.10). In oxic conditions with pH values between 5 and 8, Fe(II) will rapidly oxidize to Fe(III) and create iron precipitate (Equation 2.15). Oxidation of Fe(II) can occur both chemically or microbially. Under oxic conditions and neutral pH will Fe(II) spontaneously oxidize to Fe(III) and precipitate iron-oxyhydroxides (Equation 2.15).

$$Fe^{2+} + 3\,H_2O \longrightarrow Fe(OH)_3 + 3\,H^+ + e^- \tag{2.15}$$
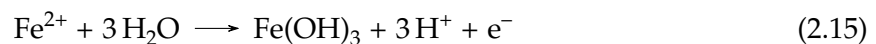
In anoxic conditions, Fe(III) is reduced by microbial processes or inorganic chemical reactions [Lovley, 1997a, Colombo et al., 2014]. The primary form of reduction is likely through microorganisms which can enzymatically induce these reactions [Lovley, 1997a]. The reduction of ferric iron Fe(III) to ferrous iron Fe(II) serves as an important electron acceptor in the sediment.

In sediment, Fe(III) often exceeds other electron acceptors, including including oxygen, nitrate and sulphate [Lovley and Phillips, 1986, Appelo and Postma, 2004]. The reduction of ferric iron from the degradation of organic material is another source of ferrous iron in the sediment [Lovley, 1997b]. Another important process is sulfidogenesis, where the precipitation of iron sulphide minerals, like pyrite, can sequester iron [Colombo et al., 2014]. In anaerobic conditions, this is one of the most common microbial reactions [Colombo et al., 2014].

Iron oxides make up a many minerals, from crystalline hematite to amorphous $Fe(OH)_3$. Over time, the less stable iron precipitates will recrystalize to iron minerals of higher stability [Boero and Schwertmann, 1989]. When the pH is acidic, the oxidation of Fe(II) to Fe(III) is not as fast. The effect of low pH can also give increased amounts of the reduced form of iron and manganese. Iron oxides in soil are of very small crystal size and low concentration [Cornell et al., 2003]. A mixture of iron oxides are found in aquifers due to slow dissolution kinetics

of stable phases [Appelo and Postma, 2004]. In the unsaturated zone, the formation of iron oxide varies greatly with the micro environments [Schwertmann and Taylor, 1989]. Iron oxides have a high specific surface area and their chemical nature allows iron oxides to be sorbents for inorganic ions and cations and also for organic anions and molecules [Schwertmann and Taylor, 1989].

Goethite is the most common iron oxide in soils due to its high thermodynamic stability [Cornell et al., 2003]. There are two primary ways goethite forms in soils. The first is if iron is released from ferrous Fe(II) iron minerals or following the microbial reduction of Fe(III)oxide. The ferrous iron will then become oxidized and form goethite crystals. The second way is for ferrihydrite to transfom into goethite. Ferrihydrite is much less stable compared to geothtite and has a poorly crystalline structure. Poorly crystalline (or amorphous) iron is reduced easier than crystalline oxides [Lovley and Phillips, 1986]. Research is still needed into the formation of iron oxides. It is still not certain to what extent ferrihydrite forms simulatenously with goethite or in sequence [Cornell et al., 2003].

Crystalline iron oxides, such as goethite, dissolve slowly and thus provide little iron for reduction [Colombo et al., 2014, Roden and Zachara, 1996]. However, in most soils and sediments, crystalline iron is often more abundant than amorphous iron [Colombo et al., 2014, Roden and Zachara, 1996].

2.3.5 Manganese sources and reduction in groundwater

Manganese in groundwater is most often the result of weathering from manganese bearing minerals. Manganese is found within oxides, carbonates, silicates, sulfides. Following dissolution, these minerals may then re-precipitate as hydroxides, oxides and carbonates [Aziz and Smith, 1992]. The majority of manganese in sediments is found as oxides. Manganese oxides are amorphous (poorly crystalline) minerals with large surface areas and act as strong oxidizing agents [Post, 1999]. They are typically black-brown and are located as coatings or intermixed masses on grains [Post, 1999]. There are many different types of manganese oxides. Some of the most common manganese oxides are listed in the Table 2.4 [Matsunaga et al., 1993, Post, 1999]. Birnessite is commonly found near the surface in aquifers [Matsunaga et al., 1993]. Birnessite transforms slowly to pyrolusite and dissolves easily. Rhodochrosite has been found following the microbial reduction of Mn(IV) and is the most common form of reduced manganese (Matsunaga et al. [1993]).

The thermodynamic stability of the manganese oxides and hydroxides is determined by such factors as pH, alkalinity, temperature and redox conditions [Lovley, 1995, Di-Ruggiero and Gounot, 1990]. Relationships between pH, redox potential and species present are complicated by the many number of redox states of manganese, which ranges from -III to +VII [Aziz and Smith, 1992]. The oxidation states +II, +III and +IV are the primary states in natural

Mineral	Chemical Formula
Birnessite	$(Na,Ca)Mn_7O_{14} \cdot 2.8\,H_2O$
Pyrolusite	MnO_2
Magnetite	$MnOOH$
Lithiophorite	$LiAl_2(Mn_2^{4+}Mn^{3+})O_6(OH)_6$
Hollandite	$Ba(Mn^{4+},Mn^{3+})_8O_{16}$

Table 2.4: Common manganese minerals and their forumals. Chemical formuals from [Post, 1999]
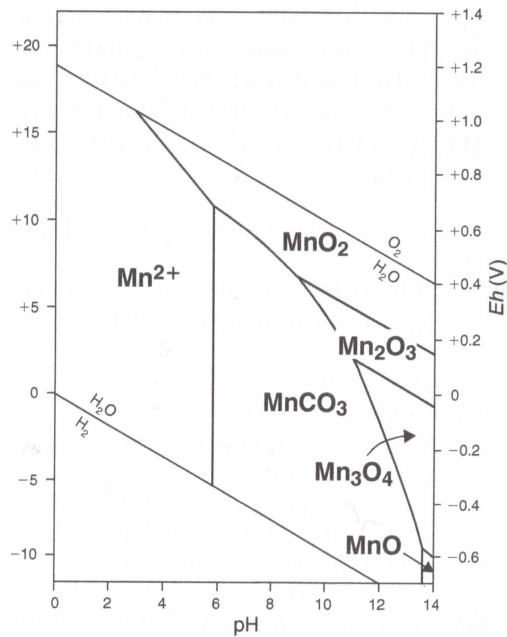
Figure 2.11: Manganese stability diagram from Appelo and Postma [2004] at 25°C and TIC = 1M

environments [Buamah et al., 2009]. At low pH and redox potential, Mn(II) is dominant and at high pH and high redox potential, MnO_2 (s) is dominant (Figure 2.11).

Oxidation of manganese is predominantly formed through microbially mediated pathways [Remucal and Ginder-Vogel, 2014, Dixon et al., 1990]. Oxidation of Mn(II) can either be the direct result of micro-organisms using the electron-acceptor Mn(IV) or an indirect process. Manganese is also slow to precipitate without catalysis. In conditions where oxidation and precipitation of Mn(II) is thermodynamically favored it could take years for the process to occur without catalysis [Martin, 2005, Gounot, 1994]. An increase from pH from 8 to 10 under oxic conditions for example will increase the rate and lead to faster precipitation of Mn(II).

When there are low quantities of oxygen in the groundwater, manganese and iron will dissolve more rapidly, especially when the pH is low [Khozyem et al., 2019]. Waters with high dissolved manganese are often used to indicate an environment that has either low or no oxygen concentrations [Appelo and Postma, 2004]. The mobilization of manganese in aquifers is often due to the dissolution of manganese oxides due to degradation activity [Khozyem et al., 2019]. Reduction of manganese oxides can can also take place from ferrous iron (Fe(II)) and sulphide [Lovley and Phillips, 1988, Breedveld, 2001]. In aquifers where redox conditions have develop downgradient of contaminant sources, the presence of manganese is used to map manganese-reducing zones [Jensen et al., 1998].

Previous studies near Oslo Airport at Moreppen show that manganese concentrations increase in both the soil and groundwater when there is an increase in the unsaturated zone degradation activity [French et al., 2001, French, 2008, French and van der Zee, 2014]. This is visible from a spill in 1999 from deicing chemicals and chemical processes in Figure 2.12 [Holm, 2000, Wejden and Øvstedal, 2006].

19
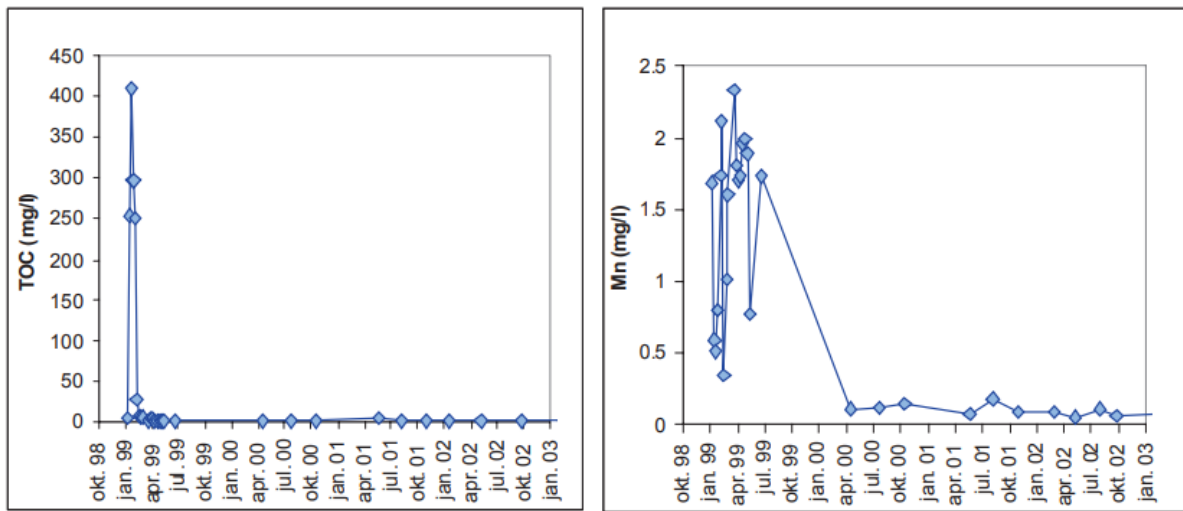
Figure 2.12: Spike in dissolved manganese following a chemical deicer spill at Oslo Airport in 1999, shown by spike in total organic carbon (TOC) levels. Figure from Wejden and Øvstedal [2006] and based on experiments by Holm [2000].

Chapter 3

Methods

3.1 Overview of boreholes and multilevel wells

The area of study near the western runway is often called the BR-area given the naming of first monitoring well, BR29, in the area. This area has been a focus of previous studies based on several factors. This area sits along the western runway, which is the most used runway at Oslo Airport. Thus, the frequent airplane traffic adds to the propylene glycol load in the area. Additionally, this area has a shallow groundwater table, at 2-8 meters below the surface [Hansen et al., 2020b]. The groundwater flow line is shown to go approximately NE-SW (Figure 3.1). The BR29 wells along the western runway can be seen to be located near this groundwater flow line. The topography between BR29-2 and the airport road to the SW is shown in Figure 3.1. The topography in this area is close to 200 m.a.s.l and has a slight increase from 199 m.a.s.l to 202 m.a.s.l.

The distance of these wells with respect to the groundwater flow line from the runway is provided in Table 3.1. Well ML1 is shown to be the closest well downgradient of the runway and ML2 is second to the furthest away from the runway at 167m. The location of the airport boundary is located along a fence west of the airport road in Figure 3.1, at a distance of 281 meters downgradient of the western runway.

The location where the four boreholes used in this research study were placed was determined based on groundwater flow and proximity to the runway. BR-ML1 (referred to as ML1) was placed close to the runway and along the groundwater flow line of several of the other BR29 wells. BR29-ML2 (referred to as ML2) was placed further along the groundwater flow path. ML2 was placed far enough away to not disrupt air traffic along the western runway when it was being sampled. Figure 3.2 shows the general proximity of the wells to the runway. The two boreholes, JordB and JordC, were placed slightly outside the flow path of the other wells.

Well	Distance (m)
BR29-ML1	11
BR29	20
BR29-B2	34
BR29-3	44
BR29-4	114
BR29-ML2	167
BR29-5	216

Table 3.1: Distances of wells along western runway from the runway with respect to modeled groundwater flow line from Hansen et al. [2020b].
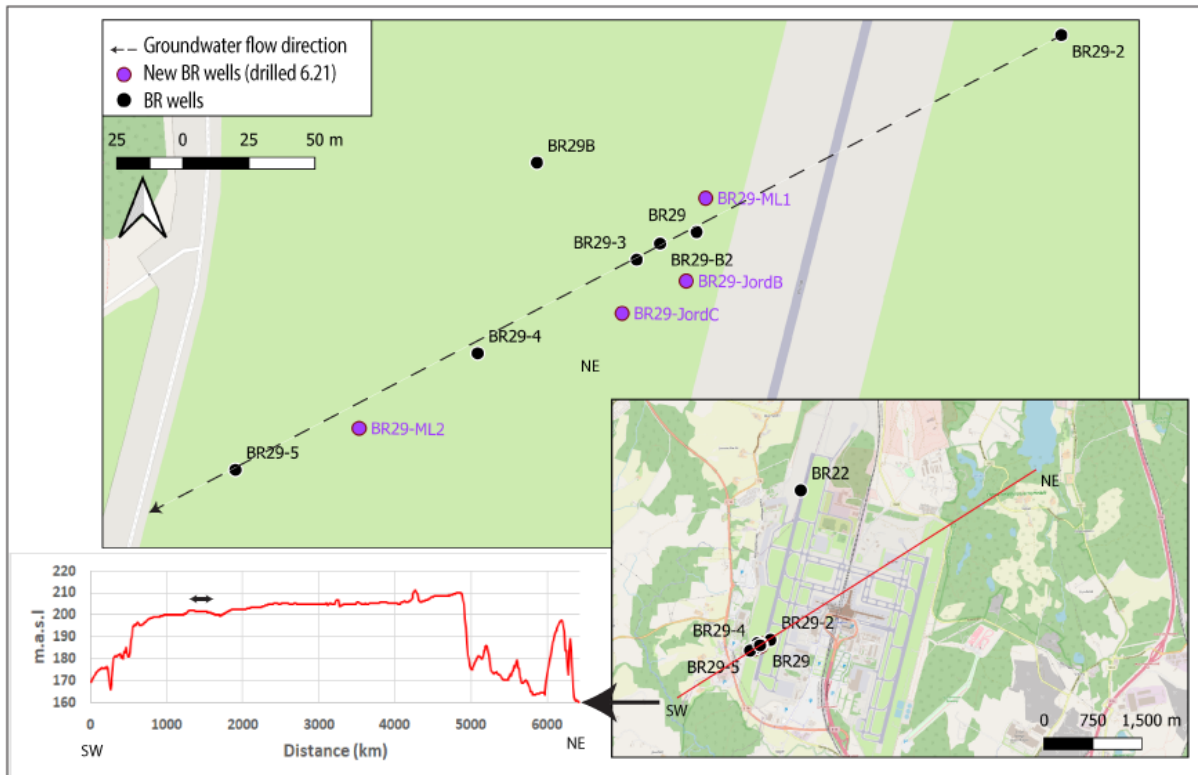
Figure 3.1: The groundwater flow path between wells along western runway and an extended cross section that matches the flow line. The top figure shows the approximated groundwater flow line between wells along the western runway based on previous groundwater modeling [Hansen et al., 2020b]. The bottom-right figures shows a cross section from the north-east at the bottom tip Lake Hersjøen to the south-west portion of the aquifer where the ravines are located. The bottom-left figure shows the topographic profile of the NE-SW cross section. The black arrow on this topographic profile shows the location and distance of the groundwater flow line in the top figure.

3.2 Borehole drilling

The borehole drilling was conducted between June 7th - 10th and June 14th - 15th, 2021. The first week was done during the night so as not to disrupt flight traffic. The final two days in the field were conducted during the day. Senior Adviser from the Norwegian Geotechnical Institute, Mona Hansen, coordinated and led the drilling work. The drilling was conducted by the company Brödrene Myhre. I was present on June 7th, 10th and 14th. I worked with Mona to determine a sampling method for the days I was not able to be present.

The wells were drilled using two different methods. In the uppermost soil layers, the drill rig was set up with an auger to bore into the earth (Figure 3.3a). Auger drilling is a common method for drilling. The benefit of using an earth auger is that samples are collected from the ground directly upon the auger. The auger sampling allows for more analysis of changes to soil physical features with depth and to take samples with a finer precision with respect to depth. It was noticed in some of the auger profiles that a thin layer of clay would coat the sediment. This layer would be carefully scraped off with a hand shovel prior to sampling. There are a few other potential problems with using the auger drill. In gravelly areas the larger rocks will not necessarily be brought up with the auger and may have instead fall off the drill. Additionally, the auger is more time intensive and is not able to bore through gravel and rock.

Each profile that was extracted on the auger was approximately 1 meter. Each meter was on average broken into 4 sampling sections. However, when clear sedimentary layers

(a) BR-ML1.

(b) BR-ML2.

Figure 3.2: Photos of wells ML1 and ML2 and the western runway in the background.

	Well ML1	Well ML2	JordB	JordC
Auger drilling depth(m)	8.4	14.5	14.5	7.2
ODEX drilling depth (m)	26	26	-	-

Table 3.2: Depth of ODEX and auger drilling for the four boreholes: ML1, ML2, JordB and JordC. Only the auger was used to drill JordB and JordC.

were apparent in the profile the sediment samples would reflect these. Thus, there is some variance in the depth that each sample reflects. Specific sedimentary layers were sampled when possible in order to provide more detailed characterization. Using the auger also allowed for more specific comparison with other physio-chemical changes in the sediment, such as redox conditions.

An ODEX drilling rig was used when the auger was no longer able to bore. The drilling depths for the boreholes are in Table 3.2. ODEX drilling is a method that uses an air powered hammer to force down a casing string. An ODEX casing can be driven through almost all soil and rockfill materials. During drilling, cuttings from inside the casing are carried to the surface using air. When the drill was used, the cores were sampled every meter by taking sediment that was brought to the surface by the rig (Figure 3.3b).

(a)   (b)
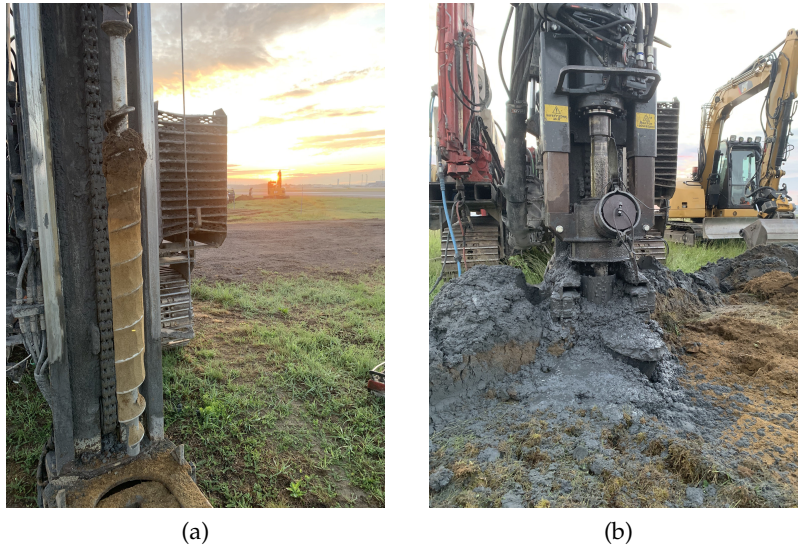
Figure 3.3: Photos of sample collection at the study site using (a) an auger drill and (b) the ODEX drilling rig.

3.2.1 Sediment characterization in the field

The sediment in the column was analyzed visually for changes to sediment grain size and soil coloration. The soil coloration provides the opportunity to visually interpret changes in iron oxide concentrations. Iron oxides can alter the color of the soil even at low concentrations [Schwertmann and Taylor, 1989]. Iron oxides are usually yellow or red [Heron et al., 1994]. Previous studies have shown different types of iron have different colors in the soil. However, when there is a mixture of different types of iron minerals in the soil it is not possible to differentiate them by color [Heron et al., 1994]. A change in concentration between tan to gray is also an indication that Fe(III) oxide coating on tan grains has been stripped [Lovley, 1997a]. The color profile of the soil was generally mapped into gray, tan and red layers in the soil. Variations in red layer color was not further analyzed for simplicity.

3.2.2 Sample storage

The samples were collected and placed in Rislan bags and zip-tied closed. The soil was stored in bags and refrigerated at the airport by Avinor and transported to a storage room at the Norwegian Geotechnical Institute (NGI) in Oslo in Sept. 2021. Sediment samples were analyzed between August 2021 - January 2022.

3.3 Sediment analysis

3.3.1 Sample selection for further analysis

An initial set of twenty sediment samples were chosen for additional laboratory analysis based on several initial criteria. Samples were chosen based on their depth and grain size. Additionally, samples were chosen from each of the three filter locations for both wells to compare with water chemistry analysis (Table 3.2). The well nearest the runway, ML1, had the most sample points of all four boreholes in order to get a more detailed vertical profile from the results. Additionally, a goal was to find similar grain sizes between wells to make sample comparison easier. Three approximately equally spaced samples were taken from ML1

in the unsaturated zone. Additionally, three samples from the top filter were chosen to see if there were any trends with respect to sediment above and below the water table. In addition, a sample from the location of each of the two lower filters from ML1 was included. For ML2, it was attempted to match the grain size of samples taken in ML1 with respect to depth. While eight initial samples were taken in ML1, only five were included in ML2. Three sample points were included from JordB and four from JordC. The sample points from JordB and JordC were chosen based on grain size with respect to depth and the sampling point grain sizes of the other boreholes.

The 20 initial soil samples were then used for additional chemical characterization, including XRD, XRF and TOC. A subset of these samples was used for SEM analysis and the extraction experiment. An overview of the sediment samples used for the different laboratory experiments is found in Table A.2.

3.3.2   Grain size distribution

Particle size distribution analysis is important for determining the percent of soil with a specific size fraction [Di Stefano et al., 2010]. There are several methods of determining grain size distribution. The method used in this study was to use manually sieve sediment to 0.5 mm and to use a diffraction analyzer for sediment smaller than this amount. The diffraction analyzer used in this study was the Beckman Coulter LS13 320.

Diffraction analyzers use laser-based technology to detect grain particle sizes between 0.4 µm-2000 µm. The method assumes that all particles are spherical. Sediment that is preferred for this method does not have a high amount of organics or salts. Previous studies have shown that the laser diffraction method (LDM) is a very reliable method for determining grain size distribution [Di Stefano et al., 2010, Goossens, 2008].

LDM is based on the idea that each grain size will diffract light at a specific angle [Loizeau et al., 1994]. Smaller particles have a high angle and large particles a low angle. The size distribution is determined through the cumulative scattering pattern from each sample. The scattered light is focused by a Fourier lens [Loizeau et al., 1994]. The Fourier lens creates a diffraction pattern of each particle based on the angle of light. There are 126 detectors measuring the patterns from the particles. An integrated pattern from all the particles is used to create subgroups based on size category. The amplitudes of each of these subgroups corresponds to the relative proportions of each of these particle sizes in the sample.

3.3.3   Sample preparation

To prepare samples for grain size analysis, the sample sediment was first homogenized. This was done by shaking the sediment bag to distribute the sample more evenly. Next, sediment was poured into a thin plate. The sediment was divided into four equal parts. Next, two equal parts diagonal to each other were removed. The remaining two parts were mixed and then divided into four parts and again the diagonal parts were removed. This process was repeated until the desired amount of material was attained.

The sample was then dried overnight at 60°C. Any plant residue was manually removed. Next, all samples were sieved down to 0.5 mm. The weight of the total material and the weight of sediment above and below a grain size of 0.5 mm was recorded and stored separately in a plastic beaker. All sediment above 0.5 mm was sieved manually. For sediment that was below 0.5 mm, the samples were prepared for diffraction analysis. No additional preparation was necessary for samples with an average size greater than 50 µm or without a significant amount of clay. Otherwise, the samples were diluted with distilled water and placed in plastic beakers. The plastic beakers were then placed in a freezer overnight. Next, the sample were freeze-dried and then weighed.

3.3.4 Grain size distribution analysis and interpretation

The diffraction analyzer produces a cumulative grain size curve for grain sizes for particle diameter up to (but not including) 500 µm and to grain sizes less than 2 µm. The grain size values used for the categorization of sediment size are from Blott and Pye [2001].

Sediment gradation

Based on grain size distribution, soils can be compared by three basic soil parameters [Das and Sivakugan, 2016]. The effective grain size (D_{10}) in a sample is the diameter that corresponds to 10% finer sediment. The uniformity coefficient (C_u) is determined from Equation 3.1. The coefficient of curvature (C_c) is shown in Equation 3.2, where D_{30} is the diameter corresponding to 30% finer. A well-graded soil has a uniformity coefficient that is greater than 6 for sands (4 for gravel) and a coefficient of gradation of between 1 and 3 for both gravels and sands [Das and Sivakugan, 2016].

$$C_u = D_{60}/D_{10} \tag{3.1}$$

$$C_c = (D_{30})^2/D_{60} * D_{10} \tag{3.2}$$

Saturated hydraulic conductivity estimation

Grain size distribution can be helpful in estimating saturated hydraulic conductivity (K_s) when it is hard to directly measure it in the field. A commonly used approximation is the Hazen formula which relates hydraulic conductivity to the effective grain size, D_{10} [mm] (Equation 3.3) ([Hazen, 1892]).

$$K = (D_{10})^2 * C \tag{3.3}$$

In Equation 3.3, C is the Hazen's emperical coefficient and has a value between 1 and 1.5 and the hydraulic conductivity (K) is in mm/s. The empirical coefficient C is dependent on such factors as grain size distribution. Hazen's formula is best suited for sands and gravels and may have a larger error with fine-grained sands [West and Shakoor, 2018].

3.3.5 Total inorganic and organic carbon

The percent organic and incorganic matter was determined by using an Organic Elemental Analyzer (CHNS/O). I prepared the sample for the CHNS/O and senior engineer, Mufak Said Naoroz, ran the samples in the CHNS/O. The CHNS/O works through a series of steps. The sample, which is wrapped in tin, first enters the combustion tube. The tube is set at a high temperature and includes catalytic material. When the tin sample crucible enters the tube, a set amount of oxygen is also injected. The tin triggers an exothermic oxidation reaction that causes the temperature to approximately 1800°C. At this temperature the sample fully combusts [Qian, 2000]. The products from combustion are sent through an oxidation zone where catalysts are oxidized. Through this process, elements are converted into N_2, CO_2, H_2O, and SO_2 gases. These gases flow into the chromatographic column where they are separated. The gases are then sent to the thermal conductivity detector (TCD) where the electrical signal is analyzed by software. This analysis can provide information about the percentage of nitrogen, carbon, hydrogen and sulfur in the sample.

Sample preparation

To prepare the sediment, the sample is first freeze-dried. Approximately 1 gram of the sediment is then pulverized using an agate mortar. To avoid contamination, the mortar is cleaned with

(a)   (b)
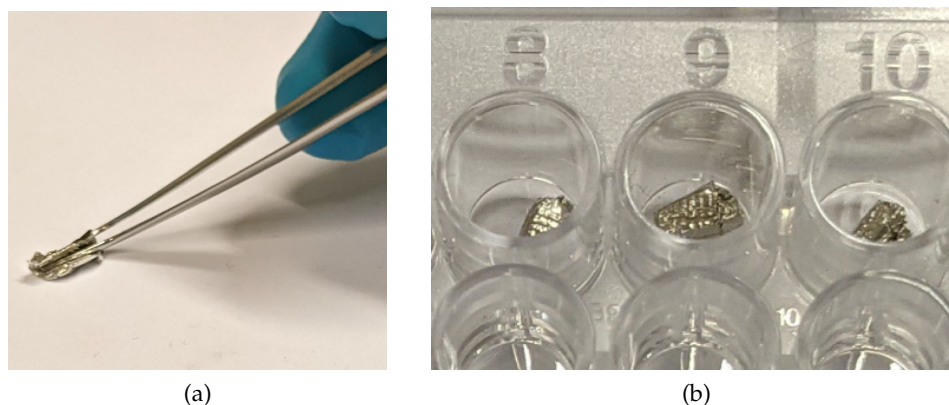
Figure 3.4: Sample preparation for Organic Elemental Analyzer. a) Folding the sample in a thin sheet. b) Samples folded in a thin tin sheet and ready for CHNS/O analysis.

ethanol between each use. Next, the sediment powder is transferred to a 50mL centrifuge tube and weighed. The inorganic carbonate (TIC) is removed by carefully adding 15mL of 1M Hydrochloric Acid (HCL). The solution is then mixed and left overnight. Next, the samples are centrifuged at 3000 rpm for 10 minutes. The acid solution is then decanted. Distilled water is added to the sample and mixed thoroughly. The sample is then centrifuged and decanted. The washing with water is repeated to remove the acid until the pH of the sample is above 5. The samples were then dried at a max temperature 40°C and weighed. The samples were again pulverized in an agate mortar and stored in a small glass container. The samples were carefully folded in a thin tin sheet (Figure 3.4). The samples were then ready to be analyzed by the CHNS/O.

3.3.6 Sediment composition imaging with SEM

A scanning electron microscope (SEM) was used to locate areas of iron and manganese oxide crystalline and amorphous iron. A second objective was to look for areas where the oxides were primary, or within the sediment itself, or precipitated as a coating on the sediment. The SEM analysis was done at the University of Oslo in the Geosciences Department with the assistance of Senior Engineer Siri Simonsen. The SEM is a Hitachi SU5000 variable pressure FEG-SEM that includes dual EDS (Energy Dispersive Spectroscopy), high-resolution EBSD (Electron Backscatter Diffraction) and a cathodluminescence (CL) system.

The SEM uses a high-energy electron beam to scan the surface of the sample. Several different types of signals are created from the interaction between the samples and electrons. Two signals that provide information on the imaging of samples include secondary electrons and backscattered electrons. Secondary electrons give information on surface structure, including the morphology and topography [Zhou et al., 2006]. Backscattered electrons provide information on surface structure and composition. Magnification can range from 5-300,000x. The detectors are set to detect the different energy levels produced by these signals [Nesse, 2012].

Prior to analysis, the samples were first dried overnight at 40°C. The samples were mounted on carbon tape. Six samples were selected from borehole ML1 and four from ML2. Sediment samples were selected for both above and below the water table.

3.3.7 Quantification of total iron and manganese with XRF

X-ray fluorescence (XRF) is a non-destructive technique that is used to analyze the specific elemental composition of samples. X-ray fluorescence is the emission of fluorescent X-rays

from material after it has been hit with X-rays. When the X-rays hits an atom with sufficient energy it can eject an electron from its inner shell. This results in an outer-shell electron dropping down to restore the original configuration [Brouwer, 2006]. This movement emits fluorescent radiation. The energy of radiation equals the energy difference between the two electron shells and it is unique for each element.

The spectrometer systems can be classified into two different groups, including the energy dispersive system (EDXRF) and the wavelength dispersive system (WDXRF) [Brouwer, 2006]. The primary difference between the two is in the detection system. In EDXRF, an X-ray tube irradiates a sample and the detector is able to directly measure the florescence radiation. The detector separates the fluorescence from the sample into radiation of the elements present. The main source of error with this method is the overlap of peaks. EDXRF instruments are used both in the lab and field and are used for the quick screening of elements.

The WDXRF system includes a diffraction crystal, a detector and a set of collimators (Figure 3.5a) [Brouwer, 2006]. The x-rays from the sample hit the crystal and the crystal then defracts different wavelengths in separate directions [Brouwer, 2006]. The detector is placed at specific angle where it can measure the intensity of the x-rays given a certain wavelength [Li et al., 2020]. If the angle is changed by moving the crystal and detector, it is possible to scan a wide spectral range and find which characteristic wavelength radiation comes out of the sample. The peaks are narrower and less overlapping. Thus, it is much more accurate and more sensitive than the EDXRF. The WDXRF is a standard test method for analysis in laboratories. The disadvantages of this method is that it is more expensive, complex and slower compared to the EDXRF.

This study uses both EDXRF and WDXRF systems. The samples were first analyzed with a field EDXRF at the Norwegian Geotechnical Institute (NGI) in Oslo. The instrument used was the Nitron XL3t GOLDD+ by Thermo Scientific. The instrument has been calibrated specifically for use with black shale. A known problem with the instrument after testing it at NGI is that it does not have a very reliable calibration curve for iron analysis. Thus, this instrument has a higher uncertainty with respect to iron. The instrument can be used on samples directly in the field. However, greater accuracy is achieved when the sample is ground to <250 micro meters. The use of a stand ensures that the instrument remains still when samples are taken and is safer given that the instrument emits radiation.

The prepared samples that were used for XRD were also used for analysis with the field EDXRF (Figure 3.6b). These samples, which were in glass holders, were covered with a thin sheet of plastic to avoid the sample falling out when it was turned upside down to be analyzed. The sample was tested by connecting the hand Nitron XL3t GOLDD+ instrument to a mobile test stand. The instrument and test stand was also connected to a laptop to both run the instrument directly and to access the data. The data was run under the category "Soils" from the menu settings. The analysis was repeated three times for each sample. Between each of the replicas, the sample was moved slightly, to account for any spatial heterogeneity in the sample. Additionally, a control sample was also run.

Four samples were additionally sent to be analyzed to the Bergmekanisk laboratory at the Norwegian University of Science and Technology (NTNU). At the laboratory, the four samples were sampled for major elements, including iron and manganese, by XRF. The instrument used was a PANalytical Zetium 4 kW X-ray spectrometer and the analysis was done by Torill Sørløkk. This instrument integrates the methods of EDXRF and WDXRF. The preparation of the samples was to crush the sediment with a high abrasion puck mill pulverizer for 3 minutes. The sediment did not include the final steps of adding ethanol and milling the sample, which was included in the field EDXRF and XRD preparation method.
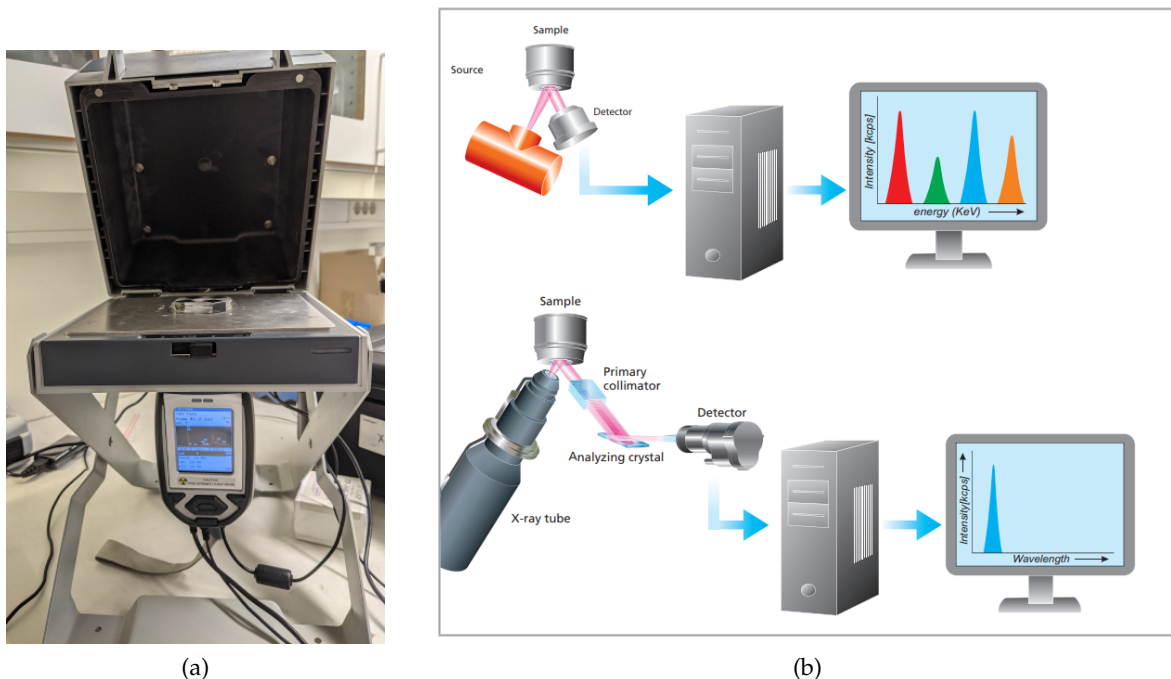
Figure 3.5: The field XRF connected to the mobile stand. The sample is shown placed on the stand prior to closing the lid and running the sample. b) The basic set-up for the EDXRF (top) and the WDXRF (bottom). The figure is taken from Brouwer [2006].

3.3.8 Quantification of crystalline iron and manganese with XRD

The quantification of crystalline iron and manganese was determined through X-ray diffraction (XRD). XRD is a non-destructive method to analyze sample material properties in the crystalline state. It can assess properties such as phase composition, structure and texture of the sample [Bunaciu et al., 2015]. X-ray diffractometers have three basic components, including an X-ray tube, a sample holder and a detector. In XRD, a monochromatic X-ray beam is produced by a cathode ray tube and directed towards a sample. The scatter from the crystals produces a regular array of spherical waves. Most of the waves cancel each other out but some are constructive, which is known as Bragg's law (Equation 3.4). Bragg's Law relates the wavelength of radiation x-rays (λ) to the diffraction angle (θ) and lattice spacing of the crystals (d) in the sample. An integer, n, is related to the order of diffraction.

$$2d \sin \theta = n\lambda \tag{3.4}$$

The angle between incident and scattered beam is 2θ. When the sample is scanned for a range of 2θ angles, the random orientation of the material allows for the determination of all diffraction directions of the lattice [Bunaciu et al., 2015]. The results of the XRD is called a defractogram. The x-ray diffraction pattern from the sample is then compared to a reference database.

Sample preparation

Samples used for XRD can vary between liquid, solid and powder. This study used the powder method. In this method the bulk sample is ground down to a powder. The benefits of this method include high sensitivity and reliability.

To prepare the sample, the sample was first dried overnight at 60°C. A high abrasion puck mill pulverizer was used to mechanically crush the samples. Before the samples were crushed,

29

(a)   (b)
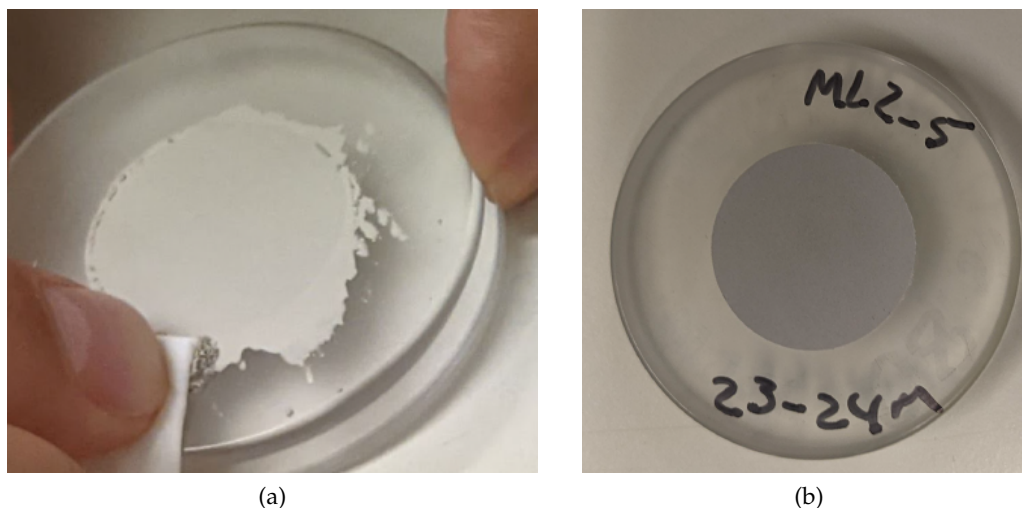
Figure 3.6: Sample preparation for XRD. (a) Smoothing the edge of the powdered sample (b) A powdered sample in glass holder that is ready for XRD analysis

the puck was cleaned to avoid any contamination. The puck was first wiped clean with ethanol and then quartz was milled for 10 minutes in the puck. Larger rocks were crushed with a hammer and then the sample was crushed for 3 minutes in the mill pulverizer. The puck was cleaned with ethanol between each sample and quartz was milled at the end of the analysis to reduce contamination.

The samples were then micronized in a McCrone micronizing mill. The samples were placed into a mill that includes 48 agate pellets. Additionally, 10mL of ethanol was added. Samples were milled for 10 minutes. They were then placed in an oven at 60°C to evaporate ethanol from sample. To reduce the samples to a powder, an agate mortar was used. The samples were smoothed with the edge of the holder using a thin glass plate (Figure 3.6). Once the samples were prepared, the samples were analyzed with XRD by Ibrahim Omar Khaled. The instrument was a Bruker D8 Advance XRD located in the Insitute of Geosciences at the University of Oslo. The samples were analyzed with the assistance of Lars Riber using the open source software Profex [Doebelin and Kleeberg, 2015] and Diffrac.EVA .

3.3.9   Iron and manganese extraction

Two different methods were used to determine the concentration of iron and manganese in the sediment. These two methods include the oxalate extraction method and the Dithionite Citrate Bicarbonate (DCB) procedure. The oxalate extraction method is used to estimate non-crystalline fractions and the DCB extraction is used to find both crystalline and non-crystalline iron and manganese.

Oxalate extraction background

The ammonium oxalate method extracts "amorphous" or also called "poorly crystalline" forms. Specifically, the method extracts X-ray amorphous hydrous oxides and microcrystalline ferrihydrite. It is a method which is commonly used on metals including iron, manganese and aluminum [Rennert et al., 2021]. The method of using oxalate to extract elements began approximately 100 years ago following a study by Tamm [1922] [Rennert et al., 2021]. This method was later advanced in the 1960s to differentiate between X-ray amorphous and crystalline iron oxides by [Schwertmann, 1964, Rennert et al., 2021]. The method is conducted in acidic conditions, where oxide surfaces are protonated with OH^- groups. This in turn

weakens the metal's bonds with oxygen. Then final step is for the metal to complex with the ligand oxalate and dissolve the metal oxide. The reason for focusing on amorphous iron is that these forms are generally be more reactive. In addition to dissolving non-crystalline forms of iron the the oxalate method also dissolves organically bound Fe, Al and Mn [Darke and Walbridge, 1994]. In addition, oxalate extraction has been found to dissolve the crystalline iron oxide magnetite (Fe_3O_4) [Darke and Walbridge, 1994].

There are several potential sources of error in this method. One of the issues with the reliability and reproducibility of oxalate extraction is that there is no universal standard for oxalate-extraction. Extraction methods often contain wide ranging differences, including soil to solution ratio, pH, extraction time and temperature [Rennert et al., 2021, Boero and Schwertmann, 1989]. Studies have found that the duration of the experiment can potentially dissolve crystalline oxide forms. Another factor is that given that oxalate also extracts organically bound metals, this can potentially overstate the concentration of oxides [Rennert et al., 2021]. Another variation is regarding whether or not to grind the sample in advance. It has been found that sample grinding increases efficiency and also allows for easier comparability between heterogeneous material. However, grinding the samples may also expose and extract trioctahedral clay minerals with the oxalate solution [Singer and Janitzky, 1986].

DCB extraction background

The DCB extraction dissolves organic matter iron oxides, non-crystalline and crystalline iron oxides [Darke and Walbridge, 1994]. Additionally, small amounts of iron bearing silicates may also be dissolved to a small degree [Darke and Walbridge, 1994]. In the procedure, a powerful reductant, dithionite, reduces iron oxides to soluble iron (II). A bicarbonate buffer is used to maintain a pH of 7 to 8 and to prevent the re-precipitation of Fe(II), sodium citrate is added. Similar to methods for oxalate extraction, there is no universal standard for the method. A source of error with the DCB extraction method is that it does not extract magnetite. While some studies recommend removing magnetite first, other studies have argued against this approach given that crystalline and amorphous iron coatings often form in or near magnetite grains [Singer and Janitzky, 1986, Walker, 1983].

Oxalate extraction procedure

The procedure follows the method outlined by the AgroEcoLab from the University of Maryland, which was based on methods by [Darke and Walbridge, 1994]. For each experiment, a blank and 3 repetitions were made. The basic procedure is outlined below. For step 1, all samples were sieved to 125 µm except one additional sample where the bulk material was ground to less than 125 µm. For step 3, reagents needed for the oxalte-oxalic acid solution include 0.2M ammonium oxalate ($C_2H_8N_2O_4$) and 0.2M oxalic acid ($C_2H_2O_4$). All reagents were stored in a dark environment. To prepare the oxalate-oxalic acid solution, 100mL of 0.2M ammonium oxalate was mixed with 75mL of 0.2M oxalic acid. The volume was altered with the fixed ratio depending on how much was needed for the full experiment. Next, the pH was tested. If it was greater than 3, oxalic acid was slowly pipetted to achieve a pH of 3. If the pH was less than 3, ammonium oxalate was added until the pH was 3. In step 7, a dilution series was created based on concentrations that were available. For step 9, a dilution series was created based on expected concentrations and concentrations ranges needed for ICP-MS analysis.

1. Dry sediment overnight at 60°C and sieve to 125 µm.
2. Weigh 0.4 g of the prepared sediment to a 50 mL centrifuge tube.
3. Prepare oxalate reagent and ensure pH is at 3.

4. Add 40 mL of the oxalate reagent to each tube.
5. Cap tubes and cover in tin foil and place in rack.
6. Shake with a mechanical shaker on high for 4 hours.
7. Centrifuge at 4000 rpm for 12 minutes or to clarity.
8. Decant supernatant into a 50 mL bottle.
9. Add 1 drop of 7M nitric acid (HNO_3).
10. Create a dilution series of samples.

To analyze the wt. % of iron and manganese in each sample, Equation 3.5 was used. In this equation, C_{Fe} is the concentration of iron determined by ICP-MS, $V_{solution}$ is the sample volume (0.04 L), M_{sample} is the initial mass of sediment added (0.4 g for oxalate experiment). This provides the mass of iron per 100 grams of sediment sample sieved to 125 µm. To find the the weight percent in bulk sediment, this concentration must be multiplied by the fraction of sediment by weight less than 125 µm.

$$\frac{C_{extracted\ solution} \left[\frac{mg}{L}\right] * V_{extracted\ solution} \left[L\right]}{M_{sample} \left[g\right]} * \frac{M_{sediment<125\,\mu m} \left[g\right]}{M_{bulk\ sediment} \left[g\right]} = C_{iron} \left[wt.\ \%\right] \quad (3.5)$$

DCB

The procedure follows the method outlined by the AgroEcoLab from the University of Maryland [AgroEcoLab, 2018], which was based on methods by Darke and Walbridge [1994]. In step 4, the reagents used for this expiriment were 0.1M sodium hydroxide (NaOH), 0.3M sodium hydroxide ($Na_3C_6H_5O_7$), 0.3M sodium citrate ($Na_3C_6H_5O_7$) and 1M sodium bicarbonate ($NaHCO_3$). To make the citrate-bicarbonate solution, a 4 to 1 ratio of sodium citrate to sodium bicarbonate was made. For step 5, the time for shaking the sample was modified from 16 to 18 hours based on the initial trial experiment. In step 8, the supernatant was decanted under a fume hood.

1. Dry sediment overnight at 60°C and sieve to 125 µm.
2. Weigh out 0.8 g of prepared sediment into a 50 mL centrifuge tube.
3. Add 0.8 g of solid $Na_2S_2O_4$.
4. Prepare citrate-bicarbonate solution.
5. Add 40 mL of the citrate-bicarbonate solution.
6. Cap tubes and shake on high for 18 hours.
7. Centrifuge for 20 minutes or to clarity.
8. Decant supernatant into a 50 mL bottle.
9. Add 1 drop of 7M nitric acid (HNO_3).
10. Create a dilution series of samples.

To analyze the wt. % of iron and manganese in each sample, Equation 3.5 was used. The initial mass of the sediment, M_{sample}, was modified to 0.8 g.

3.4 Groundwater monitoring

3.4.1 Placement of filters

Both ML1 and ML2 are multilevel wells and include 3 filters (Table 3.3). The placement and length of the filters was based on several monitoring objectives. The other wells in the BR-area have a single filter that spans 6-12m. The length and depth of BR-29 filter is not known. The longer length of these filters allow them to detect contaminants in the groundwater over a greater depth in the aquifer. However, the longer filter depth reduces the accuracy of sampled

	Well ML1	Well ML2
Filter A (m)	5-8	6-9
Filter B (m)	12-13	12-13
Filter C (m)	23-25	23-25

Table 3.3: The depth of the three filters for multilevel wells ML1 and ML2.

physical and chemical parameters with respect to depth. The three filters placed in each of the two wells were therefore shorter in length.

The exact location of each filter was determined based on soil wetness levels in the ground during drilling and decided by Mona Hansen from NGI. The filter depths and locations are detailed in Table 3.3. The uppermost filter in ML1 and ML2 is 3 meters long. The top filter is the longest of the filters to ensure that it captures the top of the groundwater table, provided seasonal fluctuations. The second filter is 1 meter in length for both wells and placed approximately at the half the depth of the well, at 12-13 meters. The third filter was placed as deep as possible, between 23 and 25 meters in both wells. The bottom filter was placed at this deep point based on previous reports that indicate there could be vertical flow in this area and current filters only monitor to approximately 12m. Additional details regarding location of wells, casing and elevation is found in Table A.6.

3.4.2 Hydraulic head

Hydraulic head can be determined from a simplification of Bernoulli's principle, which states that the total hydraulic head (h_t) is the sum of the pressure head (h_p), elevation head (z) and velocity head (h_v). In flow through soils, the velocity head term is ignored because the flow has a low velocity [Evans et al., 2021]. The equation can be simplified to Equation 3.6, where the second term is the pressure head (h_p).

$$h_t = z + h_p \tag{3.6}$$

3.4.3 Manual hydraulic head measurements

Manual measurements were taken with a Water Level Meter. The Water Level Meter includes a measuring tape and a probe at the end. When the prob reaches water it beeps and the length from the water to the top of casing (TOC) can then be noted (Figure 3.7). To find the depth of the groundwater table, the distance between the TOP to the ground surface must be calculated. At OSL the casing is below the ground. The groundwater level (GW) with respect to the surface elevation (S) and measured depth to groundwater (DGW) can be calculated with Equation 3.7.

$$GW = (S - TOC) - DGW \tag{3.7}$$

3.4.4 Automatic hydraulic head measurements

The groundwater was measured both automatically with six water pressures sensors, one for each filter. The water pressure sensors used were Van Essen Micro-Diver Water Level Loggers. Additionally, a Van Essen Baro-Diver Barometric Pressure Logger was used. When the water and air pressure sensors were retrieved they included data regarding the pressure [cmH_2O] and temperature [C°] for each date and time sampled. The water column (WC) above the water pressure sensor can be expressed as:
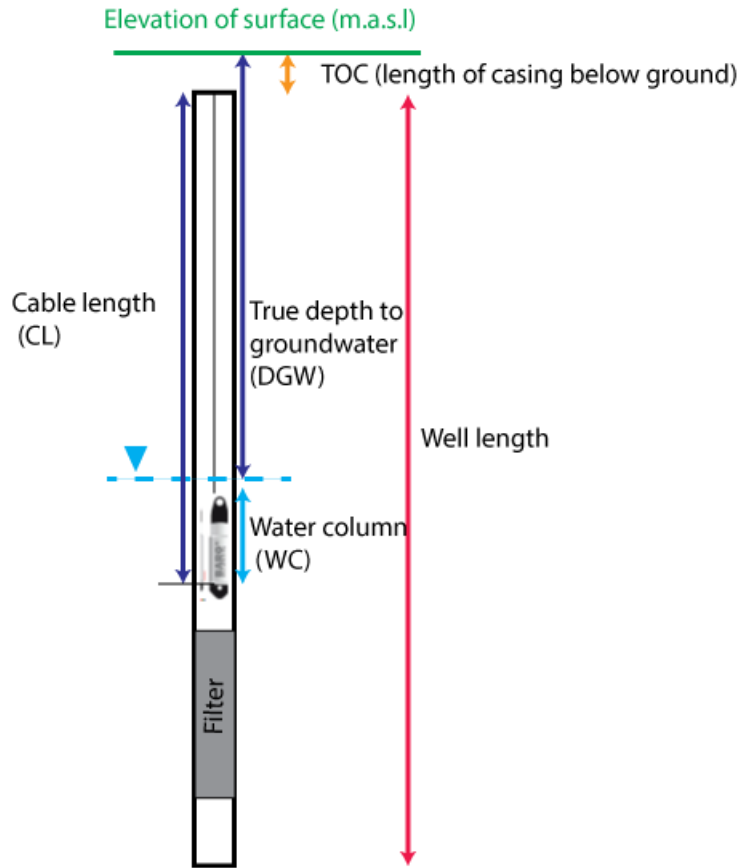
Figure 3.7: Schematic of a groundwater well and information used for hydraulic head measurements. The cable length (CL) is for the water pressure sensor, which is shown below the water column (WC). The top of casing (TOC) is below surface elevation at Oslo Airport.

$$WC = 9806.65 * \frac{p_{Diver} - p_{baro}}{\rho * g} \tag{3.8}$$

where p is the pressure in cmH_2O, g is the acceleration due to gravity (9.80665 m/s^2) and ρ is the density of water (1,000 kg/m^3). The depth to the water level (WL) from the surface elevation can be estimated by equation Equation 3.9:

$$WL = (TOC + CL) - WC \tag{3.9}$$

where CL is the cable length and top of casing (TOC) is below the ground surface.

Water pressure sensors took measurements every 12 hours. The barometer was placed in well ML2 Filter B. The sampling period for the water pressures sensors and barometer is based on when they were inserted and removed from the filters (Table 3.4). ML2 has a longer sampling period since it was inserted approximately a month prior to ML1. This is due to the fact that it was more difficult to sample ML1 since it is very close to the runway. Manual groundwater measurements and the water pressure sensors were used to determine the groundwater depth and if there was any differences in hydraulic head between filters. Dates of manual groundwater measurement are found in Table 3.4.

Possible error in diver data includes accurate measurement of the string the diver is connected to. Given that the height of the topographic surface and each of the filters was measured by OSL using professional surveyors, these measurements are likely accurate. The string of each of the divers was measured both before inserting it into the wells and after pulling the water pressures sensors out of the water on April 5th, 2022. When measuring the length,

Date	Groundwater Measurements	Divers	Water Samples
12.08.2021*			ML1, ML2
22.9.2021	ML2	Inserted in ML2	
13.10.2021	ML1, ML2	Inserted in ML1	
23.11.2021	ML1, ML2		ML1, ML2
05.04.2022	ML1, ML2	Divers removed	

Table 3.4: Measurement dates for wells BR29-ML1 and BR29-ML2. Measurements include manual measurements of groundwater level, water samples for analysis, and diver start and stop dates. * indicates water samples were taken by Avinor.

care was taken that the string was taught and straight. For the second measurement, a long measuring tape was used that could measure the entire length of each water pressures sensor.

3.5 Water chemistry sampling

Groundwater from multilevel wells Ml1 and Ml2 were sampled on August 12, 2021 and on Nov. 23rd, 2021. Groundwater samples were taken from each of the three filters (A,B and C) for ML1 and ML2 for both sampling campaigns. The August water sampling was done by Avinor and lab analysis was done at the Eurfins Labortory in Oslo. The November sampling was conducted by myself and with the help of a technician from OSL. All the water composition analysis for the November sample was done at the sedimentology and geochemistry labs at the University of Oslo.

To sample the groundwater, a plastic tube was inserted into the well and pumped using the an electric pump supplied by OSL. Before sampling the water, 30 L was first pumped to allow for values to stabilize. Field measurements include pH, temperature and electrical conductivity. Ph was calibrated daily with the standard pH 4.0 and pH 7.0. The pH and other field parameters were measured under continued water flow after letting it first flow 30 L. Water samples were taken in 40 mL plastic bottles. For each well filter, one 40 mL bottle was filtered and 1-2 drops of 7M HNO_3 was added for cation analysis. Additionally, a 40 mL bottle was filtered for anion analysis and additional spectrophotometry. It was filtered using a 0.45 μm disposable filter. Samples were filled to the top of the bottle and care was taken to

Figure 3.8: Water sampling for well ML2 using the an electric pump from Avinor. (a) Filtering samples into 40 mL bottles. (b) Pumping water with electric pump using Avinor vehicle.

ensure there was no trapped air bubbles. The bottles were stored in the fridge at 7°C in the dark. The samples were analyzed the same day for alkalinity. Alkalinity was measured by using an autotitrator, where the pH is continuously monitored.

3.6   Water chemistry analysis

3.6.1   Major ion analysis

Water analysis of major anions and cations was performed using ion chromatography. The machine used for this was called a Dionex ICS - 2000Ion Chromatography System. The IC consists of a detector, analytical column, high-pressure regenerate pump, chemical suppressor, injection valve and eluent pump [Fritz, 1987]. An eluent is added to control the pH and modify ionic strength. When the eluent is flowing, the sample to be analyzed (analyte) is injected. The fluid passes through a column with stationary fixed material. The stationary material has ionizable functional groups where targeted ions are separated by sorbing to the fixed material (absorbent). The bound molecules will separate at different speeds from the stationary phase based on their binding strength as the eluent continues to flow through the column [Fritz, 1987]. This strength is based on ion characteristics such as size, shape and charge. The sample passes through a detector which measures peaks in ions. The suppressor is used to reduce background ionic strength. A chromatogram shows the relationship between time and the electrical conductivity. The peaks can then be compared with a known standard and the concentration of the different major ions in the analyte can be determined.

3.6.2   Trace element analysis

Quadrupole Inductively Coupled Plasma Mass Spectrometry (ICP-Q-MS) is a precise and accurate analytical instrumental technique for determining the concentrations of trace elements below 1000 ppm [Balcaen et al., 2015]. The ICP-Q-MS first converts the sample to an aerosol before transferring it to the argon plasma. The argon plasma ionizes the sample and the ions are guided with electrostatic lenses to the quadruple mass analyzer. The quadruple mass analyzer separates the ions according to their mass-to-charge ratio and the ions are sequentially measured with a detector [Wilschefski and Baxter, 2019]. ICP-Q-MS was used in this study to determine the concentrations of iron and manganese from the extraction experiments and from the groundwater samples. Analysis of the samples with ICP-Q-MS was done by Magnus Kristoffersen at the University of Oslo and by Eurofins laboratory in Oslo.

3.7   Meteorological Data

Meteorological data was collected online to estimate when chemical deicer infiltrated for season 2020/2021 and 2021/2022. Precipitation and temperature data was collected from xww.xgeo.no for Gardermoen station 4780 N for January 1st, 1990 - June 2nd, 2022. The station is located at OSL and is north of the western runway. Data for snow cover was collected from xww.xgeo.no from 4740 Ukkestad weather station. The station is approximately 3 km south-east of Oslo Airport. A previous study showed that snow depth data from the Ukkestad weather station has an 80% correlation to snow depth at OSL. Thus, values from Ukkestad weather station have a possible error value of 20% but give an approximation of snow cover trends at the airport.

3.8 Avinor water chemistry and sedimentary data

The grain size characterization of the four boreholes in this study was compared to previous borehole logs conducted near western runway. Logs provided were for BR29-5, BR29-4, BR29-3, BR29-2 and BR29-I2. Results from these borehole logs were compared to the sedimentary mapping of these boreholes in Hansen et al. [2020b]. Sedimentary characterization was included in this report for BR29-5, BR29-4, BR29-3, BR29-2, BR29-I2 and BR29. The log for BR29 was not available and characterization was based on the figures provided in Hansen et al. [2020b].

Water chemistry data was provided from Avinor from monitoring wells. The historical water chemistry data used in this research study is taken from wells BR29-5, BR29-4, BR29-3 and BR29-2 and BR29. These wells were chosen because they are analyzed frequently and they are along the groundwater flow line that is downgradient of the western runway. Water chemistry analysis of these wells focused on iron and manganese concentrations from the year 2020-2021. Water chemistry data was not yet available for 2022 when this research study was finalized. The year 2020-2021 was analyzed because there was a higher frequency of monitoring points. This data allowed for the analysis of monthly trends, which could then be compared to meteorological data. The water samples in ML1 and ML2 could also be compared to these concentrations. The filter depth of wells from Avinor are for a depth of 6-12m. This filter depth therefore spans the a wider depth than filters from ML1 and ML2. Thus, the depth of both Filter A and B in well ML1 and ML2 are within the range of the other known filter depths (BR29 filter depth is not known).

3.9 Geochemical modeling with PHREEQC

Geochemical modeling was conducted with PHREEQC interactive version 3.7.3 in this research study. PHREEQC is a computer program written in C++ programing language. PHREEQC was designed to perform a large number of aqueous geochemical calculations. PHREEQC is a geochemical program that can perform speciation and saturation calculations, batch-reaction, inverse geochemical calculations and 1D advective reaction-transport modeling [Parkhurst and Appelo, 2013]. The program is based on equilibrium chemistry of aqueous solutions which can interact with minerals, gases, solid solutions, exchangers and sorption surfaces. Additionally, PHREEQC can model kinetic reactions with rate equations [Parkhurst and Appelo, 2013].

3.9.1 Aqueous speciation calculations

PHREEQC determines the aqueous speciation, saturation indexes, and partial pressure of the gas phase based on water samples. The model uses the datablock SOLUTION_SPREAD. Aqueous speciation calculations are determined for the 12 water samples collected from each of the three filters in ML1 and ML2 for August and November. There are two main objectives of the aqueous speciation calculations. The first is to determine the saturation index of iron and manganese oxide minerals. The second objective is to determine if there are differences in SI index between filters which could provide insight into geochemical processes occurring with respect to depth in the aquifer.

Water chemistry data used for the aqueous speciation calculations is found in Table A.7. Due to different labs and testing capabilities there was some differences in chemical parameters collected in each of the samples. The pH was not determined for the August sample and so the pH from the November sample was used for the respective filters for the August samples. Additionally, a redox meter was not available for both the August and November sample analysis. The pE value was set in PHREEQC based on the redox couple NH_4^+/NO_3^-, when available. Nitrate and ammonium were analyzed in the August sample but only nitrate

was analyzed in the November sample. The concentrations of ammonium determined in the August sample were used in the calculations for the November water sample to allow for possible redox evaluation. Filter B and C in both wells had generally much lower or no nitrate measured. Thus, pE was set for Filter A using redox couple NH_4^+/NO_3^- and set to the default value of 4 for Filters B and C. Additionally, to calculate the saturation indexes of feldspars, muscovite and montmorillonite in PHREEQC, the concentrations of aluminum determined for the August campaign were included in November samples (based on well and filter).

The speciation model uses the database *llnl.dat*. Mineral phases ankerite and pyrochroite, which are not found in *llnl.dat*, were included in the model. The ankerite solubility equation was taken from webmineral.com and the equilibrium constant for dolomite was used based on data from Palandri and Kharaka [2004]. A neutral mechanism was used given groundwater pH values measured in well ML1 and ML2. Phase data for pyrochroite was taken from database *Phreeqc.dat*.

3.9.2 Reaction model with addition of chemical deicers

The reaction model includes the addition of deicers and uses imposed thermodynamic boundary conditions based on the results from the speciation model. The objective of the model is to simulate the effect of a pulse of chemical deicers during snow melt. This pulse injection is simulated using water chemistry data from November for well ML1 Filter A and B. This well was chosen because it lies the closest to the runway. As boundary conditions, the model uses the SI of minerals which were determined in the speciation model for each respective water sample. The minerals were included using the keyword data block EQUILIBRIUM_PHASES. The minerals chosen to use in the model include calcite, quartz, ferrihydrite ($Fe(OH)_3$) and manganese oxide in a reduced form ($Mn(OH)_2(am)$). A reduced form of manganese is used to force the model to primarily dissolve iron oxides rather than manganese oxides. In addition, $CO_2(g)$ was included in the datablock.

The injection pulse of deicers is based on historical data from well BR29. Well BR29 was chosen because it contains some of the highest concentrations of deicers and it is also closest to ML1. Water chemistry data from both Filter A and B were included given that this is the filter depth of other wells nearby (BR29 filter depth is not recorded). Deicer concentrations from the two dates 12.02.2020 (C1) and 04.04.2019 (C2) were chosen. Water sampling data from November in Filter A and B was chosen because it is more likely to be closer to the water chemistry in late winter or early spring compared to the August concentrations. The The saturation indexes used for the two models is shown in Table 3.5.

For the degradation of propylene glycol it was assumed that an anaerobic pathway should be used. The reasoning for this is that during a period of high deicer input the groundwater will more likely become anaerobic. Additionally, these two sampling periods contained a high level of acetate, which is an intermediary product in the anaerobic decomposition of propylene glycol (Equation 2.12).

	SI (Filter A)	SI (Filter B)
$Fe(OH)_3$	1.09	1.55
$Mn(OH)_2(am)$	-7.83	-6.51
Calcite	-1.97	0.251
Quartz	0.62	0.894
$CO_2(g)$	-1.42	-1.68

Table 3.5: Saturation indexes used for the two reaction models based on aqueous speciation calculations for well ML1 Filter A and B from the November sampling campaign.

	Formate (mg/L)	Acetate (mg/L)	PG (mg/L)	Formate (mol)	Acetate (mol)	PG (mol)
C1	38.9	79.3	0.1	8.45E-04	1.34E-03	1.31E-06
C2	40.1	130	240	2.82E-03	6.79E-04	3.15E-03

Table 3.6: Pulse concentrations used in the PHREEQC reaction model with the addition of chemical deicers. The pulse concentrations are based on historic data provided by Avinor for well BR29. Concentrations detected are from the dates 12.02.2020 (C1) and 04.04.2019 (C2). The concentrations are given in both mg/L and mol.

Equation 2.13 was used for acetate degradation and the half-reaction of formate was used for formate degradation. Because PHREEQC was unable to recognize propylene glycol, the degradation product propionate was used instead. One mole of propylene glycol degrades to half a mole of propionate and half a mole n-propanol, which further degrades to half a mole of priopionate (Equation 2.12 and Equation 2.11). Therefore, there is a one-to-one molar ratio between propylene glycol and propionate when propylene glycol is degraded. For PHREEQC to be able to recognize the degradation products of propionate, Equation 2.13 and Equation 2.12 were combined to eliminate acetate. Equation 3.10 is the final equation that was used for the degradation of propylene glycol in terms of propionate degradation.

$$\underset{\text{propionate}}{CH_3CH_2COO^-} + 4\,H_2O \longrightarrow \underset{\text{methane}}{CH_4} + H^+ + \underset{\text{bicarbonate}}{2\,HCO_3^-} + 3\,H_2 \tag{3.10}$$
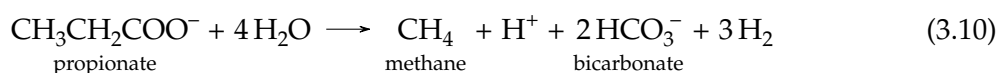
The deicers are added in 1 step using the REACTION data block. The model output includes the change in moles of minerals listed in the EQUILIBRIUM_PHASES.

Chapter 4

Results

4.1 Physical and chemical characterization of sediment samples

4.1.1 Grain size results from the field

The grain size is predominantly fine to medium sand and ranged in size from clay to gravel. In the unsaturated zone, all four boreholes were predominantly fine to medium sand with some silt layers. In boreholes ML2 and JordC there is a medium sand layer in the top 2 meters, while for JordB and ML1 it is predominantly fine sand. All four boreholes include silt layers between 2 and 4 meters. All of the boreholes except ML2 have a narrow clay layer. JordC has a clay layer between 3.3-3.8 meters and ML1 and JORDB have clay layers at 2 meters and 3 meters, respectively. In ML1 and ML2 there is fine to medium sand below the silt and clay layer until the groundwater table. For JordC, the coarse sand starts after the silty clay layer at 4 meters. For JordB, there is coarse sand and gravel below the silty layer at 3.4 meters.

There is a shift towards coarser-grained material along groundwater table for the four boreholes. A medium to coarse sand layer coincides with the the groundwater table in the boreholes. There is a medium sand layer of approximately 2 meters that is present in all boreholes between 4 and 7 meters deep. There is predominantly medium to coarse sand in ML2 between 5.5 meters and to 15 meters and in ML2 from 5.2 to 17 meters. ML2 also contains a layer of fine sand in this interval from 7-8.5 meters. JordC has a general increase in grain size from 3.8 meters until the end of sampling at 8 meters. For JordB, the medium-coarse layers are from 5-7.4 meters. There is a shift towards finer sediments in the deeper layers. For ML2, it is fine sand from 15-26 meters. From 17 meters, ML1 has 2 meters with silt and then is predominantly fine sand with some medium sand layers until 26 meters. For JordB, the soil is predominantly fine grain sand from 7-14.4 meters with some alternating medium sand layers.
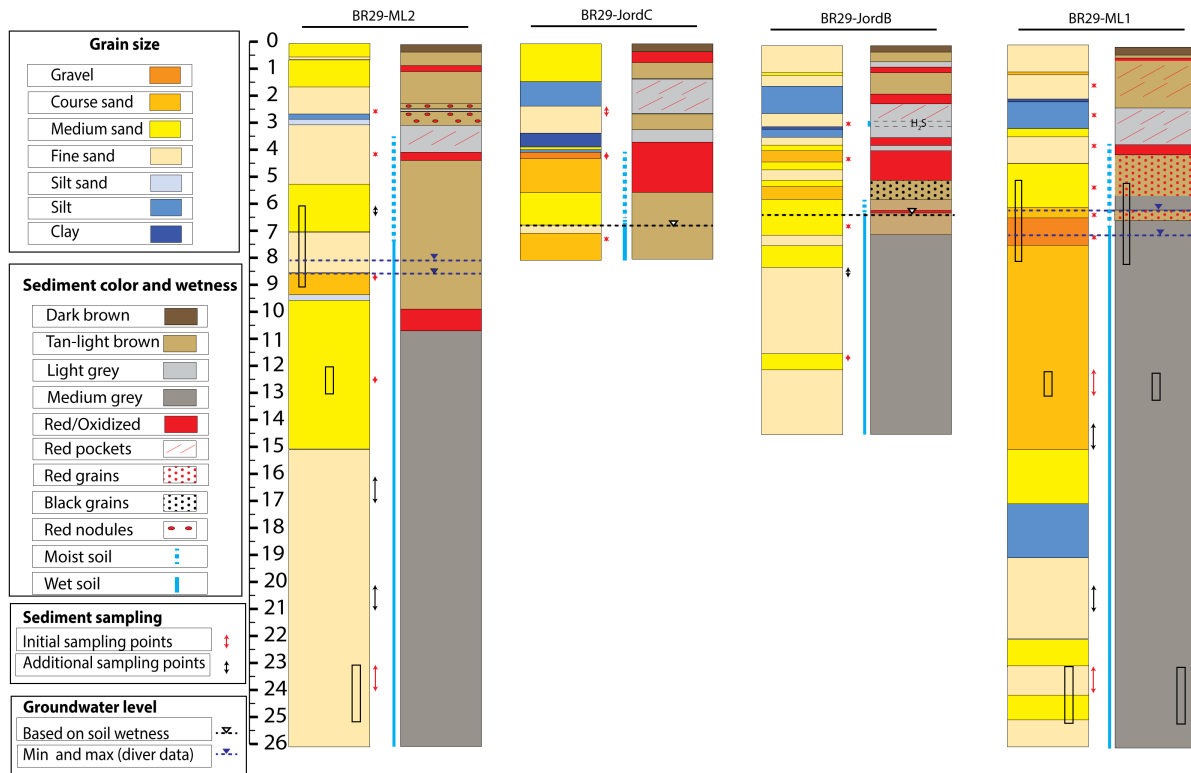
Figure 4.1: Grain size characterization of sediments from boreholes ML1, ML2, JordB and JordC near the western runway of OSL. The location of the boreholes with respect to the western runway is shown in Figure 3.1. Grain size was determined primarily in the field; laboratory sampling points are indicated with black and red arrows. Location of filters for multilevel wells ML1 and ML2 are shown as black rectangles. A profile is also included of sediment coloration, including red coloration (possible iron oxidation) and black nodules or grains (possible manganese oxidation). Moist and wet soil is based on field analysis. The groundwater level for wells ML1 and ML2 is based on water pressure sensor data and it was estimated based on soil wetness levels in the field for boreholes JordC and JordB.

4.1.2 Grain size results from the laboratory

The twenty samples used for lab analysis are marked in red in Figure 4.1. Subsequent samples were taken for additional grain size analysis (marked in black in Figure 4.1). The results of the grain size analysis are shown in cumulative grain size distribution curves in Figure 4.2. These curves show the general heterogeneity in the samples. Both the uniformity coefficient and coefficient of curvature were determined to be well-graded for the majority of the samples between a depth of 0 - 12 meters below the surface (Table A.3). Poorly graded sediment was found in borehole ML1 in the two samples between 12-24 meters. For ML2, sample point 16-17 and 23-24 is poorly graded, though sample point at 20-21 is well graded. The poorly graded sand has a large fraction (>50%) of fine-grained sand (Table A.10). The sample point from ML1 at 7-7.2m was found to be predominantly coarse-grained. However, this point was determined to be gravel in the field. Given that larger rocks can fall from the auger before being drawn up with other grains, it is likely that this sample point underestimated the grain size. Thus, in Figure 4.1 this sample is labeled as gravel.

The samples are predominantly loamy sand to sandy loam (Figure 4.3). The only outlier is ML1 at 2.5-2.7 meters, which is a silt loam. For ML1, ML2 and JordB there is a trend towards increasing percent sand with depth. This is due in part the to the greater number of sampling

points near the groundwater table, where there are coarser sediments. For ML1, the top four sample points contained more silt than the bottom four points, with 2.5-2.7m containing the highest level at 62%. For ML2, the silt is the highest in the top two depths, at 27% and 16% respectively. For both ML1 and ML2, the bottom most sampling point, 24-25m had a higher silt level (14 and 5%) compared to 12-13m (8 and 2%). JordB shows a modest decrease in silt with depth from 13-7%. Jord C, where sample points did not go as deep, had a silt level of around 20% in the bottom two sampling points and a lower silt content of 10% in the top sampling point. The percentage of clay in the samples varied between 0.53-5.92%. The samples with the most silt generally were the samples with the most clay. There is a general trend of decreasing clay with depth in ML1 and ML2 between 0 and 12 meters. There is a slight increase in clay in ML1 and ML2 from 12-13m and 23-24m.
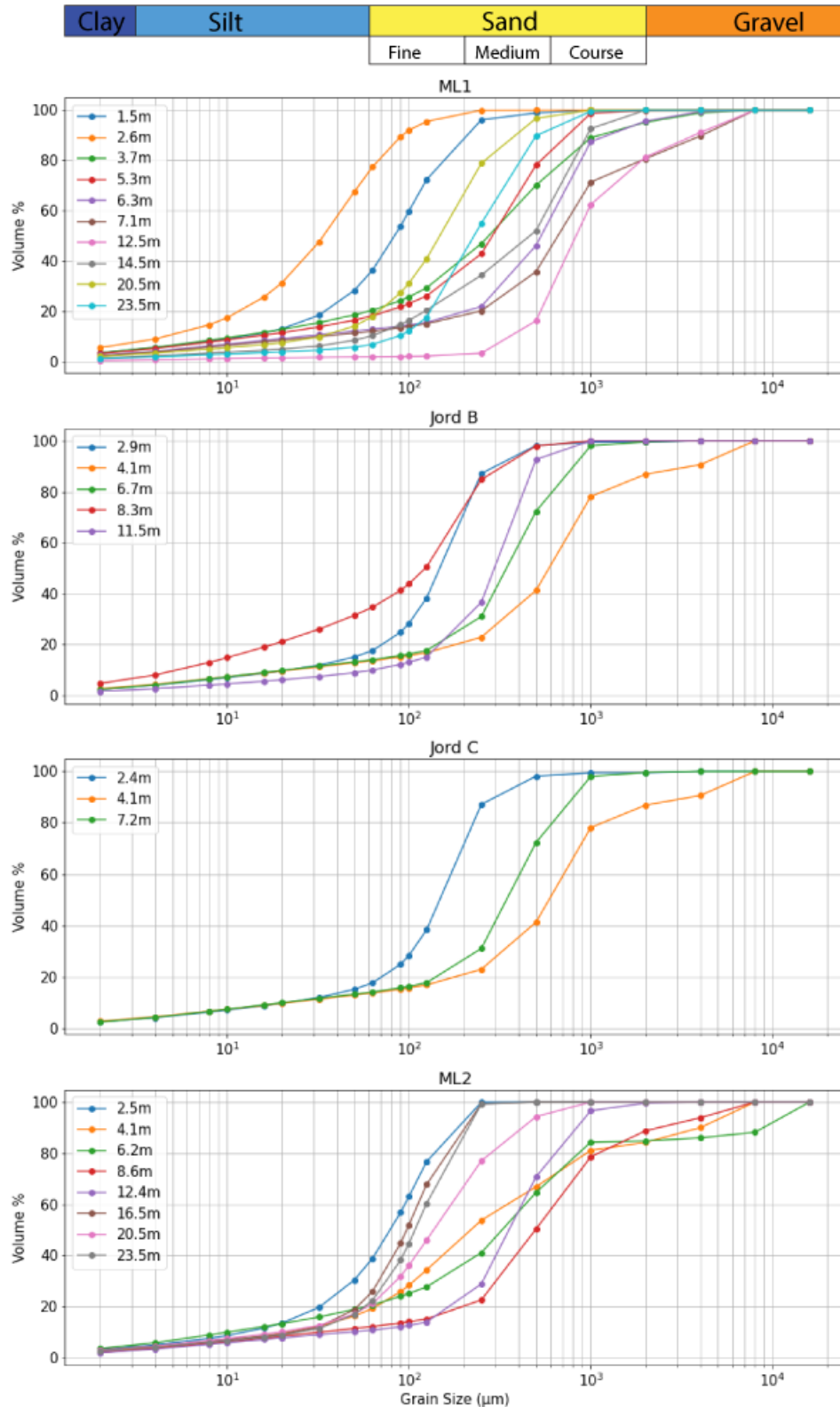
Figure 4.2: Cumulative grain size distribution for boreholes ML1, ML2, JordB and JordC. Sampling depth range and average values location in Table A.2. Location of the sampling points are found in Figure 4.1.
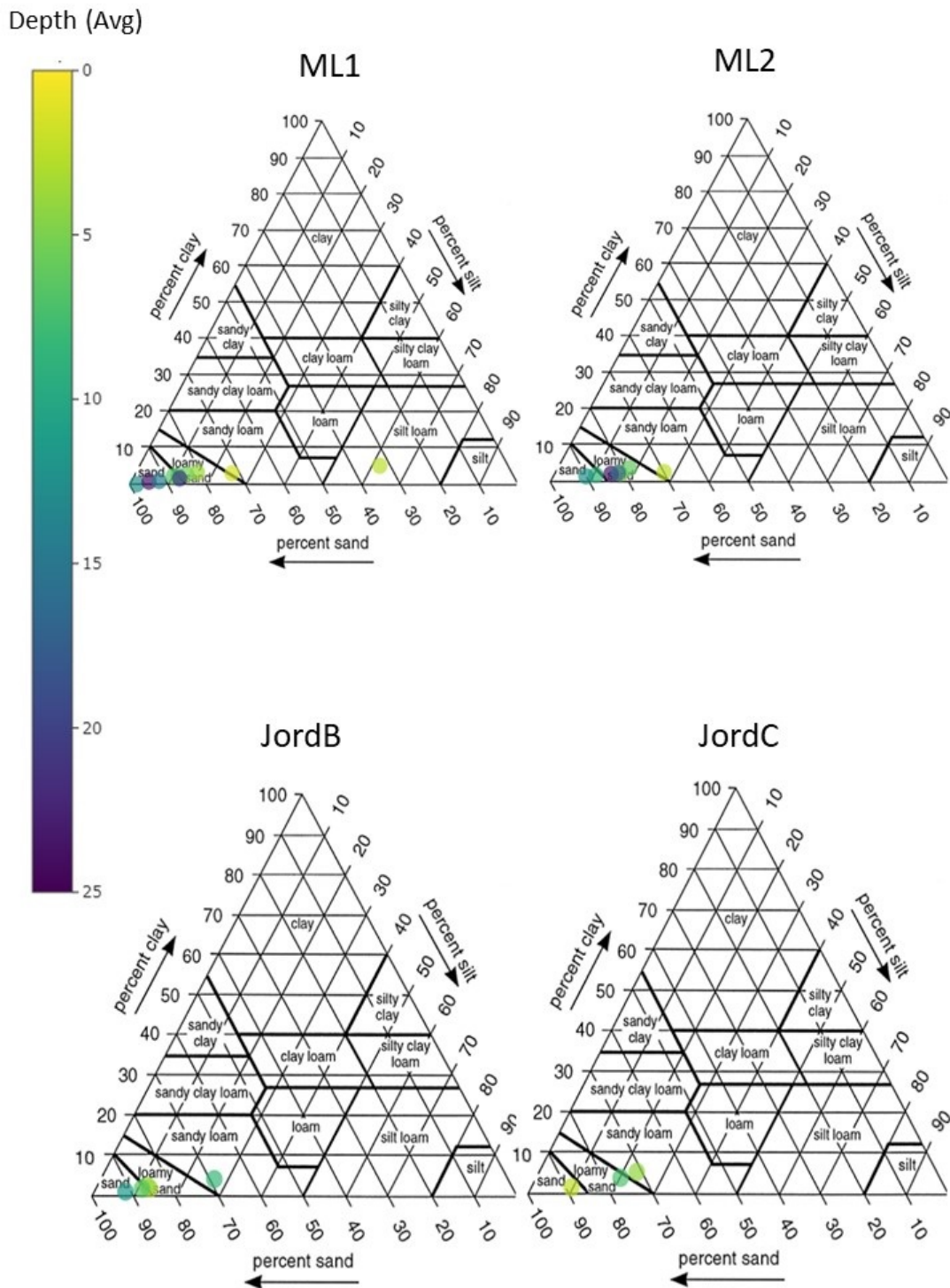
Figure 4.3: Ternary plot of grain size for boreholes ML1, ML2, JordB and JordC. Sediment samples are colored based on the colorbar, which shows the average sampling depth with respect to color. Sampling depth range and average values location in Table A.2. Location of the sampling points are found in Figure 4.1

Hydraulic conductivity estimation based on grain size

The saturated hydraulic conductivity (K_s) was measured for each of the sediment samples analyzed in the lab using the Hazen equation (Equation 3.3). A table with all the hydraulic

	Average	Coarse	Medium	Fine
K_{min} (m/s)	9.85E-06	2.46E-05	1.39E-06	2.54E-06
K_{max} (m/s)	1.48E-05	3.69E-05	2.09E-06	3.81E-06

Table 4.1: Saturated hydraulic conductivity (K) value based on the Hazen equation for sediment samples in the saturated zone from boreholes ML1, ML2, JordB and JordC. Min and max values are based on the empirical coefficient (C) of the Hazen equation. Fine-grained sediment is based on sediment samples in ML1 and ML2 which are from a depth of 16m below the surface.

conductivity values is found in Table A.11. Table Table 4.1 is a summary of the results and includes an average of all sediment samples calculated from the saturated zone. The average min and max (K_s) values are based on a value of 1 or 1.5 for the empirical coefficent (C) of the Hazen equation. The summary table also includes the average minimum and maximum K_s for coarse, medium and fine-grained sediment. The fine-grained sediment used in this summary is only for the fine-grained sediment below a depth of 16m for ML1 and ML2, where the sediment is generally poorly sorted. The average hydraulic conductivity varies between $1.5 * 10^{-5}$ and $9.9 * 10^{-6}$ (m/s). The fine and medium grained sediments have a similar order of magnitude. The average coarse-grained sediment has a higher (K_s) value between $2.5 * 10^{-5}$ (m/s) and $3.7 * 10^{-5}$ (m/s).

4.1.3 Redox zonation from field observations.

The color of the soil provides qualitative clues to areas of reduction and oxidation. Figure 4.1 shows that there are layers of likely iron oxidation in the unsaturated zone for all the boreholes. Figure 4.1 shows areas of tan to light brown sand in the unsaturated zone. This sand is likely silica rich and does not necessarily give clues to redox conditions. In the unsaturated zone there are alternating layers of tan brown and reddish layers and light gray. Often, the light gray soil in the unsaturated zone contains red pockets, indicating areas of iron oxidation.

There are areas along the profile where changes in grain size also include changes in coloration. This can be seen in Figure 4.4b, which shows a shift from silty to find sand in JordC. In this section, the change from silty to fine sand corresponds with a dark red zone of strongly oxidized material, followed by lighter red sand. The silt and clay layers are often light gray, sometimes including red pockets. Oxidized areas in the unsaturated zone are mostly in layers with fine to medium sand, where oxygen can more easily diffuse. Above the clay layer at 3 meters in JordB there was pooling of water and a hydrogen sulphide smell, indicating local reducing conditions. The clay layer in this borehole is likely acting as a local barrier to further percolation. Below this clay layer the grain size alternates between fine to medium grain size with signs of oxidation.

There is generally signs of oxidation towards the top of the water table. Below the water table, the sediment turns a medium gray, such as in Figure 4.4d. This medium gray color is likely a sign of lower oxygen levels or reducing conditions. The change to this medium gray color is seen in all boreholes except JordC, which was bored to only 8m. The medium gray color begins the deepest in ML2. In ML2there is a layer of light gray with red pockets that appears in the upper unsaturated zone, which mostly corresponds to finer-grained and silt sediments.

(a)	(b)	(c)	(d)
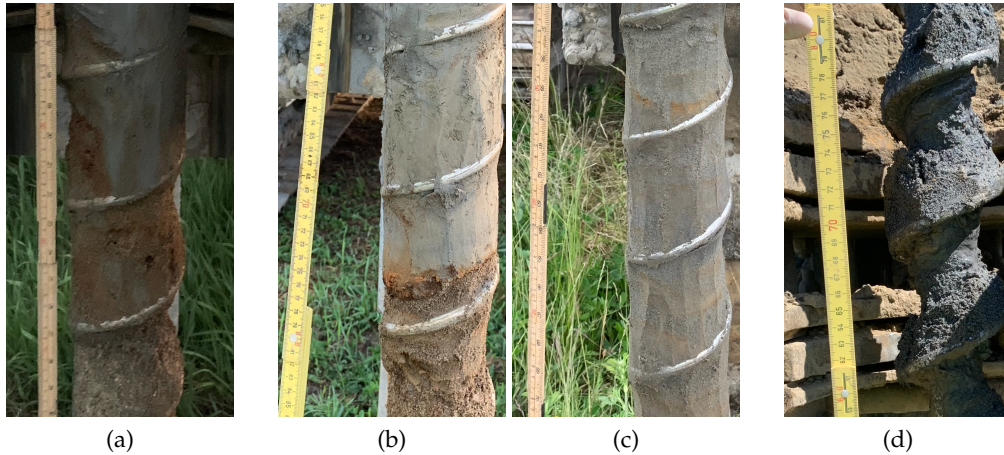
Figure 4.4: Sediment cores extracted with an auger drill. Photos taken by Mona Hansen from NGI. a) Grey sediment above area of oxidized sediment in JordB at 3-4m depth. b) Light grey sediment above a band of strongly oxidized sediment in JordC at 3-4m depth. c) Light grey sediment with lightly oxidized bands in ML2 between 3-4m depth. d) Dark grey sediment below the water table in ML2 between 10.7-11.0m depth.

4.1.4 Microscopy analysis

Figure 4.5 and Figure 4.6 show Scanning Electron Microscope (SEM) backscatter images from six sample locations from borehole ML1 and and four sample locations from ML2. The minerals detected include potassium feldspar, quartz, amphiboles, zircon, albite, illmenite and iron oxide. Crystalline secondary precipitate was seen in the unsaturated zone and along the water table of ML1. At a sampling depth of 1.5m in ML1, crystalline iron oxide was observed but no secondary iron precipitate was seen (Figure 4.5A and Figure 4.5B). At a depth of 3.7m in ML1 there were several grains that contained a thin iron coating of secondary precipitate (Figure 4.5C). This sample depth corresponds to sediment that was found to be oxidized and red in color. Figure 4.5E is an enlarged version of Figure 4.5D and shows the thin coating on top of a quartz grain. The secondary precipitate is crystalline. At a depth of 5.3m in ML1, the sediment sample contained a significant amount of secondary iron precipitate . The white coating in Figure 4.5F on many of the grains is secondary iron precipitate. Figure 4.5H shows the growth of this secondary crystalline precipitate. At a depth of 6.3m there was inclusions of crystalline iron oxide found (Figure 4.5I) and small localized areas of secondary crystalline precipitate (Figure 4.5J). At a depth of 7.1m the grains were coated with iron-rich clay and some iron oxide crystals were seen in the clay (Figure 4.5L). At a depth of 12.5 meters there was no evidence of secondary precipitate but there was significant amount of iron inclusions, seen in white in Figure 4.5M. Figure 4.5N shows an enlargement of the iron oxide crystalline growth.

In Well ML2 at a depth of 2.5m there was some minor areas of crystalline inclusions and a few localized areas where secondary iron oxide coating was found (Figure 4.6A). At a sampling depth of 4.1m amorphous iron oxide coating was found (Figure 4.6C and D). In Figure 4.6D there is amorphous coating on the top-left part of the figure and crystalline iron oxide on the bottom-right. This figure shows the possible transformation of amorphous iron oxide to crystalline iron oxide. As shown in the sediment color profile, at this sampling depth the sediment was oxidized and red in color. At a sampling depth of 8.6m there was some localized areas of iron oxide crystalline precipitate seen. This precipitate included more elongated crystalline shapes than seen in other samples (Figure 4.6F). At a sampling point at 12.5 meters, iron oxide was not found. At this sampling depth there was an iron-rich clay coating on the grains. Pyrite crystals were also found in this sample (Figure 4.6H).
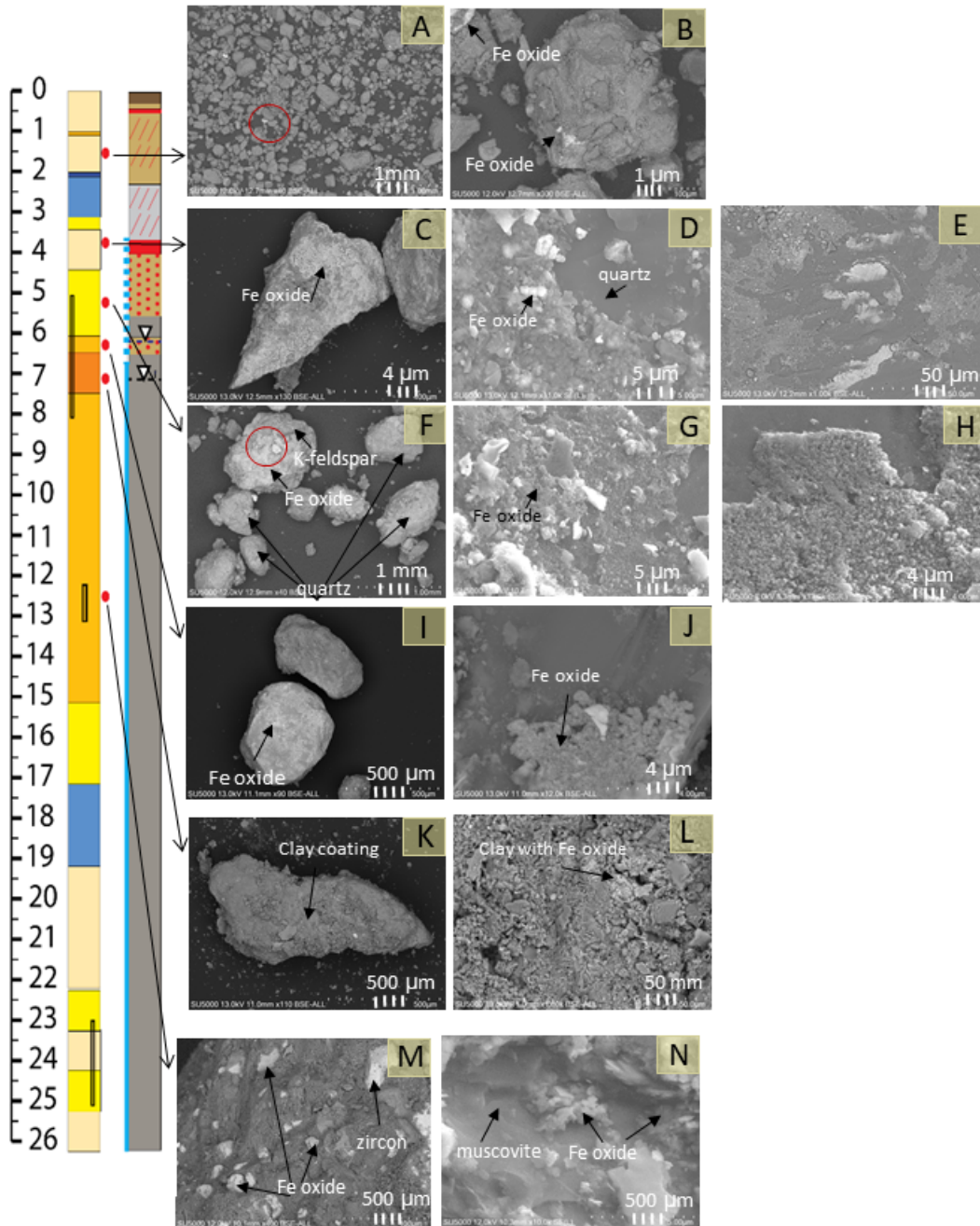
Figure 4.5: SEM backscatter images from borehole ML1 with borehole sediment characterization and redox color profile shown to the left from Figure 4.1. The arrows and red dots indicating the depth of the sampling points. Image A (1.5m) shows a white iron oxide inclusion with a red circle. Image B is an enlargement of the area indicates from in Image A and shows two iron oxide inclusions. Image C (3.7m) shows iron oxide coating. Image D and E show enlargement of Image C and show iron oxide secondary precipitate. Image F (5.3m) shows extensive iron oxide precipitate on the grains. Image G and H are enlargements of the area indicated in Image F and show crystalline iron secondary precipitate. Image I (6.3m) shows a point of secondary precipitate on a grain and Image J is an enlarged photo of this area and shows localized secondary precipitate. Image K (7.1) and L show iron-rich clay coating on grains with some iron oxide within the clay. Image M (12.5m) and N show crystalline iron oxide inclusions.
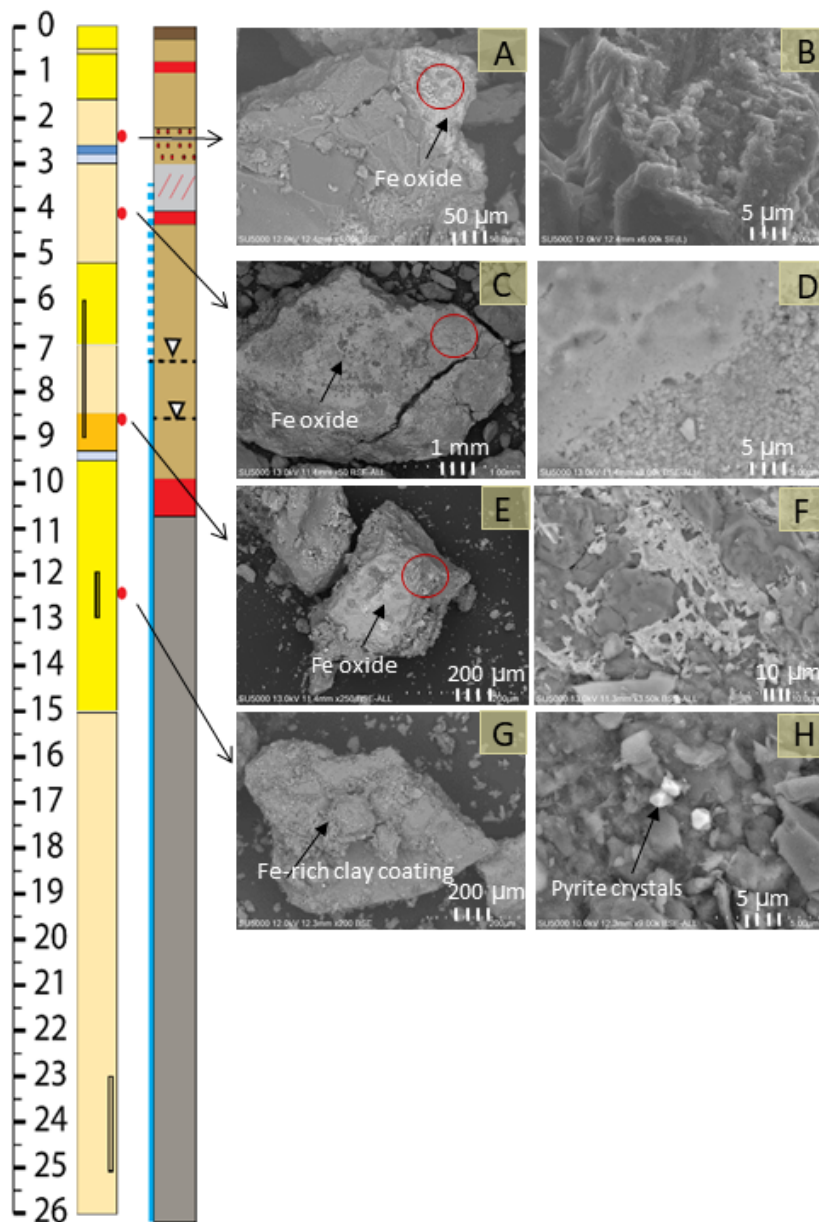
Figure 4.6: SEM backscatter images from borehole ML2 with borehole sediment characterization and redox color profile shown to the left from Figure 4.1. The arrows indicating the depth of the sampling points. Image A (2.5m) shows an area of secondary crystalline growth and B is an enlargement of the circled area in Image A. Image C (4.1) shows a grain coated in secondary precipitate and Image D is an enlargement of Image C and shows amorphous and crystalline secondary iron oxide precipitate. Image E (8.6m) shows localized areas of secondary crystalline precipitate and F shows an enlargement of the area circled in red in Image E. Image G (12.5m) shows iron rich coating of sediment and Image H shows pyrite crystals.

4.1.5   X-ray diffraction

Twenty samples were analyzed with X-ray diffraction (XRD) to determine primary minerals present. Results show that there is considerable homogeneity in mineral composition between samples. Minerals detected by XRD include microcline, plagioclase, hornblende, muscovite, chlorite, calcite and ankerite (Table A.13). Manganese and iron oxide were not found and thus they are likely below the 2% by weight threshold of XRD analysis. The dominant mineral in all the samples is quartz, with variation between 57-69%. Microcline ranges between 3-8%, plagioclase between 13-20%, hornblende between 1-6%, muscovite/illite between 6-11%, chlorite between 3-7%, calcite between 0-2% and ankerite between 0 and 1%. Figure 4.7 shows the samples normalized without quartz to compare relative differences in the more reactive minerals. Calcite generally increases with depth in each of the wells. The calcite concentration in 12-13m is higher than 23-24m for both ML1 and ML2. Ankerite does not show as clear of a relationship with depth except in ML1. Muscovite is slightly lower in the top layers of ML1 compared to the rest of the samples.
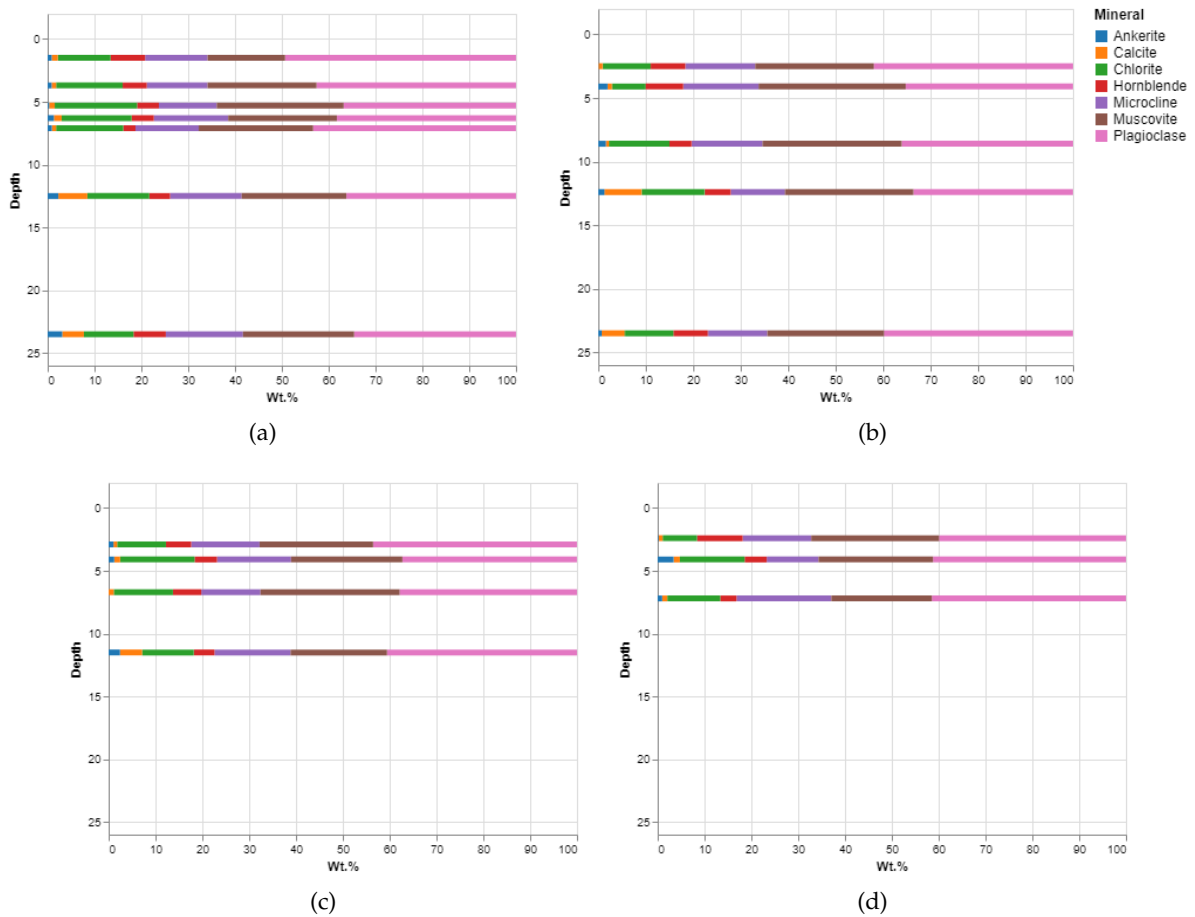
Figure 4.7: Wt. % of minerals normalized without quartz. Where a) is borehole ML1, b) is borehole ML2, c) is borehole JordB and d) is borehole JordC.

Based on the relative amounts of minerals in each sediment, the amount of iron in the primary minerals can be roughly estimated. Since such an estimation is based on stoichiometry of the primary mineral it does not include mineral impurities. Crystalline manganese could not be estimated given that none of the primary minerals contain manganese. The main minerals that include iron are chlorite, hornblende, ankerite and muscovite. Based on values calculated by Profex, the amount of crystalline iron from the primary minerals is shown in Figure 4.8. Figure 4.8 shows that chlorite and hornblende are the predominant minerals that contain iron,
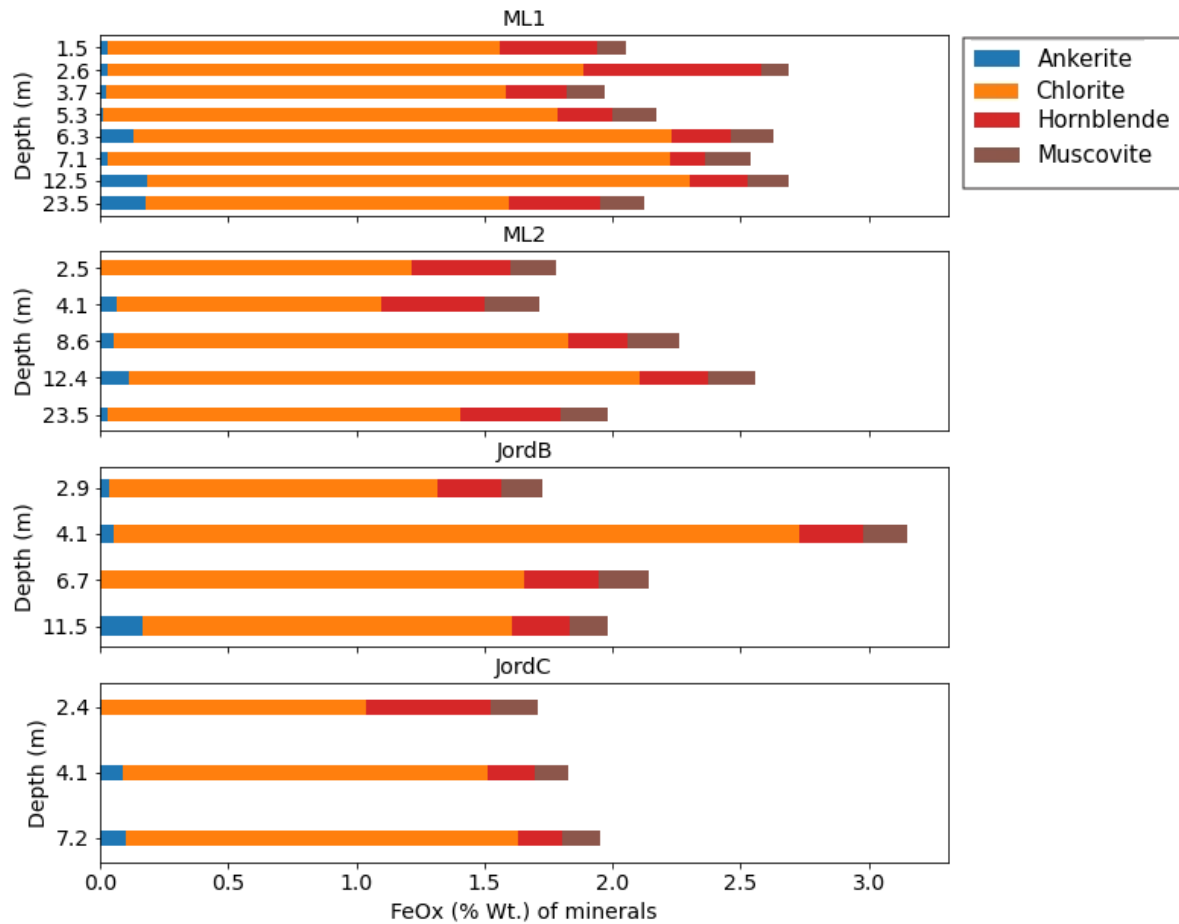
Figure 4.8: Percent by weight of FeOx for minerals identified by XRD for each sample point

with smaller amounts from ankerite and muscovite. The wt.% of iron varies between 1.8-3.1% and there is not a clear pattern with depth. The greatest percent iron is in JordB between 4-4.25m, due to the higher amount of chlorite in this layer.

4.1.6 XRF

The field XRF had a variation between replicates that was small for iron (<3%) but higher for manganese (between 10-50%). The higher error for manganese is likely due to the fact that the manganese concentrations were very close to the detection limit of 49ppm. There is significant error in the amount of iron and manganese determined by the field XRF compared with the control sample used for the field XRF. This error was 24.1% ppm for iron and 11.9% for manganese.

The four samples sent to NTNU for XRF analysis showed a considerably higher wt.% for iron and manganese than the values determined by the field XRF. There was a correlation found with the values determined by the NTNU XRF and the difference between the NTNU XRF and the field XRF (calculated in wt%) (Figure 4.9). The R^2 value for this relationship for iron (wt.%) was 0.91 and for manganese (wt.%) was 0.95. This relationship was used for calculating the concentrations in wt.% of iron and manganese of the samples that were not analyzed by the NTNU XRF. A plot of these values is shown in Figure 4.9 and tabular values are located in Table 4.2.

$$Fe_{corrected} = 1.71(XRF_{Field}) - 0.11 \qquad (4.1)$$

Well	Depth	Fe (NTNU XRF)	Mn (NTNU XRF)	Mn (Field XRF)	Fe (Field XRF)
ML1	6.28	2.92	0.028	23.00	1.17
ML1	7.08	2.43	0.030	23.00	0.97
ML1	12.5	2.35	0.056	99.70	0.92
ML2	8.63	2.50	0.048	34.49	0.91

Table 4.2: Comparison of iron and manganese concentrations in sediment in wt. % based on a field XRF and from laboratory XRF determined by the Berglaboratoriet at NTNU.

$$\text{Mn}_{corrected} = 1.25(XRF_{Field}) - 0.0042 \tag{4.2}$$

Total iron concentrations determined by NTNU XRF analysis or using Equation 4.1 varies between 1.98-2.92 wt. % across all sediment samples. The highest NTNU XRF corrected iron concentration (2.92 wt. %) is located in ML1 at an average depth of 6.3m. This depth is also near the maximum groundwater depth recorded by water pressure sensors in the study. In ML2, the highest concentration of iron is at an average depth of 2.5m with a corrected concentration of 2.82 wt. %.

Total manganese concentrations determined by the NTNU XRF analysis or using Equation 4.1 varies between $1.58 * 10^{-2}$ - $6.49 * 10^{-2}$ for all samples. The highest concentration in ML1 for the NTNU XRF corrected manganese concentrations is at an average sampling depth of 1.5m ($5.3 * 10^{-2}$ wt. %). At an average ML1 sampling depth of 6.3m and 7.1m, the NTNU XRF corrected manganese concentration drops to $2.8 * 10^{-2}$ and $3 * 10^{-2}$ wt. %, respectively. There is a similar drop in ML2 in the unsaturated zone for manganese, at an average sampling depth of 4.1m and 8.6m.

(a)

(b)
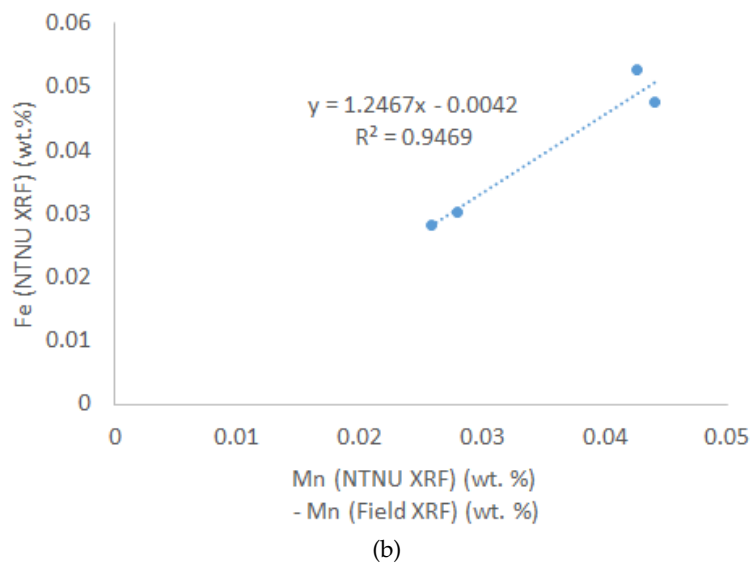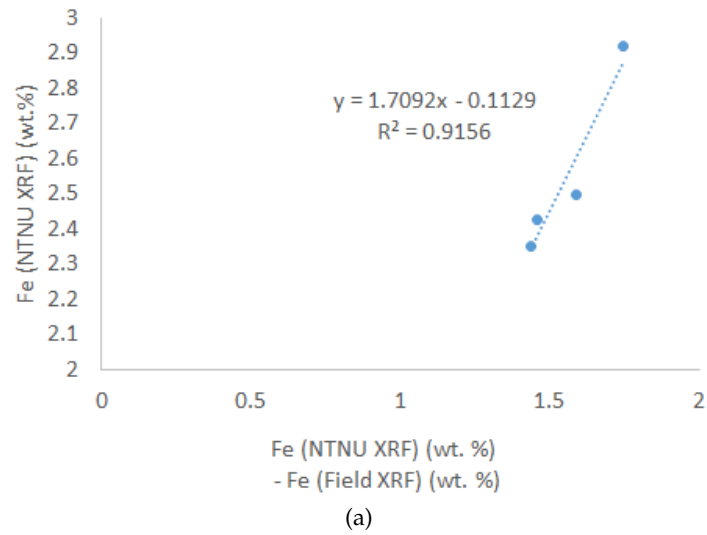
Figure 4.9: XRF measurements from NTNU plotted against the difference between NTNU XRF value and the field XRF value. Figure a) shows the concentration of iron in wt. % along the y-axis from XRF measurements from NTNU (with wt. % shown between 2-3%). On the x-axis is difference between NTNU XRF measurements (wt. %) and an XRF Field instrument from NGI (wt. %). A line of best fit was drawn for the four points. Figure b) shows the concentration of manganese in wt. % along the y-axis from XRF measurements from NTNU. A line of best fit was drawn for the four points. Data shown in Table A.5
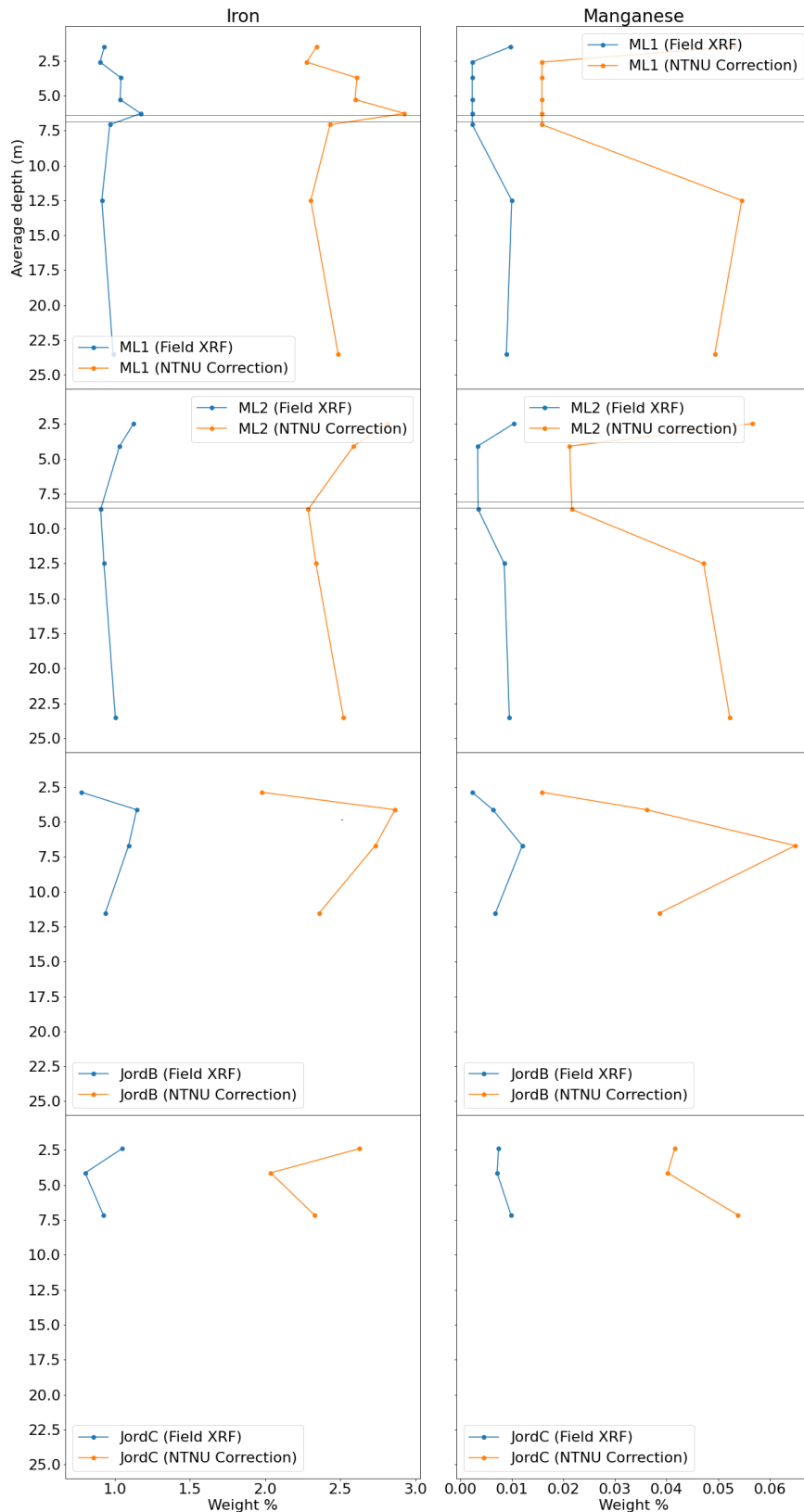
Figure 4.10: Concentration of total iron and manganese in sediment based on measurements by a field XRF, plotted in blue for boreholes ML1, ML2, JordB and JordC. Based on XRF analysis by NTNU (Berglaboratoriet) the field XRF values were corrected using Equation 4.1 for iron and Equation 4.2 and plotted in orange. The black line indicates the minimum and maximum recorded groundwater depth by water pressure sensors.

4.1.7 Organic and inorganic carbon

Total organic and inorganic carbon are very low in all samples. TOC ranged between 0.11-0.17% and TIC ranged between 0.0-0.05%. Values for both TOC and TIC were close to the detection limit. In ML1, there is a slight increase in TOC levels which also corresponds to observed increase in total iron observed with XRF at these points. The trend in TOC also corresponds with relative levels of total iron content (wt.%) determined by XRF values for JordB and JordC.
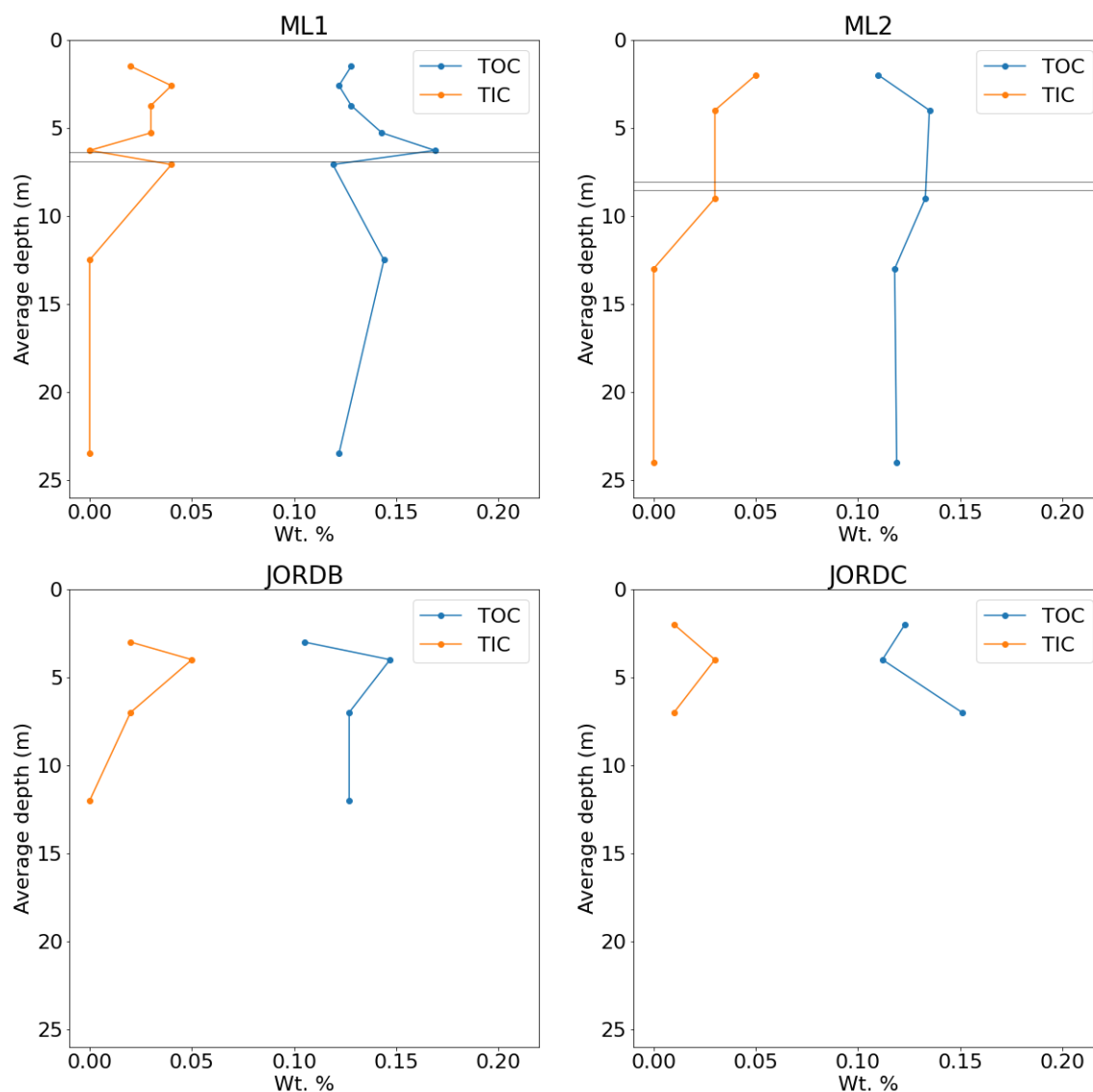
Figure 4.11: Total organic and inorganic carbon determined using an Organic Elemental Analyzer (CHNS/O) for boreholes ML1, ML2, JordC and JordB.

4.1.8 Extraction experiments

The extraction experiments are shown in Table 4.3 and Table 4.4. To determine the validity of the experiment the ratio of iron or manganese from oxalate to DCB was determined. This ratio should be 1 or less given that the DCB experiment accounts for both amorphous and crystalline oxide, whereas oxalate only accounts for the amorphous oxides. The concentrations determined between the oxalate and DCB experiments were similar to one another, shown by the high DCB/oxalate ratios. For samples where the ratio was over 1 indicates that either

	Depth	DCB		Oxalate		Ratio
		Fe(mg/L)	Fe(mg/g soil)	Fe(mg/L)	Fe(mg/g soil)	DCB/Ox
ML1	3.6-3.85	330.01	16.5	116.67	11.67	0.71
	5.15-5.4	246.67	12.33	97.01	9.70	0.79
	6.15-6.4	538.96	26.95	276.80	27.68	1.03
	6.15-6.4*	160.02	8.04	87.03	8.70	1.09
	6.95-7.2	323.33	16.17	140.05	14.03	0.87
	12-13	280.01	14.06	286.67	28.67	2.05
	23-24	20.04	1.01	19.67	1.97	1.97
ML2	4-4.2	96.67	4.83	46.33	4.63	0.96
	6-6.4	266.67	13.33	98.67	9.87	0.74
	8.5-8.75	290.02	14.50	99.01	9.90	0.68
	12.25-12.5	113.33	5.67	67.33	6.73	1.19
	23-24	17.33	0.87	20.67	2.07	2.38

Table 4.3: Average iron concentrations from oxalate and DCB experiments based on three replicas. Concentrations in mg/L were determined based on ICP-Analysis by Eurofins and mg/g dry soil was determined using equation Equation 3.5. Each sample depth is the average value based on three replicas. Sample marked by * was ground.

the DCB experiment did not extract all the iron in the sample or that the oxalate experiment extracted some of the crystalline iron.

The replicas showed generally low variability (<5%). The uncertainty from Eurofins of ICP analysis is 20% for iron analysis and 15% for manganese. Given these possible errors, the samples which showed a ratio above 1 were analyzed to see if they were within this margin of error. For iron extraction, there were three samples above this error. These three samples were from a depth 12-13 meters and at 23-24 meters and for well ML1 and for well ML2 at 23-24 meters. For manganese, the ground sample for ML1 at 6.15-6.4 meters, 12-13 meters and well ML2 at 23-24 meters were also too high. For both manganese and iron, concentrations from both wells at 23-24 meters were above this ratio. At this depth the manganese and iron concentrations were both very low. There was also lower manganese concentrations in the ML1 ground sample (6.15-6.4m). The high oxalate value relative to DCB concentration for well ML1 between 12-13 meters for both iron and manganese did not have low concentrations. This sample is from a coarse layer in the aquifer where there was very little fine-grained sediment.

The amount of amorphous and crystalline iron and manganese oxide in the sediment was converted to g/100 grams soil (wt. %) based on the fraction <125μm for each sample. The ground sample included the bulk material and thus included all sediment size fractions. Figure 4.12 shows the relationship between amorphous and crystalline iron and manganese content compared with XRF and XRD results. The concentration of amorphous iron varies between 0.03 and 0.43 wt. % and crystalline iron oxide varies between 0 and 0.14 wt. %. The concentration of amorphous manganese oxide varies between 0.001 and 0.003 wt. % and crystalline manganese oxide varies between 0 and 0.002 wt.%. Figure 4.12 shows that the amorphous fraction of iron in wt. % has a maximum concentration in the unsaturated zone or along the groundwater table before decreasing with depth.

The amorphous manganese oxide ranges between 0.001-0.004 wt. % in ML1 and between 0.002-0.010 wt. % in ML2. Crystalline manganese ranges between 0.0-0.002 wt. % in ML1 and ML2. The peak manganese content is for 6.95-7.2 me in ML1 and at 6-6.4 meters for ML2. Both iron and manganese oxide extraction generally show elevated amorphous concentrations above or towards the top of the groundwater table.

	Depth	DCB Mn(mg/L)	DCB Mn(mg/g soil)	Oxalate Mn(mg/L)	Oxalate Mn(mg/g soil)	Ratio DCB/Ox
ML1	3.6-3.85	2.97	0.15	0.81	0.08	0.55
	5.15-5.4	1.27	0.06	0.59	0.06	0.93
	6.15-6.4	1.48	0.007	0.86	0.09	1.16
	6.15-6.4*	0.49	0.02	0.45	0.05	1.86
	6.95-7.2	4.97	0.25	2.57	0.26	1.03
	12-13	9.83	0.49	14.67	1.47	2.98
	23-24	1.90	0.10	0.67	0.007	0.72
ML2	4-4.2	0.70	0.04	0.39	0.04	1.11
	6-6.4	12.02	0.60	6.20	0.62	1.03
	8.5-8.75	13.04	0.65	6.87	0.69	1.06
	12.25-12.5	4.03	0.2	1.90	0.19	0.94
	23-24	1.83	0.09	0.64	0.06	0.70

Table 4.4: Manganese concentrations from oxalate and DCB experiments. Each sample depth is the average value based on three replicas. Concentrations in mg/L were determined from ICP-Analysis by Eurofins and mg/g dry soil was determined using equation Equation 3.5. The sample marked by * was ground.
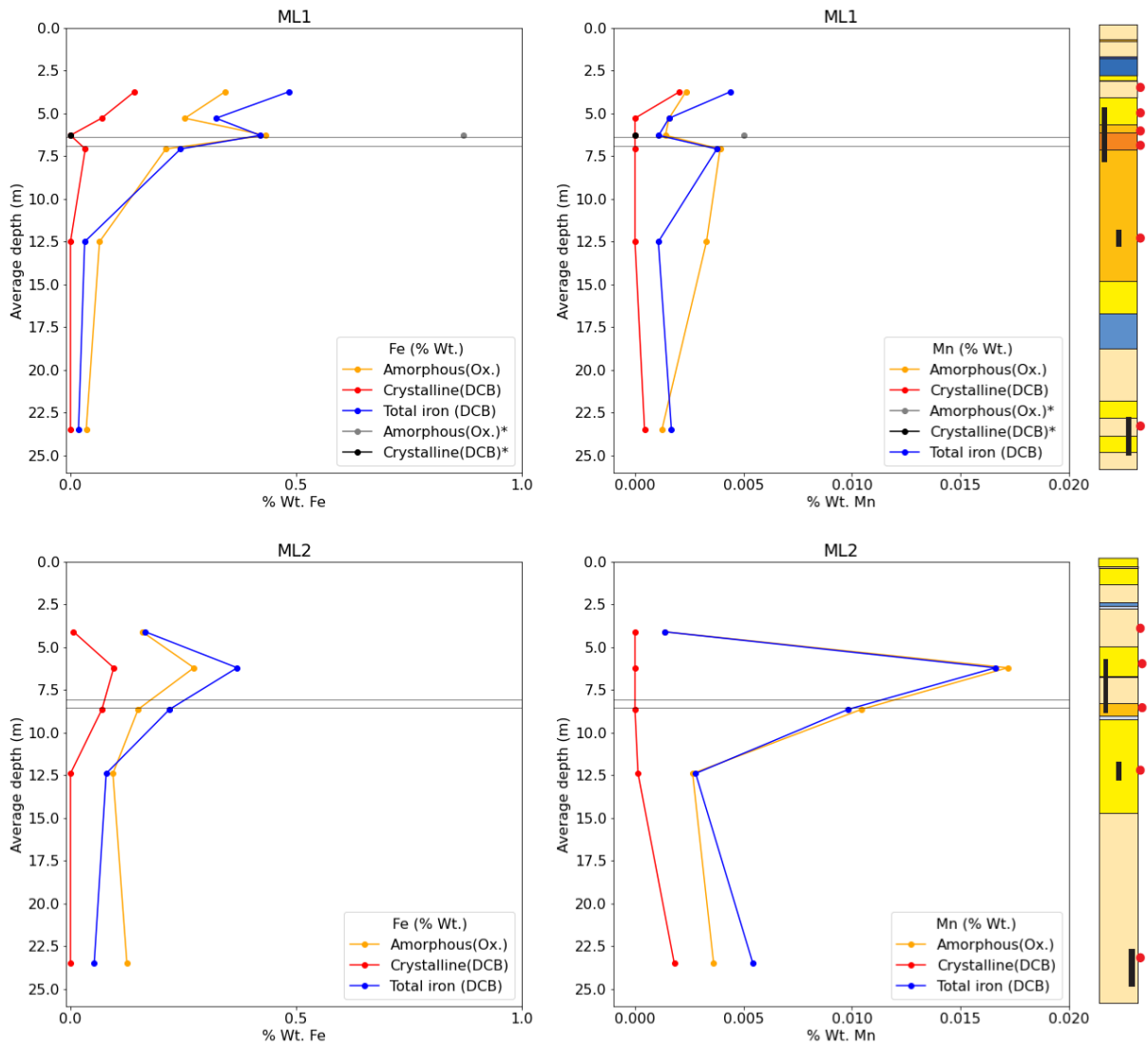
Figure 4.12: Results of extraction experiment for samples from wells BR-ML1 and BR-ML2 for manganese and iron. The top right figure includes results from a ground sample (Amorphous(Ox)* and Crystalline(DCB)*). The schematic well to the right shows red sampling points for samples used for extraction. The min and max groundwater depth from the uppermost filter for each respective well is shown as black lines.

4.2 Meteorological data

Average daily values of precipitation, temperature and snow cover based on data between Sept. 1st, 1990 and May 31st, 2022 is shown in Figure 4.13. Based on average temperatures between 1990-2022, the temperature drops to freezing in late November and remains around -5°C until mid March (Figure 4.13). Snow generally starts in November and snow melt begins in mid March when temperatures increase above 0°C.

The winter season between 2020-2021 was generally warmer than usual between December and January, where temperature oscillated between zero degrees Celsius. The oscillating values around zero degrees between December and January correspond with fluctuating levels of snow depth (0-10cm) prior to January. The temperature remains largely below zero between January and until late February when temperatures rise above zero. A decrease in snow depth at the end of February corresponds to a precipitation event that occurs in late February. Snow depth drops from approximately 65 inches in late February to 2cm in mid March. From mid March the temperature remains above zero degrees Celsius, which is consistent with the historical trend. A precipitation event increases snow cover in mid march. The snow cover drops steady from mid March and is gone by April.

The winter season of 2021-2022 was generally low precipitation. Snow depth in year 2021-2022 increases from late November and remained until mid March. Snow melt begins to decrease gradually from early February through mid March. Total snowfall was reported to be lower than average at Oslo Airport and therefore may be overestimated by the Ukkestad weather station used in this study [Grotthing, 2022]. There was a lot of precipitation in October but precipitation is otherwise low between December and through April. Between the months of December and March the temperature is mainly below freezing but it fluctuates between 5°and -10°C.
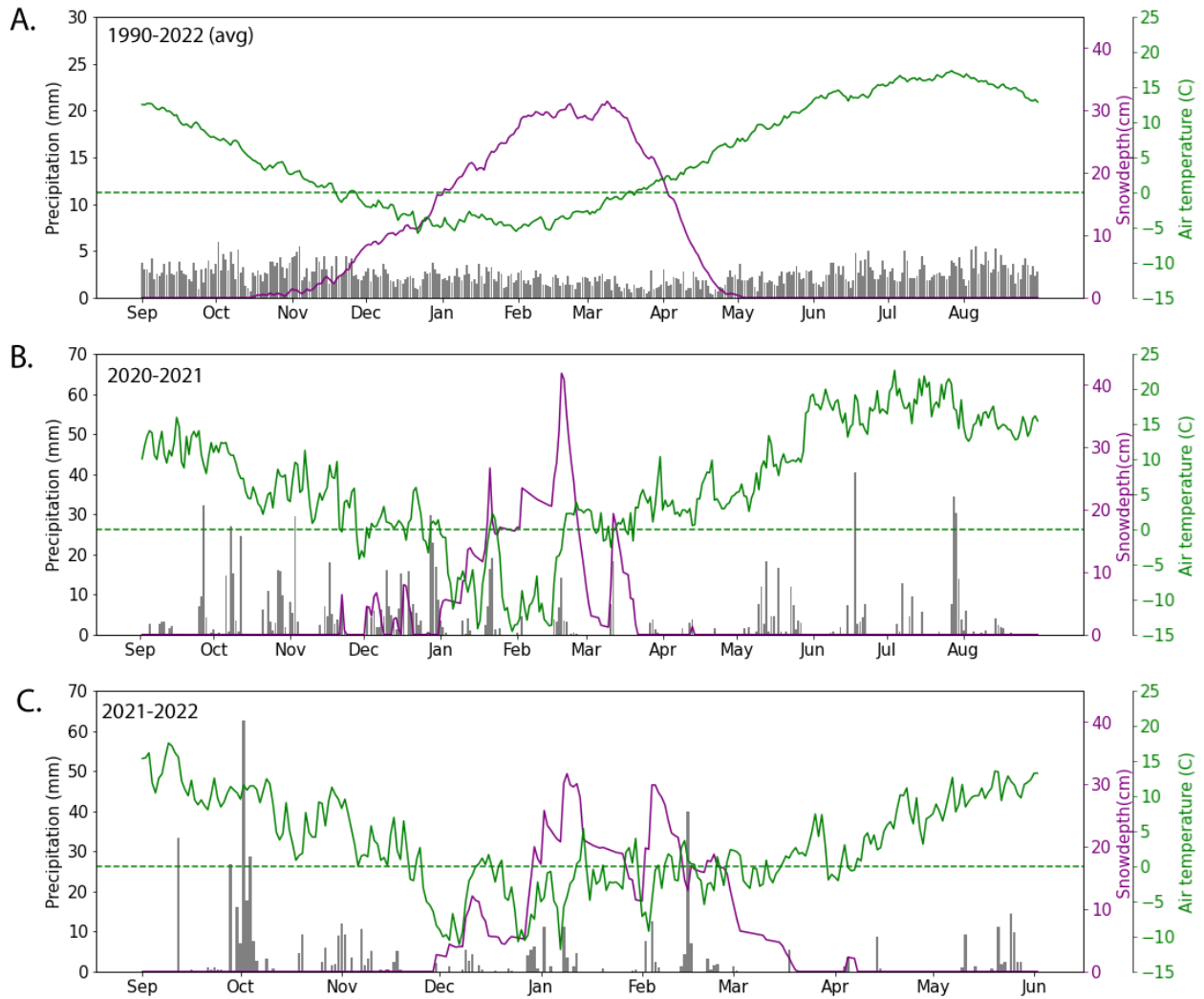
Figure 4.13: A) Average daily values of precipitation (gray), temperature (green) and snow depth (purple) data based on data between Sept. 1st, 1990 and May 31st, 2022. Dotted green line shows temperature at 0°C. B) Average daily values of precipitation, temperature and snow cover between Sept. 1st, 2020 and Aug 31st, 2021. C) Average daily values of precipitation, temperature and snow cover between Sept. 1st, 2021 and May 31st, 2022. Precipitation and temperature data is from Gardermoen station 4780 N and retrieved from xww.xgeo.no. Data from snow depth data was from 4740 Ukkestad weather station, approximately 3 km south-east of Oslo Airport. Precipitation and temperature data is collected from a station at Oslo Airport, station 4780 GARDERMOEN, located north of the study area.

4.3 Groundwater analysis

4.3.1 Water chemistry

The results from groundwater chemistry analysis for both the August and November campaigns are detailed in Table A.1. The electrical Balance (E.B.) was above 5% for in the August campaign for well ML1 for Filters A and C and for well ML2 Filter A (Table 4.5). ML2 Filter A showed the highest E.B. of 17.22% and was the only filter to exceed the desired maximum 15% E.B. limit. The E.B. values from the November campaign were lower than for August. All filters for both wells ML1 and ML2 were below 5% except ML1 Filter B, with a value of 7.4%.

Both major ions and minor are shown in Figure 4.15 and Figure 4.16. Deicing chemicals propylene glycol, formate or the degradation product acetate were not found within the detection limits. The pH was not measured during the August campaign as Avinor was awaiting a replacement instrument. In November, the pH in ML1 in November was between 6.67 and 7.22 (Table 4.5). The highest pH is in Filter B and the lowest in filter C. For well ML2, the pH increases with depth and has a range of 6.22-7.48.

The alkalinity is generally high in both sampling campaigns, with values ranging between 42.1 to 604.1 mmol/L. For both wells, Filter B contains the highest alkalinity levels compared to other filters in both campaigns. There are evident differences in alkalinity between ML1 and ML2. ML1 has higher alkalinity for Filters A and B compared to ML2 for both sampling months. In comparison, Filter C is lower for both months in ML1 compared to ML2. The lowest alkalinity values is found in the top filter of ML2 for in August and November. There are also differences between the two campaigns for each well. In ML1, there is an increase in alkalinity in Filter A from August to November. However, there is a decrease in alkalinity between these campaigns in Filter B. Filter C shows only a very small increase in alkalinity. ML2 exhibits similar trends for Filters A and B. There is a small increase in alkalinity in Filter A and a decrease for Filter B from August to November. Filter C shows a small decrease in alkalinity. Alkalinity is presented in units of meq/L in Figure 4.15 and is simplified to assume it is entirely bicarbonate (HCO_3^-).

A piper plot of the groundwater shows that the water type differs between wells. Well ML2 has a Ca^{2+}/HCO_3^- groundwater type. For well ML1, Filters A and B have elevated concentrations of sodium and potassium. ML1 Filter A in particularly is dominated by Na^+ and K^+.

Major cations in the groundwater include calcium, potassium, magnesium and sodium. Calcium is the dominant cation in all filters except for in ML1 filter A. There is very little variability in calcium for ML1 between the two campaigns and some variability in ML2. The highest levels of calcium are found in filter B for both ML1 and ML2. In ML1 filter B, calcium is 6.5 meq/L for both campaigns and in ML2 it decreases to 5.0 meq/L to 4.4 meq/L. The lowest calcium levels are found in ML1 filter A, with a value of 0.16 meq/L for both campaigns. Similar to ML1, ML2 Filter A has the lowest calcium levels in the well. There is a slightly lower

| | Aug | | | | | | Nov | | | | | |
| | ML1 | | | ML2 | | | ML1 | | | ML2 | | |
	A	B	C	A	B	C	A	B	C	A	B	C
Alk (mmol/L)	128.1	604.1	103.7	42.7	384.4	183.1	230.6	466.8	111.1	67.7	327.1	172.7
pH	n.a.	n.a.	n.a.	n.a.	n.a.	n.a.	6.76	7.22	6.67	6.22	6.68	7.48
E.B. (%)	13.22	1.8	10.14	17.22	0.78	3.81	4.89	7.37	1.48	1.93	0.80	-1.53

Table 4.5: Electrical balance, pH and alkalinity for water samples from the August and November campaigns for multilevel wells ML1 and ML2 (Filters A, B and C).
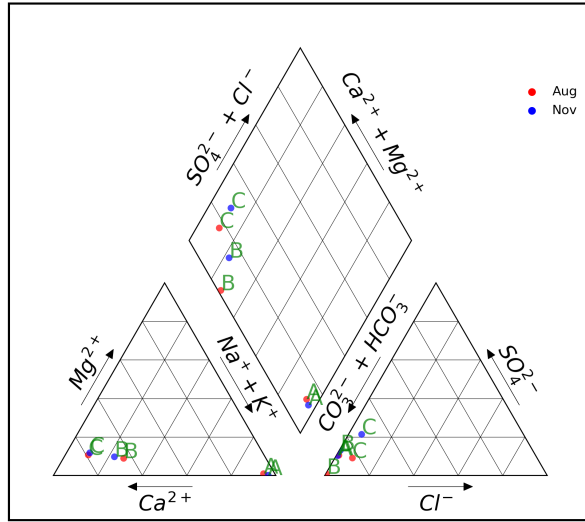
(a) ML1
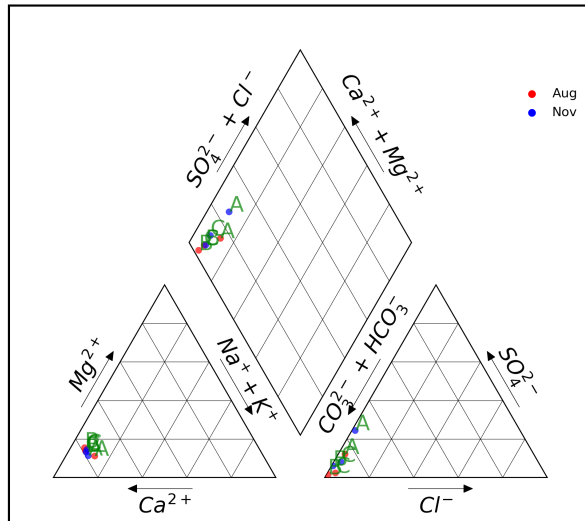
(b) ML2

Figure 4.14: Chemical composition of August and November groundwater samples from multilevel wells ML1 and ML2 and respective filters (A, B and C) plotted in a Piper Diagram. Each of the triangular plots shows cations (bottom left), anions (bottom right) in percentage of total meq/L. The top diamond shows the extrapolation of anion and cation values.

level of calcium in ML1 Filter C compared to ML2 Filter C. The calcium concentration in ML1 Filter C is approximately 2 meq/L for both campaigns.

There are high concentrations of potassium in ML1 Filter A and B. The highest concentration is in ML1 A in November and the second highest value is in ML1 Filter B in August. In ML1 Filter A, there is a significant increase in potassium from August (1.5 meq/L) to November (2.6 meq/L). In ML1 Filter B, the concentration decreases from August (1.7 meq/L) to November (1.1 meq/L). Potassium concentration levels are much lower in the other filters for ML1 and ML2. The next highest recorded concentrations are for ML2 filter B in August (0.15 meq/L) and November (0.13 meq/L). All other filter concentrations are below 0.1 meq/L.

Similar to potassium, the highest concentrations of sodium are in ML1 filter A and B. Concentrations are the highest in filter A, with a value of 1.5 meq/L in August and 1.8 meq/L in November. The concentration is slightly lower in ML1 Filter B, with a value of 1.1 meq/L for both campaigns. The lowest concentrations are found in ML2 Filter A, with a concentration of 0.1 meq/L for both campaigns. In ML2 Filter B, concentrations remain around 0.3 meq/L. Sodium concentrations in ML1 and ML2 Filter C are approximately 0.2 meq/L for both campaigns.

Values of magnesium are highest in ML1 and ML2 Filter B, with values ranging from 0.8-1.0 meq/L. ML1 and ML2 Filter C has higher concentrations than filter A for both wells. Values of ML2 Filter C are between (0.4-0.5 meq/L) and are approximately 0.3 for both campaigns in ML1. In ML1 filter A, concentrations are below 0.4 meq/L and between 0.1-0.2 meq/L in ML2 Filter B.

Major anions shown in Figure 4.15 include bicarbonate, sulphate, chloride, nitrate and nitrite. Bicarbonate is assumed to be the dominant species in determining the alkalinity in these samples and is the most significant anion in meq/L in all samples. Sulphate is also an important anion in Figure 4.15. The highest concentration of sulphate is found in ML1 Filter B in November (1.2 meq/L) with other samples significantly lower. November sulphate concentrations are higher for all filters.

There are low concentrations of chloride and nitrate/nitrite for both wells. For chloride, concentrations were relatively similar between each filter for ML1 and ML2. There was a general increase in chloride with depth for both wells for Filters A (approximately 0.02 meq/L), Filter B (0.03-0.04 meq/L) and Filter C (0.1-0.2 meq/L). In the August campaign nitrite and nitrate were combined in the analysis whereas in the November campaign only nitrate levels were analyzed in the lab. Levels of nitrate are low and close to the detection limit in both wells. The highest levels are mainly registered in the top filter for both ML1 (0.001-0.050 meq/L) and ML2 (0.04-.0.06 meq/L). Low nitrate levels of 0.005 meq/L were also found in the November campaign in Filter B in both wells. There was also low nitrate concentration found in ML1 Filter C of the August campaign. Silica levels reach a high of 19 mg/L in filter B.

Iron, manganese and total organic carbon (TOC) concentrations can be found in Figure 4.16. Values are listed in mg/L rather than meq/L given the multiple oxidation states of manganese. TOC, which was only determined in the August campaign, was highest in top two filters of ML1. Iron concentrations are highest in ML1 Filter B for August and November (4.6 mg/L and 17.2 mg/L). Concentrations in ML1 Filter A are approximately 2 meq/L and an order of magnitude lower in Filter C both campaigns. Similar to ML1, the highest iron concentrations in ML2 are in Filter B, with a higher concentration in November (3.2 meq/L) compared to August (1.6 meq/L). In ML2, values are significantly higher in Filter B compared to Filter A and C. There is an increase between ML2 Filter A to Filter C for both campaigns.

The highest values of manganese are found in ML2 Filter B (2.7 and 2.9 meq/L). Concentrations of manganese in this filter are similar to or exceed iron concentrations. Manganese concentrations in ML2 increase by an order of magnitude from Filter A to Filter C. In ML1, the highest concentrations are also found in Filter B (1.9-2.2 meq/L). In contrast to ML2, there is a decrease by an order of magnitude in manganese levels from Filter A to C.
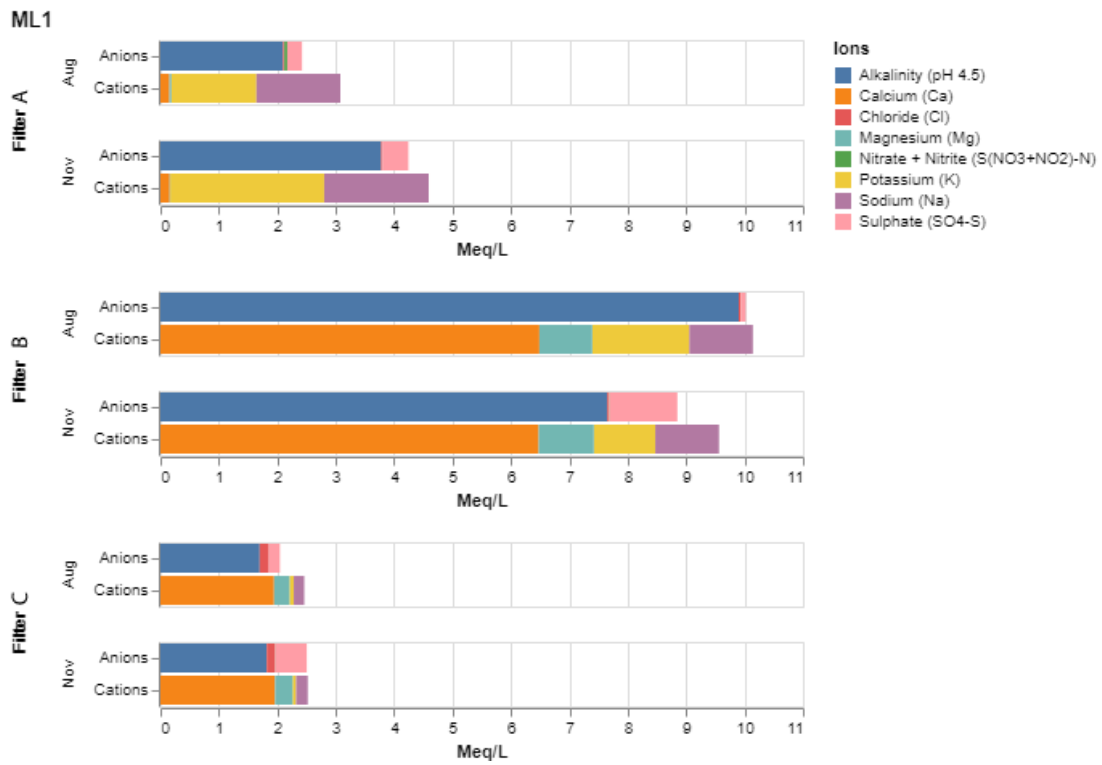
(a) ML1
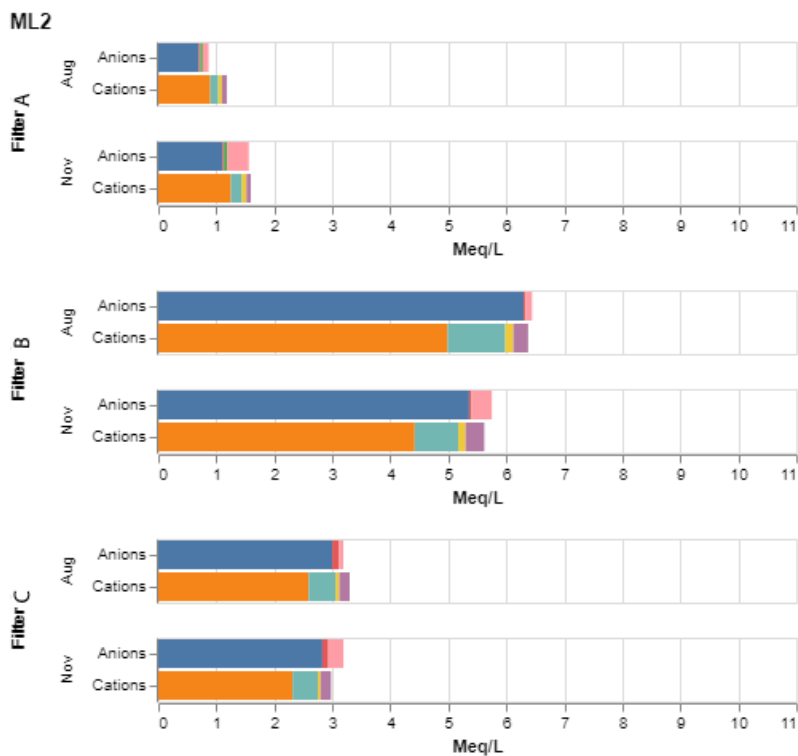
(b) ML2

Figure 4.15: Major cations and anions for (a) well ML1 (Filter A, B and C) (b) well ML2 (Filter A, B and C) for the August and November sampling periods.
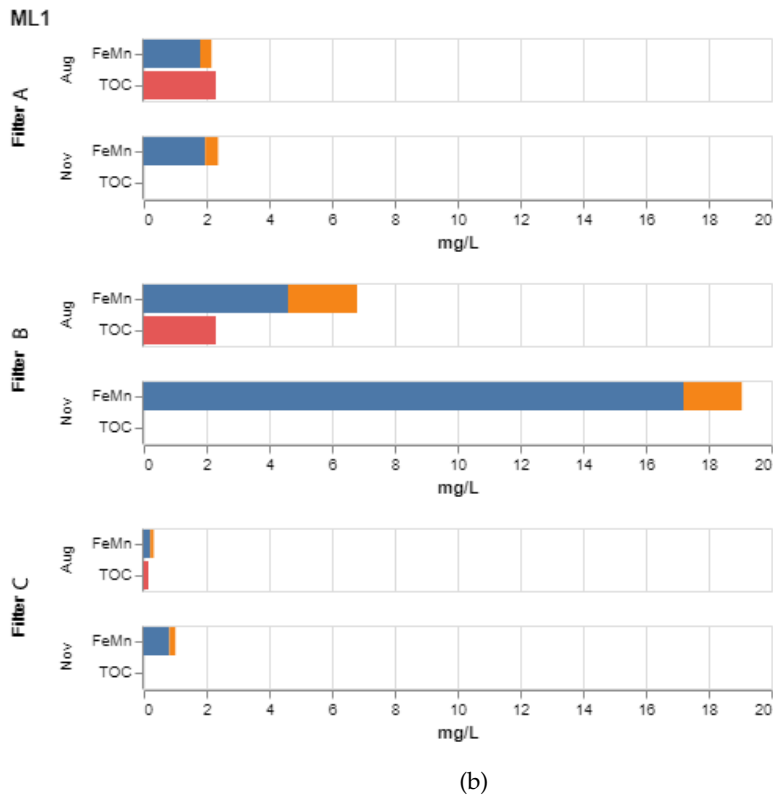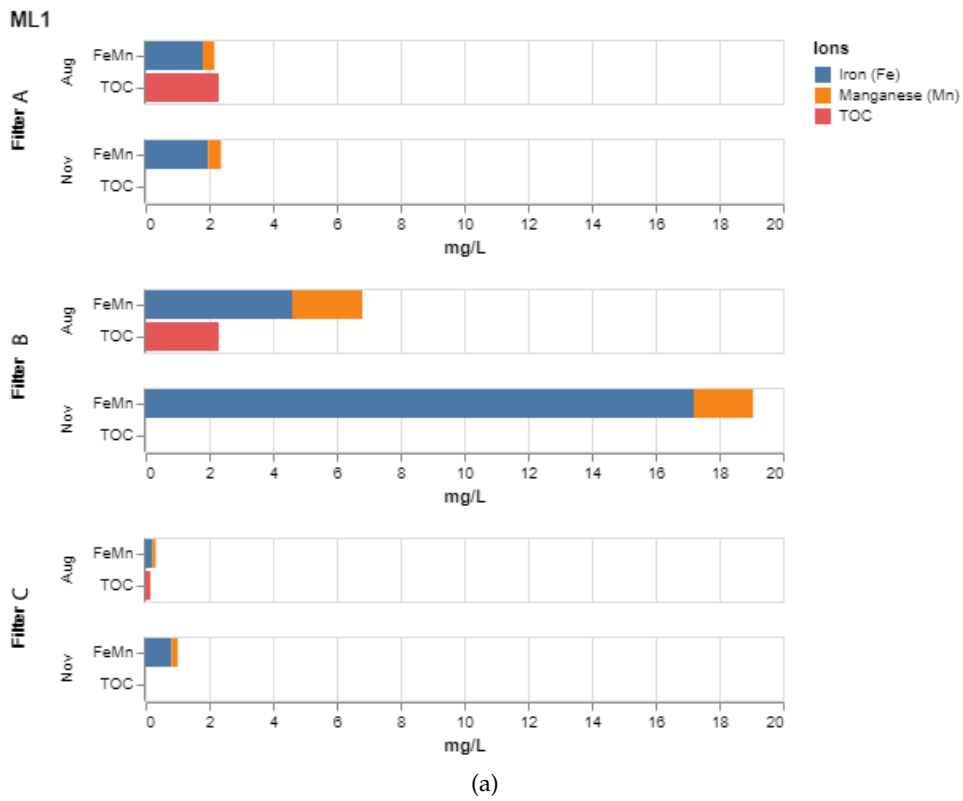
Figure 4.16: Iron and manganese concentration for (a) well ML1 (Filter A, B and C) (b) well ML2 (Filter A, B and C) for the August and November sampling periods in mg/L. TOC (mg/L) is included only for the August sampling period.

4.3.2 Hydraulic head

Manual measurements taken with a Water Level Meter are found in Table A.12. Based on data sampling taken on Nov. 23rd, 2021 and April 5th, 2022 the average difference in hydraulic head between ML1 and ML2 Filter A is 0.715m. Given an distance of 167m between multilevel wells ML1 and ML2, the approximate hydraulic gradient from ML1 to ML2 is $-4.28 * 10^{-3}$.

Figure 4.17 shows the hydraulic head for wells ML1 and ML2 for the three respective filters based on the water pressure sensor data. Additionally, Figure 4.17 shows additional precipitation and air temperature for the same time period. Data from the water pressure sensors (divers) indicate that trends in hydraulic head measurements was similar between the filters for both wells.

For ML1, there was a lot of noise associated with the diver data. The barometer was located in ML2, which may be why ML2 did not experience similar micro-fluctuations as ML1. Another hypothesis is that because ML1 was closer to the runway, the instruments could have been affected by flight traffic. To reduce the noise of the diver data in ML1, a mathematical smoothing function called LOWESS (Locally Weighted Scatterplot Smoothing) was used Figure 4.17.

The hydraulic head in ML1 and ML2 plateaus between November and December before gradually decreasing. There was a period of higher precipitation in Sept-Oct of up to 14 mm/day. This higher precipitation is correlated with an increase in hydraulic head in ML1 in October, which is evident in all three filters. The measurement period for ML1 began in November so it is missing October data. Towards the end of November there is a drop in temperature and from mid November the groundwater table gradually declines in both all filters for ML1 and Ml2. There is a slight increase in hydraulic head which is evident over the coarse of approximately five days between late February and early March that is visible in all six filters.

There is a lower hydraulic head in ML1 compared to ML2 with respect to all filters. The minimum and maximum hydraulic head of ML1 varies between 193.9 and 194.5 (with respect to all three filters). For the three filters of ML2, the hydraulic head varies between 193.2 to 193.7. Both the diver data and manual measurements show a slight reduction in hydraulic head between the top two filters and the bottom filter in ML1. The hydraulic head measured by the diver data for ML1 indicates that there is an approximate 20cm difference between the filter C and filter B. Similar to ML1, the manual measurements shows that Filter C has a slightly lower hydraulic head with an average difference of 3.43cm between Filter A and B. This manual measurement data therefore shows a much smaller difference between hydraulic head of the bottom filter compared with the top filter.

For ML2, the diver data shows that the hydraulic heads of the filters are within 10cm of each

| Well | Filter | Hydraulic head (m.a.s.l) | | Depth (m) | |
		Min	Max	Min	Max
ML1	A	194.04	194.52	6.40	6.88
	B	193.97	194.47	6.45	6.95
	C	193.85	194.31	6.62	7.07
ML2	A	193.22	193.64	8.08	8.51
	B	193.27	193.72	8.00	8.45
	C	193.25	193.67	8.05	8.47

Table 4.6: Hydraulic head (m) and groundwater depth below surface. The values are expressed as the minimum and maximum values recorded by water pressure sensors for Filters A, B and C in multilevel wells ML1and ML2.
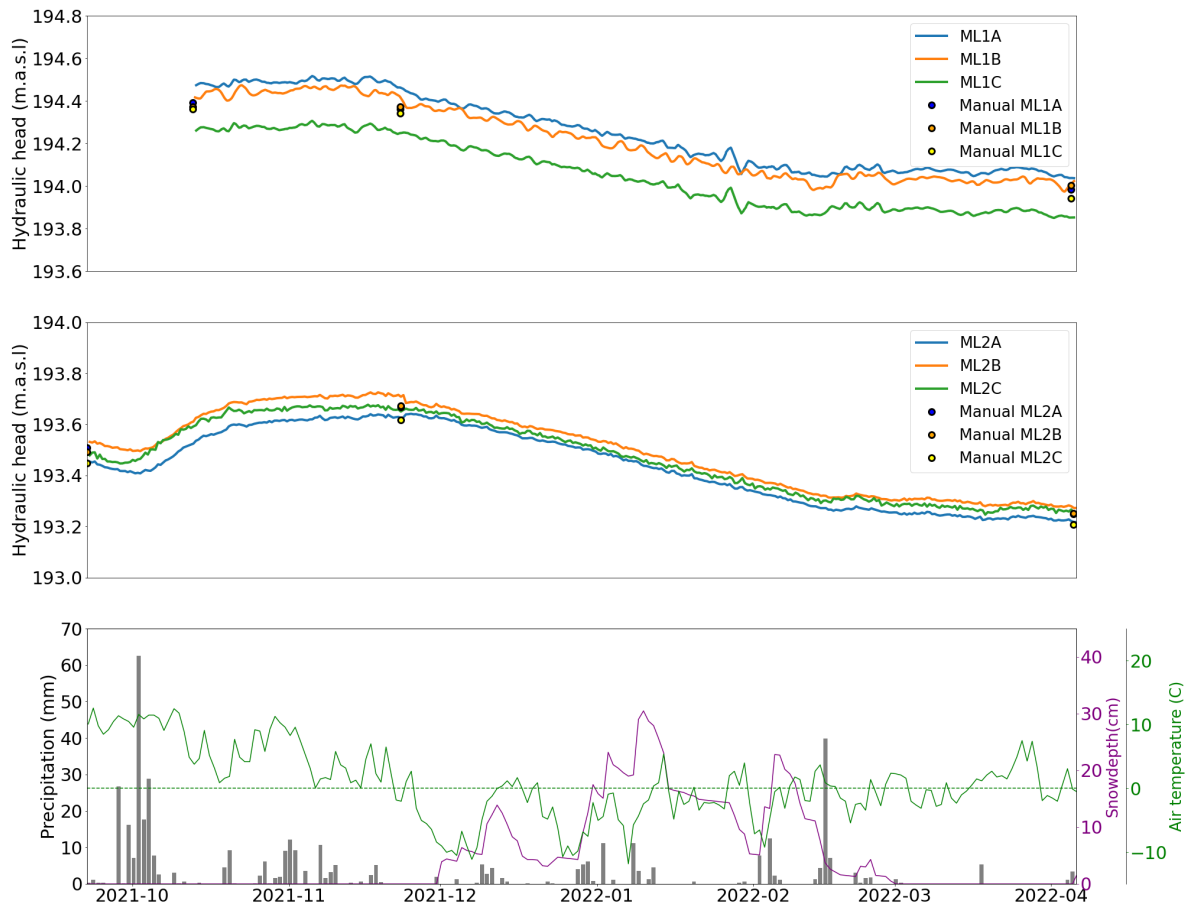
Figure 4.17: Groundwater diver data between Sept. 22, 2021 and April, 5th, 2022. Diver data for well ML1 begins Oct.13, 2021. Precipitation and temperature data is from Gardermoen station 4780 N and retrieved from www.xgeo.no.

other. Thus, the divers show a close correlation in hydraulic head relative to each other. The manual measurements at all three sampling points shows that there is a slightly lower head in the third filter relative to the top two filters, with a an average difference of 4.74cm between Filter B and Filter C. The lower hydraulic head in the manual measurements is not supported by the diver data, which shows that Filter C has a hydraulic head that is similar to the top two layers. Figure 4.17 shows that ML2 Filter C has a slightly higher hydraulic head compared to Filter A, however this assumed to be within the margin of error.

The temperature data shows variations between the filters and wells. In ML1, the top two filters increase temperature gradually. Filter A increases from a temperature of 8.60°C on Oct. 13th to a high of 10.14°C on Jan. 1st before gradually cooling to a temperature of 9.31C on April 5th, when the divers were collected. Filter B has a more gradual increase from 8.46°C on October 10th and reaches a maximum of 9.29°C on March 4th. Following this period, the temperature in Filter B remains fairly steady with a temperature between 9.29°and 9.22°C through the end of the monitoring period on April 5th. Filter C maintains a relatively stable temperature, with a slight increase from when monitoring begins to when it ends from 8.25°C to 8.38°C. Thus, Filter C maintains a colder temperature than the top two filters. There were some short-term temperature jumps and drops that are visible in filter A and B in Figure 4.17. The first occurs on November 23rd in Filter A when the temperature jumps up for the day from 9.81°to 10.00°C and there is a smaller jump in temperature in Filter B from 8.91°to 9.00°C on Nov. 23rd. The preceding rainfall occurred on Nov. 17th with a total of 5.5mm of rain. Both

67

the top two filters in ML1 show that on March 18that there was a brief drop in the temperature. Filter A dropped from 9.55°to 8.50°C on this day and for Filter B a smaller drop occurred on March 18th from 9.29°to 8.91°C. This was preceded by 3.9mm of rain on March 17th.

In ML2,the three filters maintain lower temperatures than in ML1. Additionally, there is less variation between the three filters in ML2 compared to ML1. Filter A has a temperature of 6.89°C when monitoring begins September 22nd and increases to a maximum of 7.70°C January 21st. The temperatures then decreases to a minimum of 7.45°C when the divers are collected April 5th. Similar to ML1, the increase is smaller for Filter B compared to Filter A. ML2 Filter B starts at a temperature of 7.15°C and increases to a temperature of 7.5°C on February 2nd and remains only slightly cools to a temperature of 7.47°C on April 5th. Filter C remains fairly constant. It has a starting temperature of 7.23°C and gradually increases to 7.27°C at the end of the monitoring period. Similar to in ML1, there is a slight jump in temperature that is visible in Filter A on Nov. 11th, where there is a small jump from 7.38°C to 7.45°C, which lasts a day. There is a drop in temperature that is seen in Filters A and B in early March. On March 2nd, the temperature drops from 7.60°C to 7.41°C and rises back again March 5th. Similarly, the temperature drops to 7.38°C from 7.45°C on March 2nd before rising again on March 4th.

4.4 Western runway: Sedimentary and chemical data

4.4.1 Sedimentary layers

Results from the grain size analysis for boreholes ML1, ML2, JordB and JordC were combined with previous borehole logs from Avinor and based on results from Hansen et al. [2020a]. Figure 4.18 shows groundwater wells near the western runway which have been projected along the groundwater line found in Figure 3.1.
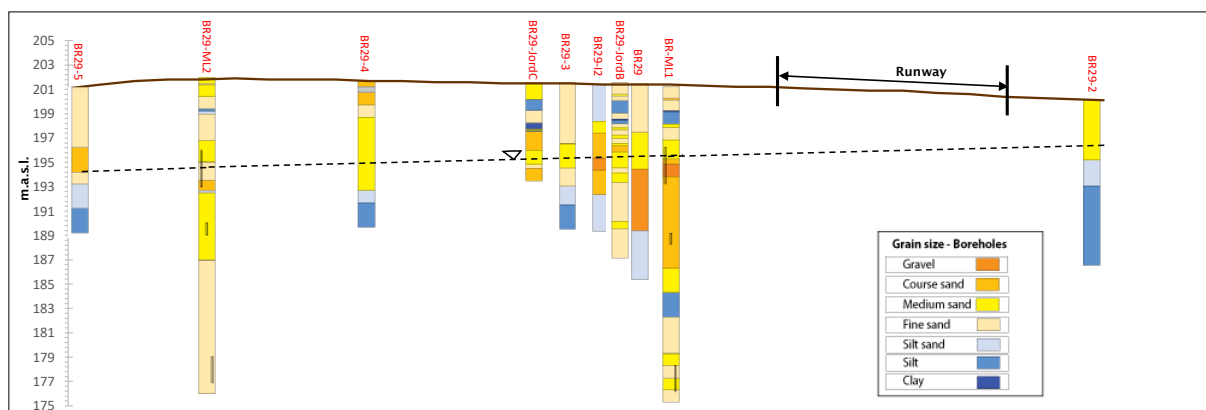
Figure 4.18: Cross section of boreholes near the western runway of Oslo Airport projected along the groundwater line shown in Figure 3.1. Results of the additional logs have been published previously [Hansen et al., 2020b].

A cross section of sedimentary layers was created for wells closest to the groundwater flow path Figure 4.19. All wells were included from Figure 4.18 except for boreholes JordC and JordB, which are further from the groundwater flow path (Figure 3.1). Two differing interpretations are shown of the combined sedimentary layers. In Figure 4.19 both (a) and (b) include three general sediment categories. The first category includes both gravel and coarse sand. The second includes medium to fine sand and the final category includes silty sand, silt and clay. In Figure 4.19 (a), the silt layer is joined with the other boreholes. This silt layer spans a large portion of the aquifer. There was only a small silt layer found in ML2 and thus the silt layer narrowly joins at this point. This interpretation then divides this area into three
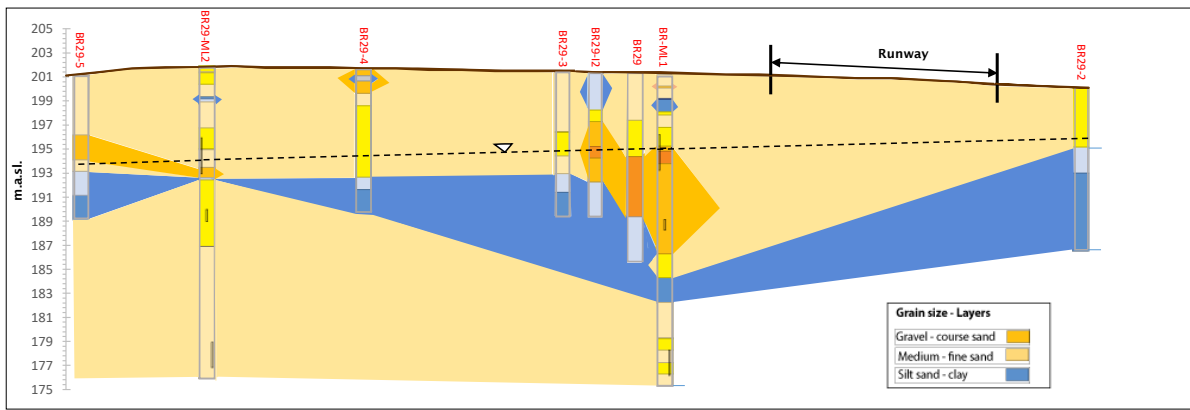
(a)
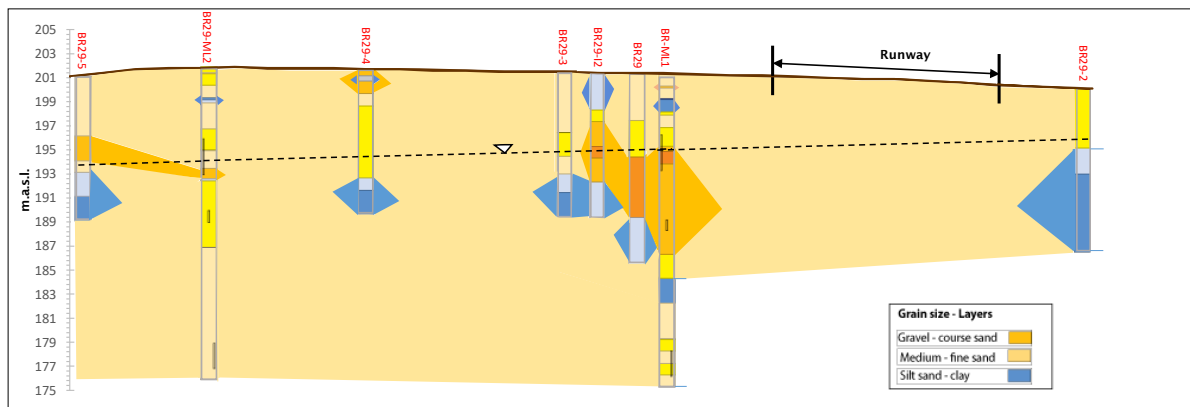
(b)

Figure 4.19: Cross section of boreholes near the western runway of Oslo Airport projected along the groundwater line with sediment samples divided into three grain size groupings. Figure a) shows the silt-sand to clay grain sizes connected accross boreholes. b) Creates silt-clay lenses instead of connecting the silt-clay layers.

distinct layers based on grain size. The top layer is primarily fine to medium sand. The top layer is between approximately 201-193 m.a.s.l between BR29-5 and BR29. The depth of the top layer increases between ML1 to BR29-2 to a depth of 185 m.a.s.l. In the top layer there are also stretches of gravel-coarse sand. Between BR29-I2 and BR-ML1 this layer rests directly on top of the low permeability layer. JordC and JordB also has coarser sediment in this area. Between approximately 193-183 m.a.s.l there is a lower permeability layer. The low permeability layer connects all the wells, but is much narrower in ML2 compared with the other wells. Below the low permeability layer is a new layer of medium-fine sand. In Figure 4.19 (b) the silt layer is no longer connected. Thus, the silt layers make up low permeability lenses.

4.4.2 Dissolved iron and manganese near the western runway in 2021

For the season 2020 through 2021, deicers started in early fall. Potassium glycol started 10th of October and formate started on the 11th of November. Methane was detected in 34m (BR29-B2) downgradient of the runway in April and June.

Figure 4.20 shows iron and manganese concentrations during the season 2020-2021. In January there is an iron concentration of 13 mg/L in January in a well 20 meters downgradient of the runway (BR29). A hightened iron concentration of 11 mg/L is also seen in January

34 m downgradient (BR29-B2). At 44m downgradient (BR29-3) the concentration drops to 2 mg/L and for all wells 216 m downgradient (BR29-5) the concentration remains below 1 mg/L. In February there is a decrease in iron in all wells. The concentration in BR29 is at 9 mg/L. In March there is a slight increase in the concentration of iron 44m downgradient of the runway, which increases from 5.8 to 8.3 mg/L from February to March. In April there is an increase in iron concentration levels 44m downgradient of the runway (BR29-3). In April iron concentrations are low (<1mg/L) 114m - 216m downgradient of the runway. In May there is an increase in iron concentrations 34m (BR29-B2) downgradient of the runway from 5.4 mg/L in April to 10 mg/L in May. This increase in iron concentrations in May is also seen 44m (BR29-3) downgradient of the runway, where there is an increase from 11 mg/L in May to 17 mg/L in April. Iron concentrations reach 17mg/L 44m downgradient in June. September concentrations are only recorded for wells 114m and 216m downgradient, which remain low (<1mg/L).

The iron concentrations sampled in ML1 and ML2 in Filter B are also shown in Figure 4.20. The values in ML2 are higher than values recorded for the other wells. THe ML1 August sample is as high as maximum concentration of 17 mg/L reached 44m downgradient in June.

The manganese concentrations in January through June remain less than 2 mg/L between 20m (BR29) and 34m (BR29-B2) downgradient. Heightened manganese concentrations are observed 44m downgradient (BR29-3) for most sampling months and drop to lower concentrations (<1mg/L) 114m downgradient of the runway. The concentration of manganese at 44m downgradient form the runway follows a similar trend to iron for the January - June sampling periods. In January, the concentration of manganese is at heightened concentration of 3.2 mg/L. The concentration drops in this well in February and March and increases May to 6.3 mg/L and 9.3 mg/L in June.

The manganese concentration in both ML1 and ML2 Filter B in both the November and August sampling periods is higher compared to wells at a similar distance downgradient of the runway.
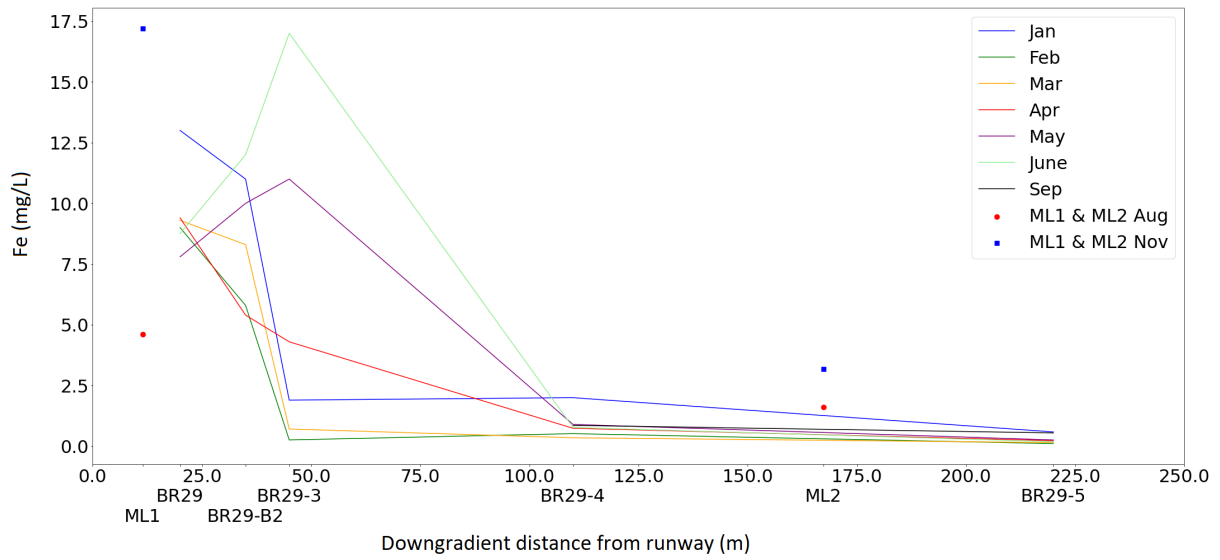
(a)
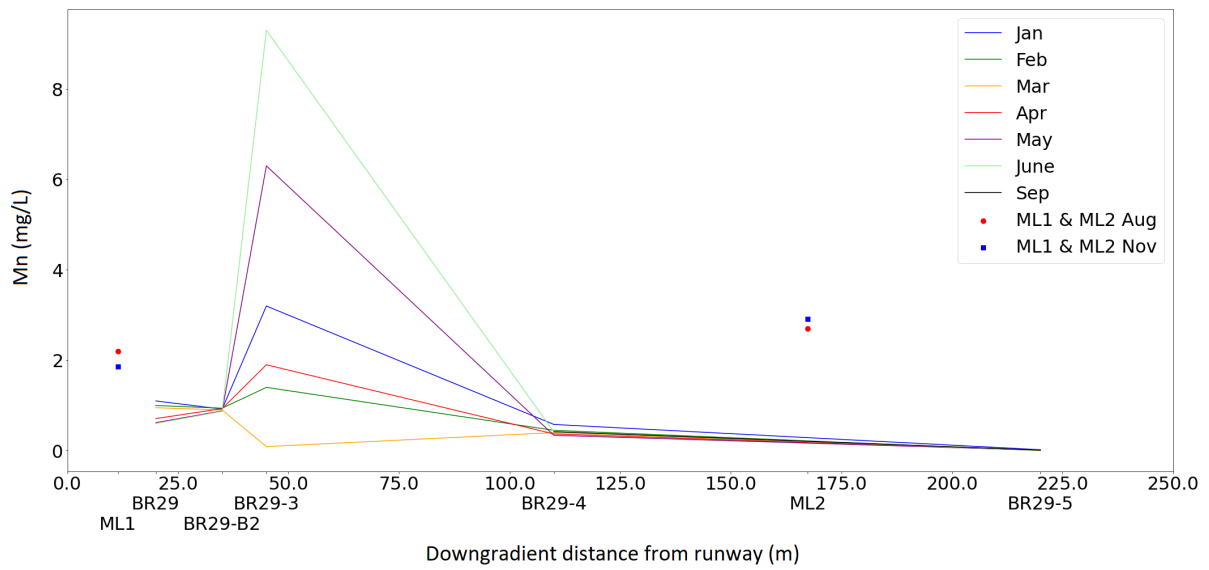
(b)

Figure 4.20: Trend in iron and manganese over the course of 2020-2021 using historical data from Avinor including two well points.

4.5 Geochemical modeling with PHREEQC

4.5.1 Aqueous speciation

The saturation indexes (SI) of the minerals determined from the PHREEQC speciation model is found in Table A.8. Manganese oxide minerals were undersaturated in all samples, including pyrochroite, pyrolusite and $Mn(OH)_2(am)$ (Figure 4.21). The SI of iron oxide minerals ferrihydrite $(Fe(OH)_3)$, hedenbergite and goethite minerals was more varied (Figure 4.21). Goetheite was over-saturated in all samples while hedenbergite was undersaturated. The SI of ferrihydrite ranges between -1 and 1 in the majority of samples. ML1 Filter A in August and November is slightly above this range, both having an SI value of 1.1 . ML1 Filter C in the August sample is below this range with a value of -1.38.
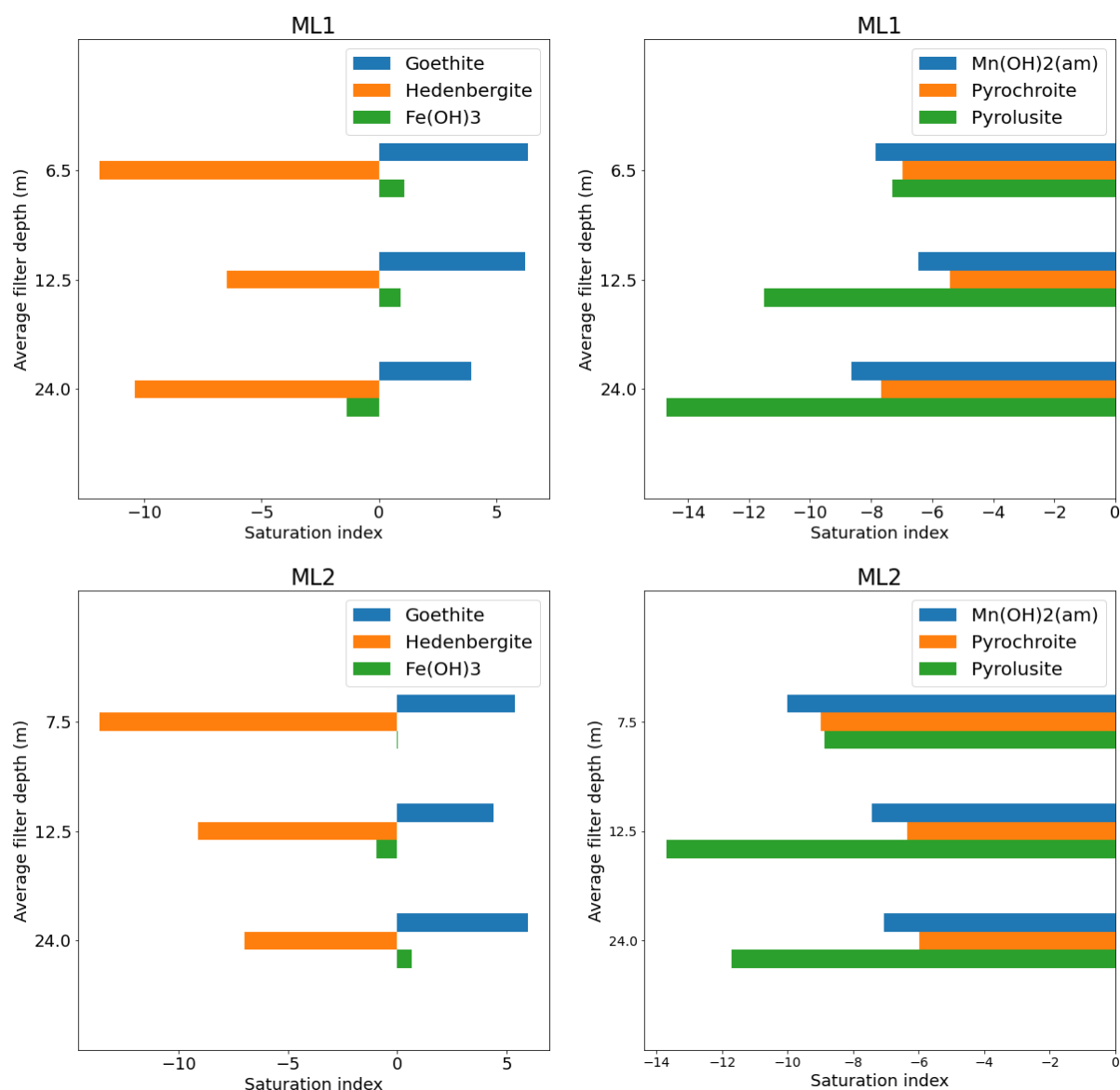
Figure 4.21: Calculated saturation index of iron containing minerals (left column) and manganese containing minerals (right column) with respect to average depth of filters in wells ML1 and ML2 from November data.

There were three samples which did not converge in the speciation model when including aluminum concentrations. For these four filters the aluminum concentration was removed

from the modeling (ML1 Filter A in November and August and ML2 Filter B in August and November) (Table A.7). The SI value of aluminum-based minerals microcline, muscovite and montmorillonite are all over-saturated except for samples which did not include aluminum. Quartz is slightly over-saturated for all samples with a value between 0 and 1. Pyrite and ankerite are undersaturated for all samples. Calcite is undersaturated in all samples except for ML1 Filter B in August and November.

4.5.2 Reaction model with addition of chemical deicers

The output results from the reaction model show that there is a decrease in pE and an increase in pH with the addition of the deicer concentrations Table 4.7. The addition of a higher concentration of deicers (C2) results in a higher pH of between 7.8-7.9 and lower pE values close to zero (C1 and C2 chemical deicer concentrations are found in Table 3.6). The final pE value at lower chemical deicer concentrations (C1) is higher than for C2 but remains below 2.

The reaction model finds there a significant dissolution of ferrihydrite with the chemical deicer input concentrations C1 and C2 (Figure 4.22). Ferrihydrite dissolution in moles with concentration C2 is almost five times higher for both filters compared to the amount dissolved with C1. With C2 the the amount of dissolved ferrihydrite is $4.8 * 10^{-2}$ mol/L and $4.9 * 10^{-2}$ mol/L for Filter A and B respectively. In comparison, the dissolution ferrihydrite is approximately $1 * 10^{-2}$ mol/L for both filters with C1. $Mn(OH)_2$ has a slight precipitation (less than 10^{-5} mol/L for both filters). The output results also indicate an increase in carbon dioxide with respect to deicer concentration. Additionally, there is a slight dissolution of quartz (less than 10^{-6} mol/L) and calcite precipitation (less than 10^{-3} mol/L) for both filters and deicers concentrations.

		Fe^{2+} (mg/L)	Mn (mg/L)	pH	pE
	Initial	2.0	4.1E-01	6.8	7.1
Filter A	C1	5.6E+02	4.7E-02	7.3	1.6
	C2	2.7E+03	1.5E-02	7.8	3.80E-02
	Initial	17.2	1.9	7.2	4.0
Filter B	C1	5.9E+02	7.0E-01	7.5	1.7
	C2	2.7E+03	2.6E-01	7.9	2.0E-01

Table 4.7: Output results from PHREEQC reaction model with addition of deicing chemicals. Addition of deicer concentrations were registered in well BR29 on 12.02.2020 (C1) and 04.04.2019 (C2). Concentration values found in Table 3.6.
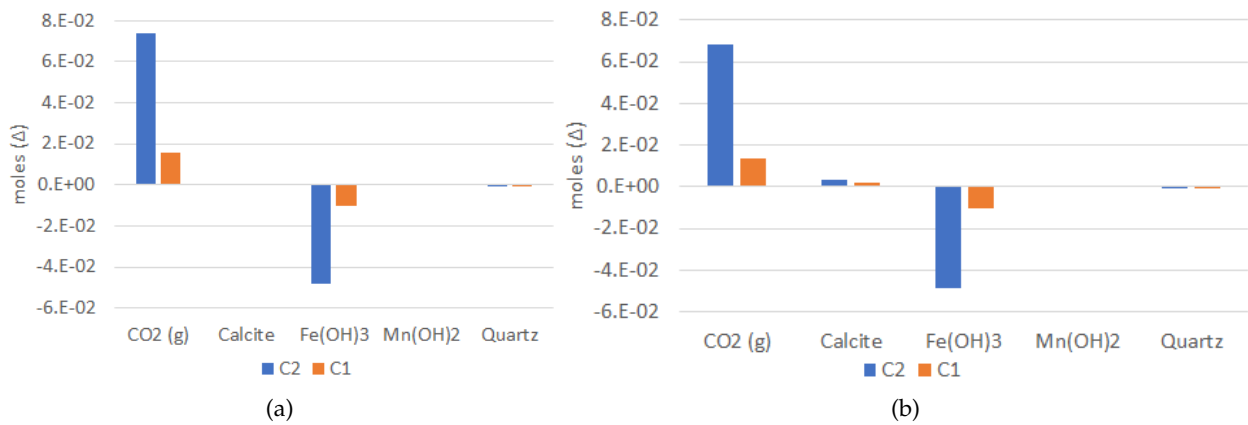
Figure 4.22: Change to mineral phase assemblage with the addition of chemical deicers based on PHREEC reaction model using mineral SI values from well ML1 November sampling campaign. Deicer concentrations used were registered in well BR29 on 12.02.2020 (C1) and 04.04.2019 (C2). For minerals, negative change indicates a dissolution and a positive value indicates precipitation. For CO_2 (g) a positive value indicates an increase in dissolved CO_2 (g) and a negative value a decrease in dissolved CO_2 (g). Concentration values for C1 and C2 found in Table 3.6. Where a) is for Filter A and b) is Filter B.

Chapter 5

Discussion

The discussion first focuses on identifying the likely flow pathways of chemical deicers along the western runway and determining if vertical flow in the saturation zone a probable pathway. To understand these flow patterns, the first section discusses the hydrostratigraphy, diver data and major ion water chemistry of the filters. The following sections are devoted to assessing the sustainability of deicer usage along the western runway based on the effect of the redox state on iron and manganese precipitation and dissolution processes. Sections include analysis of seasonal changes to the redox state based primarily on water chemistry data in 2021, which include data based upon water analysis by the author at the University of Oslo and data collected by Avinor. Additional sections include the estimation of total iron and manganese and the fraction of the respective amorphous oxides in the sediment. The final section is on the sustainability of manganese and iron electron acceptors.

5.1 Flow patterns and mineral dissolution

5.1.1 Hydrostratigraphy

The sediment analysis conducted in this study generally finds finer grained sediment compared to previous stratigraphic analysis done in the proximal areas of the Gardermoen Aquifer. The topset unit, which is predominantly composed of coarse grain sand, was not evident all the four sediment cores. Previous studies have shown that the topset unit is very thin towards the distal zone where the study site is located, as shown in Figure 2.4. The sediment analyzed in this research study, which is between 176 and 202 m.a.s.l., is indicative of the foreset unit. The foreset unit contains a combination of coarse grain to fine grain sand and gravel due to the submarine deposits from suspension fallout and river mouth deposits. The coarser grained sediment above finer grained sediment, as shown for example in well ML1 between approximately 195 and 186 m.a.s.l., is similar to what is also observed in nearby wells BR29 and BR29-I2 at this location. The fining of sediment in foreset beds from coarse-grain and gravel deposits to finer-grained sand is often seen in prograding clinoforms. In the two deepest boreholes, ML1 and ML2, there is a transition towards poorly sorted fine-grained sediment between 174 and 188 m.a.s.l. (ML1) and between 176 and 186 m.a.s.l. (ML2). This transition to more poorly sorted sediment may indicate a transition towards the lower foreset unit which becomes increasingly silty-sandy with depth. The silt and clay rich bottomset unit was not observed in the sediment cores.

The average range of saturated hydraulic conductivity of approximately $10^{-6} \mathrm{m\,s^{-1}}$ is several orders of magnitude lower than predicted by Tuttle [1997] (Figure 2.6). A lower average value for hydraulic conductivity in this area may be because it is also closer to the distal area where sediment is generally finer in the topset and foreset units. The coarse sediment has a K_{max} of $3.7 * 10^{-5} \mathrm{m\,s^{-1}}$, which is closer to the range of $10^{-3} \mathrm{m\,s^{-1}}$ to $10^{-4} \mathrm{m\,s^{-1}}$ predicted

by Tuttle [1997] (Figure 2.6). The lenses of coarse-grained sediment observed in this study area may also provide preferential flow paths that allow for a higher hydraulic conductivity (Figure 4.19). The difference between values estimated by Tuttle [1997] and this research study may also be due to the use of the Hazen equation for calculating hydraulic conductivity, which is less accurate for finer-grained sediment.

5.1.2 Groundwater flow

The groundwater flows in this study area from the direction of the runway towards the ravines. This is evident in the average hydraulic head in the hydraulic gradient of $-4.28 * 10^-3$ between wells ML1 and ML2, assuming groundwater flows parallel to these two wells. From this data, the velocity between Wells ML1 and ML2 and also from to the airport boundary can be estimated with an estimated porosity of 0.36. (Table 5.1). The travel time indicated in Table 5.1 indicates that it may take a minimum of 20.3 years in coarse sediment to travel between the western runway and the airport boundary. There are several reasons why this could be an underestimation of travel time. The hydraulic gradient will additionally affected by precipitation events, which could decrease the travel time. Further, there are lenses of coarser material, such as gravel, which was not included in laboratory sediment analysis.

Diver data shows temporal synchronization and hydraulic heads for all three filters in both wells Figure 4.17. This indicates that they are all similarly affected by the seasonal precipitation and infiltration patterns. The synchronization indicates that there is pressure communication at these depths and there is no true confining layers between the filters.

Both diver data and manual measurements indicate that groundwater flow between multilevel wells ML1 and ML2 is predominantly horizontal. There is a small vertical flow component in ML1 and possibly ML2. There was general disagreement between the diver data and manual measurements for well ML1 regarding the extent of the drop in hydraulic head between the top two filters and Filter C. Given that the manual measurements show a similar difference between Filter C and the top two filters, it is more likely that there was an error in the diver measurement. The length of the string was longer than the string of the top two filter strings which increases the potential error in measurement. Manual groundwater measurements for well ML2 found that there was also a slight drop in Filter C, which indicates there is likely a small amount of vertical flow in this layer as well. The manual measurements show that between Filter B and C there is a drop of 3.4cm (ML1) and 4.7cm (ML2).

	Average		Coarse		Fine	
	Kmin	Kmax	Kmin	Kmax	Kmin	Kmax
Velocity (m/d)	0.010	0.015	0.025	0.038	0.0026	0.0039
Airport boundary (years)	76.0	50.7	30.4	20.3	294.7	196.4
ML1 to ML2 (years)	45.2	30.1	18.1	12.1	175.1	116.7

Table 5.1: Groundwater travel time in the saturated zone between the western runway and the airport boundary and between multilevel wells ML1 and ML2 based on a hydraulic conductivity measured by the Hazen equation for the average, coarse- and fine-grained sediment samples at the study site.

5.1.3 Flow and dispersion in deeper layers

The flow between the runway and the ravines is largely characterized by horizontal flow pathways. Temperature data indicates that there is more connectivity in Filters A and B compared to Filter C for both ML1 and ML2. The general trend of warming of the top two filters during the colder months is counter-intuitive but is likely due to the rain in November which was approximately 12°C. The longer time it takes for temperature to plateau compared to hydraulic head is likely due to the slower rate of temperature diffusion compared to the rate of infiltration, which affects the hydraulic head. The delayed plateau of Filter B compared to Filter A in both wells is likely an effect of the insulation in deeper layers and thus a longer time for temperature to diffuse.

Temperature data from the divers show that there may be some flow separation between the middle filters at 12-13 meters below the surface and the bottom filters at 24-25 meters. Filter C in well ML1 remains at a lower temperature and does not show the temperature trends that occur in the top filters. Filter C in well ML2 shows less of the seasonal variation in temperature that is visible in the top two filters. However, its temperature is much closer to the top filters, which may indicate that it is more hydraulically connected. The difference in temperature between ML1 Filter C and the top two filters indicates that there is greater stratification and horizontal flow patterns in the top 12 meters between these two wells.

5.1.4 Mineral dissolution

This study found significant difference in the water chemistry between the well closest to the runway, ML1, and the well ML2, which approximately 167 meters further downgradient. The change in chemical composition between the two wells is particularly evident in the increase in major ions such as HCO_3^-, K^+, and Na^+ in well ML1 compared to ML2 in Filters A and B (Figure 4.14). The chemical composition in ML2 is less directly affected by seasonal input of deicing chemicals.

Both ML1 and ML2 have the highest concentrations of ions in Filter B (12-13m). Previous studies in the Gardermoen Aquifer have found an increase in major ions concentrations with depth [Skarstad, 1996, Basberg et al., 1998]. An increase in major ion concentrations is generally described in terms of natural mineral dissolution processes of calcite, pyrite and silica. The low ion concentration of the third filter in both ML1 and ML2 indicates that there is primarily horizontal flow and the possibility of a geochemical divide between filter B and C in both wells. The following mineral dissolution sections will focus primarily on groundwater chemistry data from well ML2 given that the filters are less affected by chemical deicers.

Calcite dissolution Both sets of groundwater samples from ML2 shows that the water chemistry for all three filters is a calcium bicarbonate type, which is accordance with previous studies [Dagestad, 1999, Jørgensen et al., 1990, Sundal, 2006]. A general trend evident in both wells is that the maximum concentration of calcium and bicarbonate is in Filter B, located between 12-13 meters below the surface. Based on the XRD analysis, the calcite front ranges are 8.6-12.5m (ML2) and 7.1-12.5m (ML1). ML1 and ML2 Filter B shows significantly higher calcium and bicarbonate levels compared to Filter A. Filter B in both wells is therefore likely below the calcite dissolution front and their high values are due to the degree of dissolved calcite ions. Dagestad [1999] similarly found a high increase in ions at approximately 12 meters depth.

Another way to analyze the role of calcite dissolution on the water chemistry is by finding the relationship between between HCO_3^- and Ca^{2+}. In Figure 5.2, a linear relationship is found between HCO_3^- and Ca^{2+}. Previous studies in the Gardermoen Aquifer have found a linear relationship between depth and calcite concentrations (Jørgensen et al. [1990]). A positive relationship with respect to depth was found between Filter A and Filter B. A positive
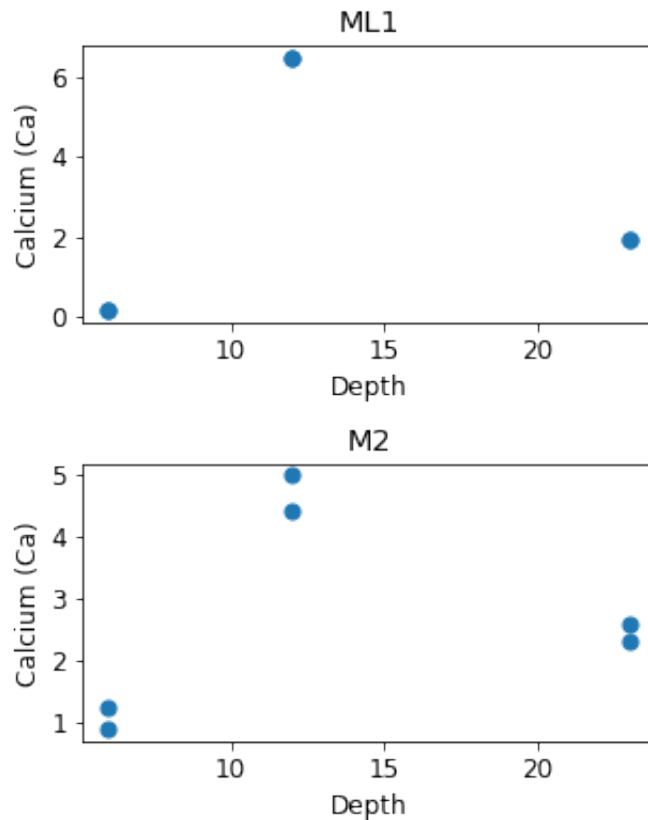
Figure 5.1: Relationship between calcium and depth for wells ML1 (top) and ML2 (bottom).

Figure 5.2: HCO_3^- with respect to calcium for well ML2. The two sampling periods are included and shown with respect to depth.

linear relationship indicates that calcite dissolution has occurred and and filtrating water may have reached equilibrium. Filter C in both Ml1 and ML2 does not indicate a positive linear relationship with the other filters with respect to depth. The lack of this relationship for the bottom filter could indicate a lack of geochemical connectivity with Filter C.

Silicate dissolution Many of the major ions are associated with silicate dissolution. These ions include Na^+, Ca^{2+}, K^+ and Mg^{2+}. In addition to calcium dissolution, an increase in magnesium may be due to dissolution of biotite ($K(Mg,Fe)_3(AlSI_3O_{10})(OH)_2$). Magnesium

follows the general trend of having the highest concentration in the top two filters of ML1 and ML2. However, in the bottom filter the concentrations are than in the middle filter. Sodium and potassium are also are products of silica dissolution. The dissolution of plagioclase, such as anorthite ($CaAl_2Si_2O_8$), will cause an increase in Na^+. For ML2, which is less affected by chemical deicers, the concentrations of Na^+ are slightly higher than the top filter but below the concentration of Filter B. Potassium, which is dissolved during dissolution of muscovite ($KAl_3Si_3O_{10}(OH)_2$ and biotite ($K(Mg,Fe)_3(AlSI_3O_{10})(OH)_2$), also increases from ML2 Filter A to B and then decreases to a concentration below or near Filter A.

Sulphate and pyrite oxidation Pyrite was found in the SEM analysis. Sulphate concentration does not show a clear increasing trend with respect to depth, as has been found in previous studies Skarstad [1996], Basberg et al. [1998]. In ML2, sulphate remains relatively constant between filter A and B with a concentration of 4.8 and 5.3 mg/L in August and 18 to 17 mg/L in November. It is unclear if the significant increase in sulphate between August and November that is observed in both trends has a seasonality component or is a factor of sampling method.

Sulphate is generally assumed to increase with depth given the oxidation of pyrite from 4 meters below the groundwater table [Skarstad, 1996] (Equation 2.5). It is assumed that in the unsaturated zone and in top layer of aquifer there is enough oxygen to have already oxidized all the pyrite. Additional sources of sulfur include rainwater with sulfur from marine aerosols. At the airport an additional source comes from sulphate aerosols from airplane traffic. Aerosols from these sources could thus be increasing the sulphate at the higher levels. The higher sulphate levels in ML1 compared to ML2 in Filter A when comparing within a sampling campaign supports this potential hypothesis.

5.1.5 Updated conceptual flow model

Chemical and temperature data indicate that there is a possible geochemical divide between Filter C and the top two filters. The conceptual model shown in Figure 5.3 updates a the sedimentary profiles shown in Figure 4.19. In this conceptual model the silt layer between 183 and 185 m.a.s.l in ML1 is connected with the silt layer found in BR29-2. However, lenses further downgradient are not connected, which would create more dispersion with deeper depths. The low flow unit is not an impermeable layer given that there is temporal synchronization in hydraulic head data.

The previous report by Hansen et al. [2020b] addressed the concern that vertical groundwater flow could lead to deeper layer flow and potential spread of deicing chemicals. Figure 5.3 indicates that if deicing chemicals enter the groundwater west of the runway, it is more probable that they will flow mostly horizontally and are not spread by large vertical gradients.
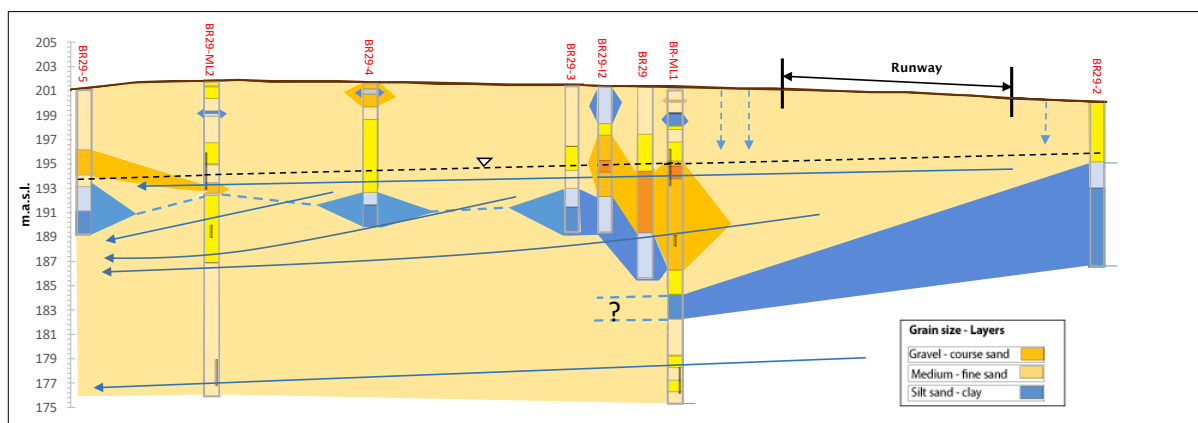
Figure 5.3: Schematic of all boreholes and possible groundwater paths, including previous well logs conducted by Avinor. Dark blue lines with arrows indicate possible groundwater pathways. Light blue dashed lines with arrows show infiltration of water and deicers near runway. Black dashed line shows the highest groundwater level recorded between November-May when divers were used to record depth. The question mark indicates indicates uncertainty regarding how far this low permeability layer spreads to the west. This study analyzed wells BR29-ML1 and BR29-ML2, which include three filters each.

5.2 Meteorology and chemical deicer infiltration for season 2020-2022

The meteorological trends in the season plays a large role in understanding chemical deicer usage patterns. Both seasons 2020-2021 and 2021-2022 were warmer than usual and also had on average less deicer usage Figure 4.17. However, the reduction in deicing chemicals may also be due a sharp reduction in passengers over these two seasons [Grotthing, 2022].

The season 2020-2021 was generally warmer than usual, especially during the winter months. In the winter season, the lack of sustained sub-zero temperatures through December indicates that the ground may not have fully frozen until January Figure 4.13. Application of propylene glycol started in September and potassium formate in October 2020. The fluctuating temperature patterns in December likely caused a melting of snow and infiltration of water and deicing chemicals prior to January. This is also supported by the fact that a low concentration of propylene glycol (0.44 mg/L) was detected on January 15th in a well approximately 34 meters downgradient from the runway (BR29-2). The precipitation that fell as rain in December helped to flush deicers into the unsaturated zone. December was the second highest month of propylene glycol usage after January in the 2020-2021, indicating how oscillating temperatures around zero can induce higher levels of deicer usage.

Snow cover in the 2020-2021 season appears fairly constant prior to a rain event in late February. The snowcover appears to almost be entirely reduced in the two weeks between late February to the beginning of March. This is likely when the bulk of deicers entered the system. Previous studies have estimated a retention time of approximately 20 days in the unsaturated zone near the western runway during the snow melt season [Wejden and Øvstedal, 2006]. Given preferential flow pathways and the lower freezing point of deicing chemicals, propylene glycol and formate may have begun infiltrating into the soil from early March. Given the rapid reduction of snowcover in late February, it is feasible that the deicing chemicals entered as a pulse injection.

The winter season of 2021-2022 was generally low precipitation between mid November and February. Snow cover was reported to be low at Gardermoen and therefore may be overestimated by the Ukkestad weather station used in this study [Grotthing, 2022]. The

warmer temperatures between mid January through mid February compared to the previous season indicate several different possible times of deicer melting, making it less likely there was a large pulse input of deicing chemicals due to rapid spring melt.

5.3 Iron and manganese reduction in 2021

The high dissolved iron concentrations 11m downgradient of the runway may be due to the infiltration of chemical deicers in the late fall (Figure 4.20). The high iron concentrations 44m downgradient of the runway between April and June indicate the reducing conditions during this time. The detection of methane 34m downgradient in April and June indicates that closer to the runway the groundwater is highly reducing. The spike 44m downgradient indicates that this is the location of the iron and manganese reduction zone. The drop in iron concentration seen between January and April at 11m and 34m downgradient from the runway may be due to a reduction in the amount of chemical deicers infiltrating as the ground freezes or due to a general reduction in the availability of iron electron acceptors. Manganese has low concentration in the wells 11m and 34m downgradient throughout the year, indicating less availability of manganese oxides along this flow path.

The peak of manganese and iron oxides in late summer is likely related to the pulse of deicing chemicals following snowmelt in late February 2021. The effect of the seasonal chemical loading indicates that there is an extended period of manganese and iron reduction during the spring and summer months. Dissolved iron and manganese concentrations are generally at low levels 100 meters downgradient from the runway.

5.3.1 Redox environment in study wells

The sampling of water chemistry in wells ML1 and ML2 provides information on redox conditions during late summer when there is less chemical loading from deicers. The water sampling in November occurred after chemical deicers had begun. PHREEQC speciation models provide insight into the potential for dissolution and precipitation of iron and manganese minerals given the water chemistry.

The PHREEQC speciation model indicates that the pE in August for the top filter is at approximately 7 for both wells based on the NO_3^-/NH_4^+ redox pair. In this environment it indicates that iron is most likely to speciate as geothetite but there is also a chance of ferrihydrite precipitation. The saturation index for ferrihydrite is between 1 and -1 for all the filters in ML1 and ML2. The SI index for for ferrihydrite is positive for the top two filters in ML1. However, the redox environment for the bottom filters in August was difficult to estimate provided that nitrate was not detected in either well and default value of 4 was estimated.

The availability of nitrate in the top filter in November indicates that it is in a suboxic state. However it was difficult to fully determine the redox state as the ammonium concentration was not measured. The high concentration jump in iron in ML1 Filter B from August to November indicates the effect of iron reduction in this layer.

The effect of deicing chemicals on the water chemistry can also be analyzed by the relationship between alkalinity relative to calcium. Figure 5.4 shows that there is not a clear linear relationship for well ML1 given that Filter A shows higher bicarbonate concentration. This indicates that calcite dissolution is not a useful indicator of the high amount of bicarbonate. Studies have shown that the reduction of Fe(III) and degradation of organic matter causes an increase in alkalinity (Equation 5.1) [Howell, 1998, Curtis, 1987].

$$(1/4)\,CH_2O + Fe(OH)_3\,(s) \longrightarrow Fe^{2+} + (1/4)\,HCO_3^- + (3/4)\,H_2O + (7/4)\,OH^- \qquad (5.1)$$
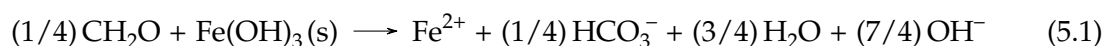
The manganese level shows an unexpected increase in Filter B (12-13m) between ML1 and ML2. This may be due to in part to the reduction in alkalinity between ML1 and ML2.
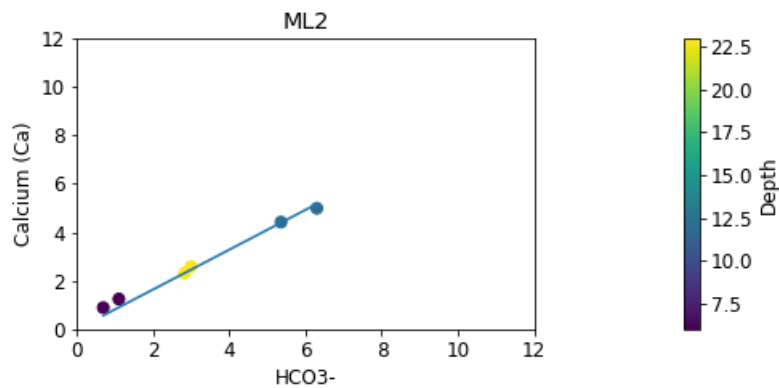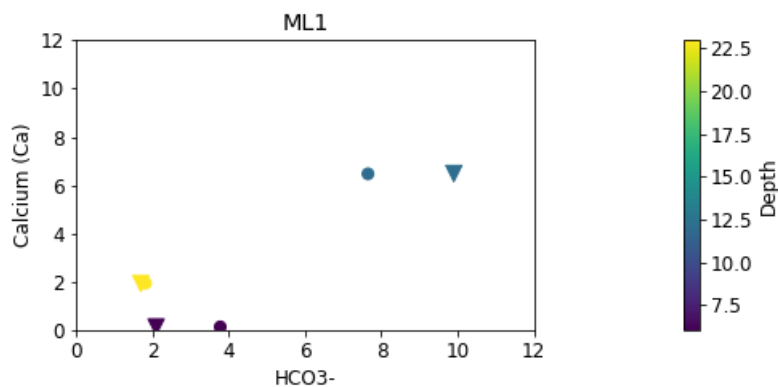
Figure 5.4: HCO_3^- with respect to calcium for well ML1. The two sampling periods are included and shown with respect to depth.

Previous column studies have shown that an increase in bicarbonate leads to precipitation of rhodochrosite $MnCO_3$ and a reduction in Mn^{2+}. Thus, the lower alkalinity ML2 may lead to a higher level of Mn_2^+. The PHREEQC speciation models shows a slight increase of the saturation index of $MnCO_3$ in ML1 Filter A compared to Filter 2.

The overall redox situation in these environments indicates an intermediary redox situation and a possibility for ferrihydrite precipitation, particularly in the top filters in August. The November campaign indicates that there may already be infiltration of some deicers given a large increase in iron levels Filter B. However, iron levels are also affected by rates of microbial degradation and thus temperature or changes to other conditions could also be impacting these levels.

5.4 Availability of manganese and iron electron acceptors

5.4.1 Total iron and manganese in sediment

The availability of electron acceptors is based on both dissolution of crystalline and amorphous minerals. The total iron in the sediment remained relatively constant with an average of 2.5% for iron and 0.039% for manganese. This supports previous studies that have found that manganese makes up a much smaller fraction in the sediment compared to iron at Gardermoen French [2005]. Figure 5.5 shows the majority of the iron is likely crystalline iron. Areas where XRD values indicate a higher wt. % of iron are over-estimations. This is due to the fact that the wt. % of iron in XRD is based on mineral stoichiometery, and thus does not include mineral impurities or minerals that make up less than 2 % by weight of the sediment. The difference between wt. % of iron determined by XRF and XRD is the amorphous iron, such as ferrihydride and iron sulphide (FeS).

The XRD data corresponds well with previous data that indicates that main iron containing minerals include chlorite, hornblende, muscovite and ankerite. XRD indicates that the predominant mineral contributing to iron is chlorite. However, based on dissolution rates, the rates of iron crystalline mineral dissolution is relatively slow compared to dissolution rates of amorphous iron and manganese oxides.
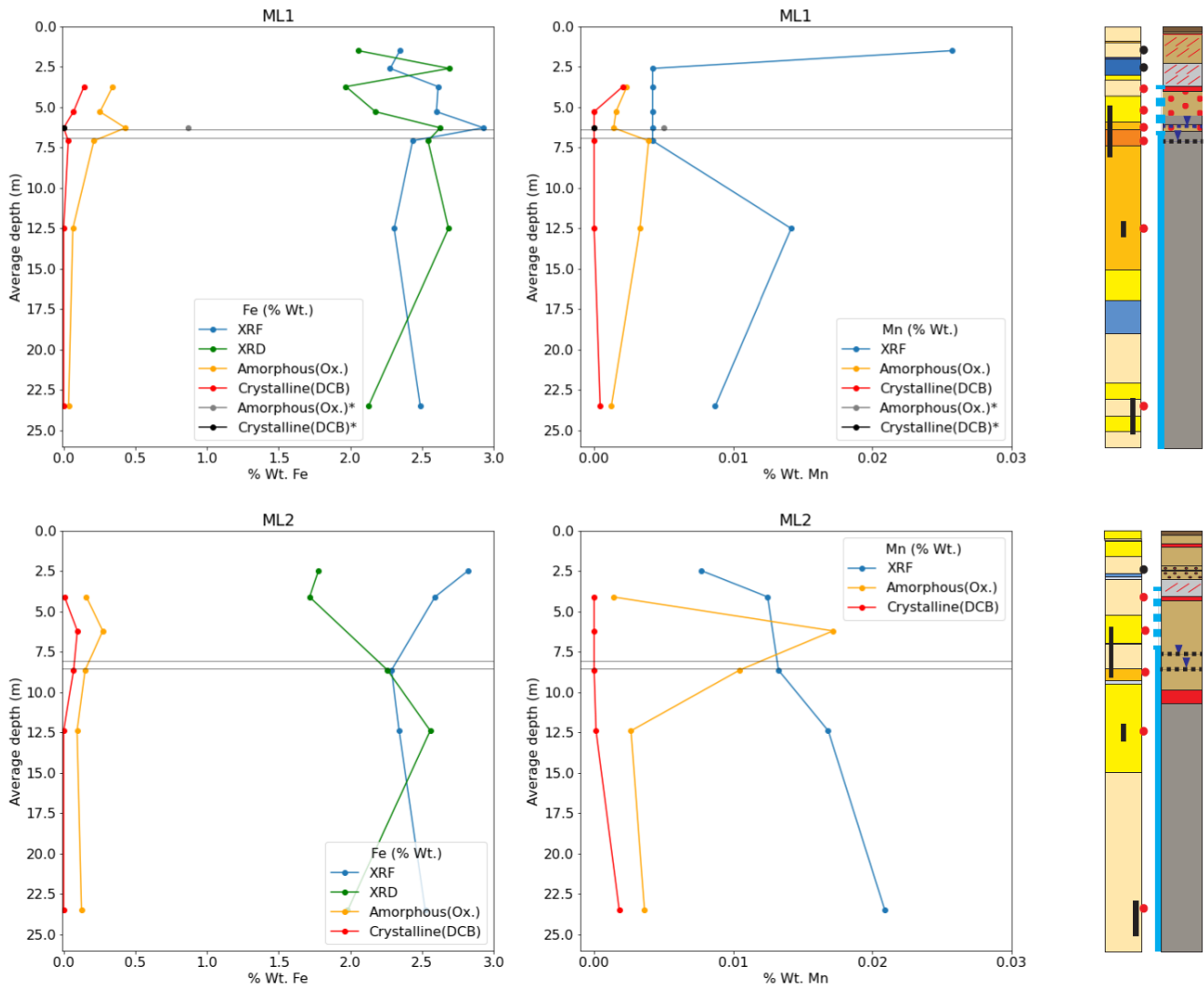
Figure 5.5: Results of extraction experiment for samples from wells BR-ML1 and BR-ML2 for manganese and iron. XRF values show the corrected values based on trendline in Figures 1 and 2. The top right figure includes results from a ground sample (Amorphous(Ox)* and Crystalline(DCB)*). The min and max groundwater depth from the uppermost filter for each respective well is shown as black lines.

5.4.2   Total iron and manganese oxides

Trends in total amount of amorphous iron and manganese oxides are important to understanding the availability of these electron acceptors and the redox environment. The iron extraction experiments allow for further understanding of the processes of precipitation and dissolution that is occurring in both the saturated and unsaturated zones.

Validity of DCB and oxalate results

Iron and manganese extracted from the DCB method was very close to the concentration of iron and manganese extracted using the oxalate method. Several samples from the oxalate experiment had higher concentrations of iron and manganese compared to the DCB experiment.It is not surprising that the oxalate and DCB concentrations are close for manganese oxide, given that manganese oxides minerals are primarily amorphous. The closeness in values

for iron extraction is more problematic for determining the concentrations of amorphous and crystalline oxide. Generally, it is assumed that the oxalate experiment will result in a far smaller percentage of amorphous iron oxides compared to the total amount of iron oxides extracted from the DCB experiment.

Two previous studies also conducted extraction studies for crystalline and amorphous iron and manganese oxides in the Gardermoen Aquifer [Søvik and Aagaard, 2003, Skarstad, 1996]. These studies were only conducted on soil samples 0 - 7.75 meters below the surface. Skarstad [1996] found total iron oxide levels of between 0.53-1.33 wt. %. The results for the oxalate and DCB extraction experiment from the present study fit in between the oxalate and DCB extraction experiments by Søvik and Aagaard [2003] and Skarstad [1996] for ML1. For ML2, the amorphous values fit more closely with oxalate values found by Søvik and Aagaard [2003].

Secondary iron oxide precipitate can be both amorphous and crystalline. There is reason for both the amorphous and crystalline fractions to decrease with depth in the saturated zone. However, the DCB iron oxide content decreases to almost zero in the lower depths. This low concentration is more intuitive for amorphous iron oxides, which form as secondary precipitate, compared to total iron oxide, which is not limited to secondary precipitation. The SEM analysis found that for ML1 there was areas of iron oxide present at 12.5 meters depth. No iron oxide was seen at this depth for ML2 but it was not possible to view much of the grains from this sample given the iron-rich clay coating.

The data collected from DCB experiment likely did not extract all of the iron oxide present in the samples. Previous studies have also shown cases where the DCB extraction did not go to completion and only extracted approximately 30% of the total iron oxide content [Reyes and Torrent, 1997]. The duration of the experiment could play a role in total extraction. Additional experiments which used more than one total iron oxide extraction approaches would also be useful for comparing results, as has been in other studies. A similar methodology was conducted by Ourradi [2021] and it is not clear if there was anything in the methodology or due to differences in the sediment sample that caused relatively low DCB concentrations.
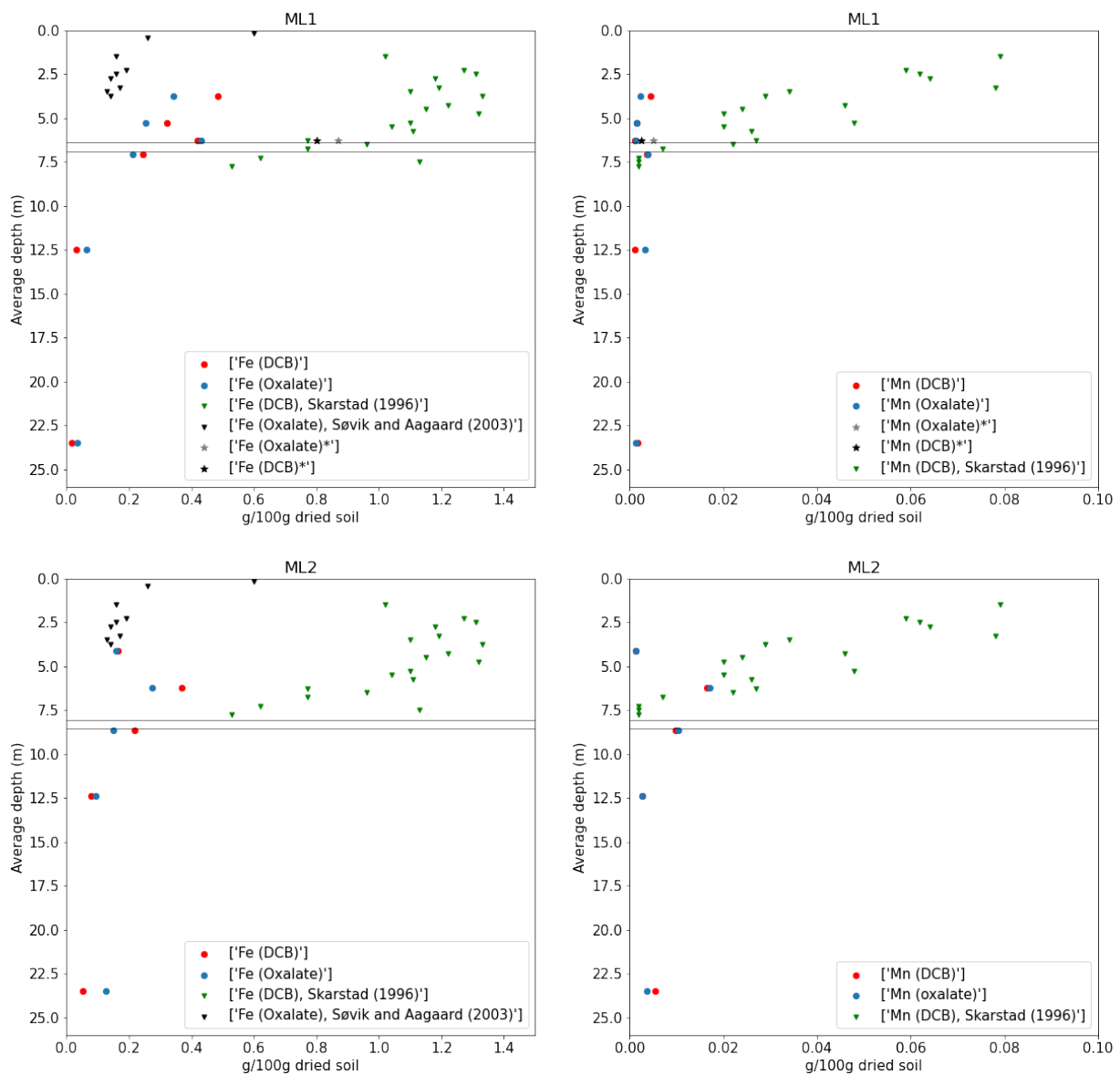
Figure 5.6: Iron and manganese extraction experiments from this research study compared with data from two previous oxalate and DCB experiments in the Gardermoen Aquifer. Skarstad [1996] conducted total iron and manganese extraction experiments and Søvik and Aagaard [2003] conducted iron oxalate experiments at Gardermoen.

Dissolution and precipitation of amorphous iron oxides

The general trend in oxalate-extracted iron shows that the highest wt.% in ML1 and ML2 is in the unsaturated zone or near the water table. Although only a small number of samples were taken in the unsaturated zone, there does not appear to be a large difference in oxlate-extracted

iron in the unsaturated zone. Amorphous iron is typically most apparent in the unsaturated zone. This zone has the most oxygen and rainwater usually is more acidic and slowly dissolves iron bearing minerals and releases iron that may then precipitate as iron oxides, creating a secondary coating [Grover, 2010]. This finding supports previous discussion on how the variable redox enivornment near the runway may support conditions for ferrihydrite percipitation.

The highest concentration of oxalate-extracted iron in ML1 at a depth of 6.15-6.4m coincides with the maximum amount of organic matter detected (0.16%). There are several potential reasons for why there is a correlation between the increase in organic matter and oxalate-extracted iron. The first possibility is that the extracted iron oxide is not amorphous but bound to organic material. The oxlate experiment extracts both amorphous and organic bound iron and manganese oxides. Another explanation is that the increase in TOC is due to propylene glycol in sediment. Previous studies have found that despite very the very low Kd value of propylene glycol, it can still create a thin coating on sediment grains which is not easily detectable French [2005]. Potential dissolution and precipitation of iron given TOC reduction could increase amorphous iron content.

Previous studies have also found an increase in iron precipitate at the capillary fringe due to groundwater transport of iron and diffusive oxygen transport in the unsaturated zone [Grover, 2010]. Studies show that this can produce an iron band formation in the unsaturated zone close to the water table [Grover, 2010]. This could also explain the slightly higher oxlate-extracted iron in ML1 along the water table. This is seen visually by the redox coloration profile for ML1 in Figure 5.5. In the unsaturated zone there is a graying of sediment and then a small zone with iron precipitates forming near the top of the highest recorded water table level. Similarly, a red band near the water table is also observed in JordB in Figure 4.1. Both of these wells are nearer to the runway and likely experience the most iron dissolution in the unsaturated zone compared to wells ML2 and JordC.

Results from SEM analysis indicate that iron is precipitated in both the unsaturated zone and at the sample point at the top of the water table at approximately 6.3m in ML1 (Figure 4.5). All the iron precipitate seen ML1 in SEM had crystallized. The clear crystalline shape of the secondary coatings are similar to previous studies of goethite under SEM [Hubbard et al., 2011]. This indicates that the secondary iron that precipitated on the grain surfaces viewed under SEM were most likely deposited as ferrihydrite and transformed into goethite. This transformation is often observed in aquifer systems given that ferrihydrite is less stable than goethite Lovley and Phillips [1986], Cornell et al. [2003]. Small amounts of Fe_2^+ can catalyze the recrystallization of ferrihydrite to either goethite or lepidocrite Larsen et al. [2006]. The only place where amorphous iron was likely spotted under SEM was in the unsaturated zone of ML2(Figure 4.5). There was one location where the transformation from ferrihydrite to goethite may be visible from a sample point near the water table in ML2. Thus, it indicates that there is iron precipitation occurring but does not visually show the availability of amorphous iron oxide.

Despite continued loading of ML1 the samples do not indicate that there was less amorphous iron in ML1 compared to ML2 in the unsaturated zone. The concentration of amorphous iron is approximately 0.3g/100g in the unsaturated zone at ML1 and 0.2g/100g at ML2. Visually, oxidation of iron is seen to occur further down in ML2 compared to ML1. This indicates that there may be more available oxygen at deeper levels in ML2 compared to ML1.

Dissolution and precipitation of amorphous manganese oxides

Despite the small number of sampling points there is some indication of a difference in the concentration in amorphous manganese oxide between well ML1 and ML2. The amount of manganese oxide extracted in the oxalate experiments is much lower compared to iron for both

ML1 and ML2. There was an average of 0.0097wt % for ML2 and 0.0023wt. % for ML1. The trend in manganese oxides with depth matches nicely with the study conducted by Skarstad [1996] for ML2 (Figure 5.6). However, the lower manganese concentration in the unsaturated zone of ML1 does not fit the trend seen in ML2 and in the study by Skarstad [1996]. This decrease in manganese could indicate the reduction of manganese oxide electron acceptors in the unsaturated zone nearer to the runway.

There are a few reasons why this trend is may be apparent with amorphous manganese oxide and not with amorphous iron oxide. Manganese precipitation is much slower compared to iron with oxygen. Studies show that that at a neutral pH precipitation of manganese oxide is slower by 100,000 compared to iron oxide Martin [2005]. The rate only becomes higher at a pH greater than 8, which is higher than rainwater pH and groundwater pH levels observed at Gardermoen Martin [2005]. Manganese oxides also dissolve faster than iron oxides Martin [2005]. Rates of manganese oxide dissolution have been found to be comparable to carbonate dissolution Martin [2005]. Thus, the slower rate of manganese oxide precipitation and faster dissolution indicates it may not be able to precipitate at a rate fast enough when redox conditions are more favorable along the western runway.

5.5   Sustainability of iron and manganese electron acceptors

A PHREEQC model was used to estimate the amount of iron oxide that is depleted when a pulse event occurs during the snow melt season. This model used concentrations of acetate, formate and propylene glycol that have been previously measured in well BR29 at two different sampling times. The model found that adding these chemical deicers created a large pulse of dissolved iron that entered the system. This model was mainly used to show the effect on iron reduction as the model showed a negligible effect on manganese oxide. These results can be used to estimate how long it would take to dissolve all amorphous iron by converting the reduction in ferrihydrite from mg/L to g/100g dry sediment. The total iron in the unsaturated zone in borehole ML1 is approximated by taking the average of the wt. % of iron determined by XRF between a depth of 0-6.3m, which is 2.53 wt .%. The available amorphous iron in the unsaturated zone is approximated by the average wt. % of oxalate-extracted iron in ML1 between 0-6.3m, which is 0.309g/100g dry sediment.

If it is assumed this pulse input approximates the concentration of chemical deicers that enters into the saturated zone over the coarse of the year, than this reduction can be seen as a yearly rate. The amount of iron oxide modeled by PHREEQC for the two different chemical deicers concentrations, -4.83 mol/L (C1) and -1.00 mol/L (C2), was then converted to the concentration of iron (mg/L) that is reduced. This value is $8.65 * 10^{-1}$mg/L (C1) and $1.76 * 10^{-1}$mg/L (C2), respectively. To calculate the amount of $Fe_{dissolved}$ in $\frac{g}{100g_{DrySediment}}$, a porosity (n) of 0.36 and density (ρ) of 2.65g/cm^3 was used. The following equation was used for the conversion:

$$\frac{mg_{Fe_{dissolved}}}{L_{groundwater}} * \frac{1g_{Fe_{dissolved}}}{1000mg_{Fe_{dissolved}}} * \frac{n * L_{groundwater}}{(1-n) * L_{sedimentGrains}} * \frac{1L_{sedimentGrains}}{2.65Kg_{sedimentGrains}} * \frac{1Kg_{sedimentGrains}}{1000g_{sedimentGrains}}$$
$$(5.2)$$

The calculations show how a higher chemical deicer concentration has a much larger effect on reducing model shows how the the effect of a higher concentration of deicers leads to a significantly higher increase in the rate of reduction of amorphous and total iron.

This model was built to primarily analyze the effect of iron oxide reduction in the aquifer. This is because in well BR29, which is closest to the runway, iron concentrations were found to be much higher than manganese concentrations during the period of snow melt (2020-2021). Thus, this model may over-estimate the amount of iron oxides that would need to be reduced

	Fe reduction	Fe (XRF)	Fe (Amorph)	Fe (XRF) depletion	Fe (Amorph) depletion
C1	-0.018 g/100g	2.53 g/100g	0.309 g/100g	137.8 years	16.8 years
C2	-0.0037 g/100g	2.53 g/100g	0.309 g/100g	$675.4 * 10^5$ years	$82.5 * 10^4$ years

Table 5.2: Depletion of total iron and amorphous iron based on pulse of chemical deicers formate and propylene glycol and acetate, a degradation product. C1 is the concentrations detected in BR29 on 04.04.2019 and C2 is the concentration detected on 12.02.2020. The first column, Fe reduction, is rate of iron reduced calculated from reduction of PHREEQC. Fe(XRF) is total iron in the unsaturated zone based on XRF values in ML1 in the unsaturated zone. Fe(amorph) is the average amorphous iron oxide in the unsaturated zone based on oxalate extraction experiments. Fe(XRF) depletion is the time it would take to deplete the total iron in the sediment and Fe(amorph) is the time it would take to deplete all the amorphous iron oxide.

given that manganese oxides are not being reduced. Additionally, this model does not take into account the re-precipitation of iron oxides in both the saturated and unsaturated zone close to the runway.

This model indicates that if the redox system was to be reducing in both the unsaturated zone and saturated zone throughout the year then the depletion of amorphous iron would quickly be unsustainable. This research study does not show that iron electron acceptors are currently being depleted near the western runway. However, an increase in the concentration of deicers may alter the seasonality of the redox conditions in the unsaturated and along the water table and reduce the ability for iron oxides to re-precipitate.

The oxalate extraction study showed that there is a reduction in amount of available manganese oxides closer to the runway (11m) compared to further away (167m). This may explain why the study by Hansen et al. [2020b] found there has been a 29% decrease in the median value of dissolved manganese (1.99 mg/L to 1.4 mg/L) between 1999 and 2019 along the western runway. A decrease in dissolved manganese may be due to a decrease in the overall amount that is available to be reduced. The low concentrations of manganese in the 44m downgradient of the runway was also found for the year 2021. A depletion in available manganese oxides would result in an increase in demand for other electron acceptors.

The overall increase in the median dissolved iron levels near the western runway from 0.01 mg/L to 4.7 mg/L between 1999 and 2019 indicates that there is an increase in the amount of iron oxides being reduced over this period of time. This increase could be due to both the increase in deicers over this period and also potentially to a decrease in the amount of amorphous manganese oxides available. Current use of $CaNO_3^-$ at Oslo Airport provides an additional source of electron acceptors that may help to buffer the possible effect of a reduction in amorphous manganese oxide electron acceptors.

5.6 Conclusions

Oslo Airport follows strict governmental regulations to not alter the groundwater chemistry of the Gardermoen Aquifer. Determining the sustainability of chemical deicer usage is particularly important given the increase in airport traffic over the past 20 years and corresponding increased use of deicing chemicals. The increase in dissolved manganese and iron observed in monitoring wells near the western runway indicates the role of iron and manganese as electron acceptors in the degradation of deicing chemicals.

An objective of this study was to analyze likely groundwater flow pathways along the western runway. The hydraulic head data indicates that there are no confining units. There is a significant decrease in ion concentrations in ML1 and ML2 between Filter B (12.5m) and Filter C (23.5m). The bottom Filter in ML1 is not affected by temperature changes evident in the

upper filters. A conceptual flow model indicates that the silt lens between 183 and 185 m.a.s.l in ML1 may extend upgradient to the groundwater divide. A low permeability layer would reduce the likelihood of vertical flow of chemical deicers.

A second objective of the report was to determine how chemical deicers affect iron and manganese reduction and precipitation processes. This study specifically analyzed manganese and iron concentrations in 2021. Generally, this study shows that there is a significant amount of dissolved iron and manganese in the well 44 meters downgradient of the runway due to redox processes. An increase in the concentration of dissolved manganese and iron at this well relates to infiltration of deicing chemicals. A PHREEQC reaction model shows that the pulse input of deicing chemicals will significantly reduce the redox potential and cause a reduction in iron oxide electron acceptors. PHREEQC speciation calculations show that in the August groundwater sample of well ML1 there was a redox potential of 7.2 and positive saturation index (SI) of ferrihydrite in the top two filters. SEM confirmed secondary iron oxide precipitate in the unsaturated zone and along the water table in boreholes ML1 and ML2. Thus there is likely a seasonal pattern to precipitation and reduction of iron oxide. Manganese iron oxide was found to have a negative SI index in the the late summer and early fall in both wells and for all filters. Manganese oxide was not found with SEM due to the much lower concentration of this mineral in the sediment.

A final objective was to determine if chemical deicer infiltration is sustainable in the long term given the availability of manganese and iron electron acceptors. Oxalate extraction and diathonite-citrate-bicarbonate (DCB) experiments were conducted to determine the amount of amorphous and crystalline iron oxides in the aquifer with respect to distance downgradient from the western runway. The results of the experiment show that the average amorphous iron oxide content in the unsaturated zone is approximately 2.5 g/100g dry sediment and there was not a significant difference with respect to distance downgradient from the runway. Total manganese oxide content was found to be 0.01 g/100g dry sediment in the unsaturated zone 157 meters downgradient from the runway (ML2) compared to 0.002 g/100g dry sediment for the well 11 meters downgradient from the runway (ML1). This indicates a possible depletion of manganese oxides which may cause higher amounts of iron oxide to dissolve over time. The ability of iron oxide to re-precipitate is essential to the sustainability of the seasonal use of deicers at Oslo airport. The PHREEQC reaction model indicates that if ferrihydrite is not able to re-precipitate in the unsaturated zone then amorphous iron oxide could be depleted in 16.8 years with elevated chemical deicer concentrations.

Appendix A

Additional Data
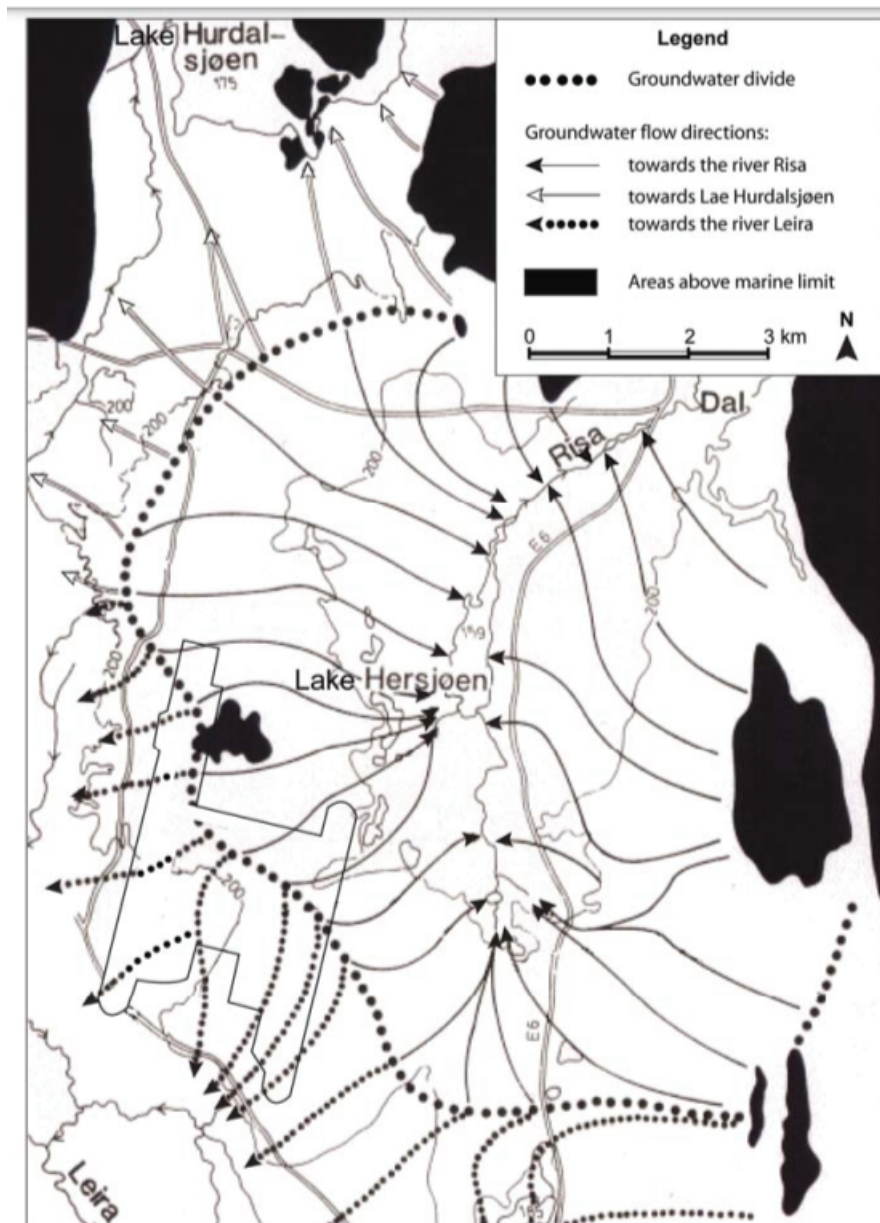
Figure A.1: Map of the groundwater flow pattern in the Gardermoen aquifer with the inclusion of an outline of Oslo Airport. Map is from Jørgensen and Østmo [1990] and modified by Sundal [2006].

Ion	units	Aug ML1 A	B	C	Aug ML2 A	B	C	Nov ML1 A	B	C	Nov ML2 A	B	C
Cromium (Cr)	mg/L	7.3E-4	2.5E-4	5.60E-4	6.8E-4	5.20E-4	2E-3	-	-	-	-	-	-
Calcium (Ca)	mg/L	3.1	130	39	18	100	52	3.18	129.8	39.33	25.12	88.61	46.39
Aluminum (Al)	mg/L	0.37	0.11	0.18	0.22	0.22	0.89	-	-	-	-	-	-
Ammonium (NH4)	mg/L	8.90E-2	6.3E-2	2.3E-2	6.5E-3	2.91E-2	2.3E-2	-	-	-	-	-	-
Lead (Pb)	mg/L	4.3E-3	5.4E-4	<0.00020	5.4E-4	4.8E-4	1E-3	-	-	-	-	-	-
Iron (Fe)	mg/L	1.8	4.60	0.21	0.41	1.6	0.96	1.97	17.20	0.82	0.235	3.20	0.51
Cadmium (Cd)	mg/L	2.2E-4	5.0E-6	5.0E-6	2.8E-5	<1.0E-5	<1.0E-5	-	-	-	-	-	-
Potassium (K)	mg/L	57	65	2.9	2.7	5.7	2.6	103.1	41.13	2.37	3.31	5.0	1.8
Copper (Cu)	mg/L	3.7E-3	5.9E-4	2.5E-4	6.4E-4	5.20E-4	1.5E-3	-	-	-	-	-	-
Mercury (Hg)	ug/L	<5.0E-3	<5.0E-3	<5.0E-3	<5.0E-3	<5.0E-3	<5.0E-3	-	-	-	-	-	-
Magnesium (Mg)	mg/L	0.38	11	3.2	1.6	12	5.6	0.11	11.46	3.64	2.21	9.11	5.29
Sodium (Na)	mg/L	33	25	4.10	1.9	5.8	4.10	41.13	25.07	4.59	1.71	7.39	4.18
Manganese (Mn)	mg/L	0.36	2.20	0.11	0.04	2.7	0.15	0.41	1.86	0.19	1.16E-2	2.91	0.14
Alkalinity	mmol/L	128.14	604.07	103.73	42.71	384.4	183.05	230.64	466.78	111.051	67.73	327.05	172.68
Arsenic (As)	mg/L	2.60E-2	0.01	1.10E-2	3.1E-4	5.3E-3	6.90E-3	-	-	-	-	-	-
Chloride (Cl)	mg/L	0.73	1.3	5.6	0.84	1.2	4	0.62	1.19	5.18	0.76	1.34	3.62
Fluoride (F)	mg/L	-	-	-	-	-	-	0.20	0	2.29E-2	1.276E-2	0	5.79E-3
Nitrate, Nitrite (NO3, NO2)	mg/L	2.7	2.5E-03	2.5E-03	2.30	2.5E-03	2.5E-03	0.63	0.71	0.25	3.82	0.28	0.00
Ammonium		0.09	0.06	0.02	0.01	0.03	0.02	-	-	-	-	-	-
Sulphate (SO4)	mg/L	12.16	3.97	8.98	4.84	5.31	3.67	21.43	55.74	25.80	17.64	16.75	12.47
Acetate	mg/L	<5.0E-1	<5.0E-2	<5.0E-3	<5.0E-4	<5.0E-5	<5.0E-6	-	-	-	-	-	-
Chemical oxygen demand	mg O2/L	1.4	1.6	0.77	0.79	1.4	0.96	-	-	-	-	-	-
Formate	mg/L	<5.0E-1	<5.0E-2	<5.0E-3	<5.0E-4	<5.0E-5	<5.0E-6	-	-	-	-	-	-
Dissolved organic carbon	mg/L	2.4	2	0.35	0.84	1.3	0.62	-	-	-	-	-	-
Propylenglykol	mg/L	<2.0E-1	<2.0E-1	<2.0E-1	<2.0E-1	<2.0E-1	<2.0E-1	-	-	-	-	-	-
Silica (Si)	mg/L	5.8	9.70	4.60	5.8	8.20	8.1	14.6	18.7	11.7	12.2	15.4	12.1
Total organic carbon	mg/L	2.30	2.30	0.15	0.76	1.3	0.69	-	-	-	-	-	-
pH	-	-	-	-	-	-	-	6.76	7.22	6.67	6.22	6.68	7.48
Electrical balance	%	13.22	1.8	10.14	17.22	0.78	3.81	4.89	7.37	1.48	1.93	0.8	-1.53

Table A.1: Water chemistry analysis multilevel wells ML1 and ML2, which include three filters (A,B,C). The first water sampling campaign was sampled by Avinor on August 12, 2021. The second campaign was on November, 23rd and they were analyzed at the University of Oslo.

Borehole	Sampling depth (range)	Depth (avg)	Grain size analysis	XRD	Field XRF	XRF (NTNU)	Extraction	SEM
ENGM-BR29-ML1	1.4-1.6	1.50	×	×	×			×
ENGM-BR29-ML1	2.5-2.7	2.60	×	×	×			
ENGM-BR29-ML1	3.6-3.85	3.73	×	×	×		×	×
ENGM-BR29-ML1	5.15-5.4	5.28	×	×	×		×	×
ENGM-BR29-ML1	6.15-6.4	6.28	×	×	×		x[1]	×
ENGM-BR29-ML1	6.95-7.2	7.08	×	×	×		×	×
ENGM-BR29-ML1	12-13	12.50	×	×	×		×	×
ENGM-BR29-ML1	14-15	14.50	×					
ENGM-BR29-ML1	20-21	20.50	×					
ENGM-BR29-ML1	23-24	23.50	×	×	×		×	
ENGM-BR29-JORDB	2.75-3	2.88	×	×	×			
ENGM-BR29-JORDB	4-4.25	4.13	×	×	×			
ENGM-BR29-JORDB	6.6-6.8	6.70	×	×	×			
ENGM-BR29-JORDB	8.2-8.4	8.30	×					
ENGM-BR29-JORDB	11.4-11.65	11.53	×	×	×			
ENGM-BR29-JORDC	2.25-2.55	2.40	×	×	×			
ENGM-BR29-JORDC	4-4.25	4.13	×	×	×			
ENGM-BR29-JORDC	7.1-7.2	7.15	×	×	×			
ENGM-BR29-ML2	2.4-2.55	2.48	×	×	×			×
ENGM-BR29-ML2	4-4.2	4.10	×	×	×		×	×
ENGM-BR29-ML2	6-6.4	6.20	×				×	
ENGM-BR29-ML2	8.5-8.75	8.63	×	×	×		×	×
ENGM-BR29-ML2	12.25-12.5	12.38	×	×	×		×	×
ENGM-BR29-ML2	16-17	16.50	×					
ENGM-BR29-ML2	20-21	20.50	×					
ENGM-BR29-ML2	23-24	23.50	×	×	×		×	

Table A.2: Overview of all sedimentary laboratory analysis conducted with respect to a sampling depth range, also given as an average depth.[1] [1] indicates sample that was additionally ground in the extraction experiment.

Borehole	Sampling depth (range)	Depth (avg)	D10 (mm)	D30 (mm)	D60 (mm)	Uniformity Coefficient	Coefficient of Curvature
ENGM-BR29-ML1	1.4-1.6	1.5	1.22E-02	5.27E-02	1.00E-01	8.18	2.26
	2.5-2.7	2.6	4.70E-03	1.90E-02	4.32E-02	9.20	1.78
	3.6-3.85	3.725	1.13E-02	1.30E-01	3.91E-01	34.42	3.79
	5.15-5.4	5.275	1.42E-02	1.54E-01	3.71E-01	26.21	4.50
	6.15-6.4	6.275	2.63E-02	3.33E-01	6.67E-01	25.35	6.31
	6.95-7.2	7.075	3.53E-02	4.07E-01	8.40E-01	23.81	5.59
	12-13	12.5	3.78E-01	6.49E-01	9.73E-01	2.57	1.14
	14-15	14.5	3.27E-02	9.68E-02	1.88E-01	5.75	1.53
	20-21	20.5	8.66E-02	1.66E-01	2.86E-01	3.30	1.12
	23-24	23.5	6.04E-02	2.11E-01	5.98E-01	9.89	1.23
ENGM-BR29-JORDB	2.75-3	2.875	2.20E-02	1.04E-01	1.81E-01	8.21	2.74
	4-4.25	4.125	2.28E-02	3.47E-01	7.54E-01	33.09	7.00
	6.6-6.8	6.7	2.10E-02	2.41E-01	4.26E-01	20.28	6.49
	8.2-8.4	8.3	5.59E-03	4.52E-02	1.60E-01	28.54	2.29
	11.4-11.65	11.525	6.31E-02	2.12E-01	3.54E-01	5.61	2.01
ENGM-BR29-JORDC	2.25-2.55	2.4	2.20E-02	1.04E-01	1.81E-01	8.21	2.74
	4-4.25	4.125	2.28E-02	3.47E-01	7.54E-01	33.09	7.00
	7.1-7.2	7.15	2.10E-02	2.41E-01	4.26E-01	20.28	6.49
ENGM-BR29-ML2	2.4-2.55	2.475	1.27E-02	4.94E-02	9.51E-02	7.48	2.02
	4-4.2	4.1	2.24E-02	1.07E-01	3.69E-01	16.46	1.38
	6-6.4	6.2	1.01E-02	1.47E-01	4.51E-01	44.85	4.74
	8.5-8.75	8.625	3.25E-02	3.17E-01	6.71E-01	20.65	4.60
	12.25-12.5	12.375	4.72E-02	2.57E-01	4.36E-01	9.23	3.21
	16-17	16.5	2.32E-02	6.89E-02	1.13E-01	4.87	1.82
	20-21	20.5	1.95E-02	8.55E-02	1.81E-01	9.28	2.06
	23-24	23.5	2.53E-02	7.60E-02	1.24E-01	4.91	1.83

Table A.3: The values of D10, D30 and D60 which were determined from the cumulative grain size distribution of each sample. From the values, the uniformity coefficient and the coefficient of curvature were determined. Samples are from boreholes ML1, ML2, JordC and JordD and they are listed with the full descriptive name (ENGM-BR29) before the borehole.

Well	Min	Max	Avg
ML1	1.4	1.6	1.5
	2.5	2.7	2.6
	3.6	3.85	3.725
	5.15	5.4	5.275
	6.15	6.4	6.275
	6.95	7.2	7.075
	12	13	12.5
	14	15	14.5
	20	21	20.5
	23	24	23.5
JORDB	2.75	3	2.875
	4	4.25	4.125
	6.6	6.8	6.7
	8.2	8.4	8.3
	11.4	11.65	11.525
JORDC	2.25	2.55	2.4
	4	4.25	4.125
	7.1	7.2	7.15
ML2	2.4	2.55	2.475
	4	4.2	4.1
	6	6.4	6.2
	8.5	8.75	8.625
	12.25	12.5	12.375
	16	17	16.5
	20	21	20.5
	23	24	23.5

Table A.4: Range of the sampling depths for sediment samples for boreholes ML1, JORDB, JORDC and ML2.

Well	Average Depth	Mn (Field XRF)	Fe (Field XRF)	Fe (NTNU XRF)	Mn (NTNU XRF)
ML1	1.5	9.73E-03	0.93	2.34	5.34E-02
	2.6	2.30E-03	0.90	2.28	1.58E-02
	3.7	2.30E-03	1.04	2.61	1.58E-02
	5.3	2.30E-03	1.04	2.60	1.58E-02
	6.3	2.30E-03	1.17	**2.92**	**2.81E-02**
	7.1	2.30E-03	0.97	**2.43**	**3.03E-02**
	12.5	9.97E-03	0.92	**2.35**	**5.26E-02**
	23.5	8.93E-03	0.99	2.49	4.93E-02
ML2	2.48	1.04E-02	1.13	2.82	5.67E-02
	4.1	3.36E-03	1.03	2.59	2.12E-02
	8.6	3.45E-03	0.91	**2.50**	**4.75E-02**
	12.5	8.50E-03	0.93	2.34	4.72E-02
	23.5	9.51E-03	1.00	2.52	5.23E-02
JordB	2.9	2.30E-03	0.78	1.98	1.58E-02
	4.1	6.32E-03	1.15	2.87	3.61E-02
	6.7	1.20E-02	1.09	2.73	6.49E-02
	11.5	6.80E-03	0.94	2.36	3.86E-02
JordC	2.4	7.40E-03	1.05	2.63	4.16E-02
	4.1	7.13E-03	0.80	2.04	4.02E-02
	7.2	9.82E-03	0.93	2.33	5.39E-02

Table A.5: Average of total iron and manganese in sediment samples (wt.%) determined with a field XRF based on three replicas. Additionally, total iron and manganese for the sediment samples were corrected based on concentrations determined by NTNU XRF analysis (wt.%) for four sediment samples. The values of the four sediments are in bold. The remaining values were calculated based on the correlation between NTNU XRF values and the difference between the NTNU XRF values and the field XRF values (calculated in wt%).

Piezometer	Elevation (m.a.s.l.)	TOC (m.a.s.l.)	TOC (m)	Diver Depth (m)	Borehole Length (m)	Coordinate (x)	Coordinate (y)
BR29-ML1A	200.922	200.563	0.359	7.569	9	6674384.789	615105.304
BR29-ML1B	200.922	200.543	0.379	11.057	15	6674384.798	615105.204
BR29-ML1C	200.922	200.592	0.33	17.625	26	6674384.727	615105.241
BR29-ML2A	201.722	201.428	0.294	8.776	10	6674299.617	614975.078
BR29-ML2B	201.722	201.462	0.26	11.285	15	6674299.51	614975.086
BR29-ML2C	201.722	201.522	0.2	17.704	26	6674299.566	614975.12

Table A.6: Raw data used to calculate the hydraulic head for each filter in wells ML1 and ML2. The elevation of each well in m.a.s.l, the top of casing (TOC), the diver depth (m), borehole length and coordinate information in EUREF89 UTM32.
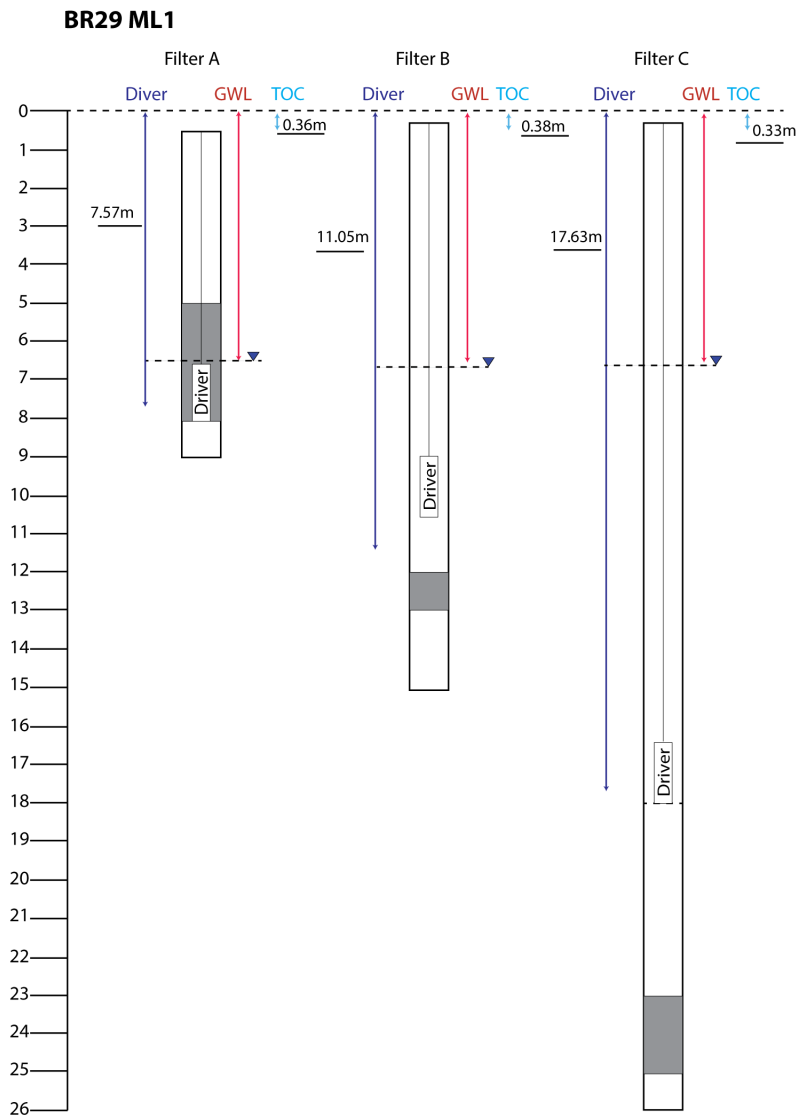
Figure A.2: Schematic used to calculate hydraulic head for well ML1 for Filter A, B and C. The depth of divers and top of casing (TOC) is shown, given varying levels groundwater (GW) depth.
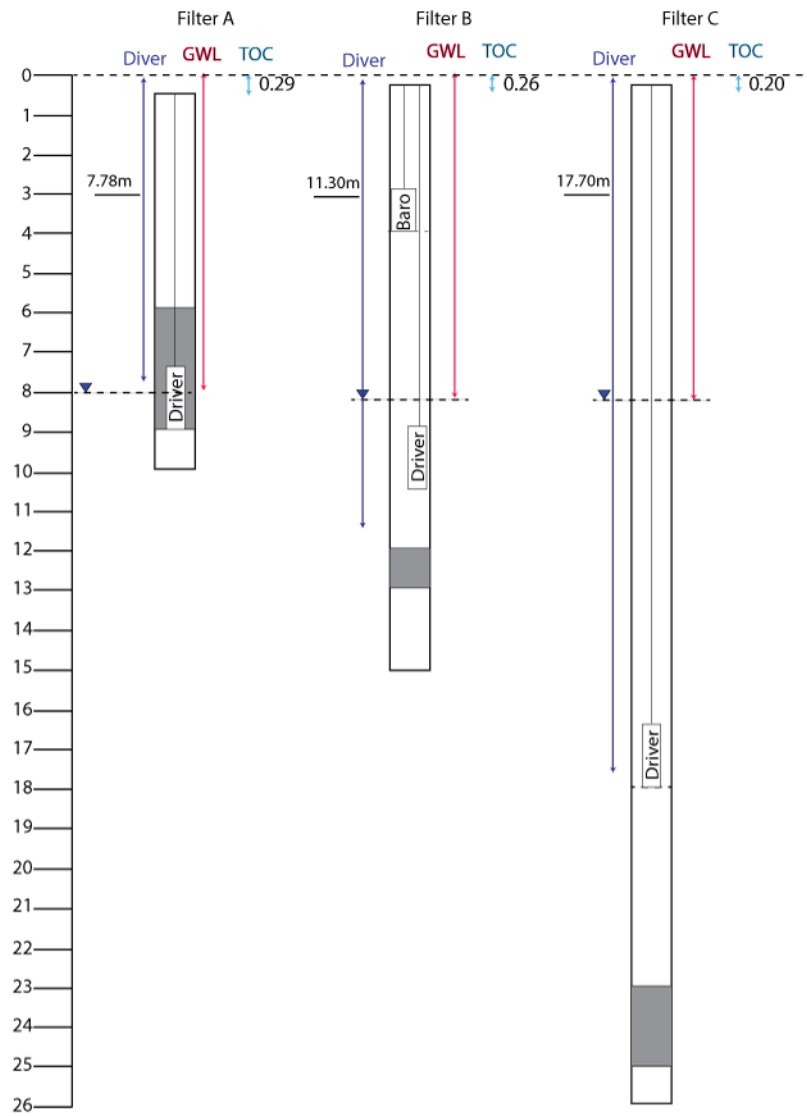
Figure A.3: Schematic used to calculate hydraulic head for well ML2 for Filter A, B and C. The depth of divers and top of casing (TOC) is shown, given varying levels groundwater (GW) depth.

Number	Description	pH	pe	temp	Alkalinity	Na	Mg	K	Ca	N(5)	S(6)	Cl	Mn	Fe	N(-3)	Si	Al
1	ML1_Aug_A	6.76	7.17	12.3	2.10E+00	1.44E+00	1.56E-02	1.46E+00	7.73E-02	0.043545	1.27E-01	2.06E-02	6.55E-03	3.22E-02	4.88E-03	2.07E-01	#no conv
2	ML1_Aug_B	7.22	4	10	9.90E+00	1.09E+00	4.53E-01	1.66E+00	3.24E+00	4.03E-05	4.13E-02	3.67E-02	4.01E-02	8.24E-02	3.49E-03	3.45E-01	4.08E-03
3	ML1_Aug_C	6.67	4	10.8	1.70E+00	1.78E-01	1.32E-01	7.42E-02	9.73E-01	4.03E-05	9.35E-02	1.58E-01	2.00E-03	3.76E-03	1.28E-03	1.64E-01	6.67E-03
4	ML1_Nov_A	6.76	7.09	12.3	3.78E+00	1.79E+00	4.42E-03	2.64E+00	7.93E-02	0.043545	2.23E-01	1.77E-02	7.55E-03	3.51E-02	4.88E-03	2.07E-01	#no conv
5	ML1_Nov_B	7.22	4	10	7.65E+00	1.09E+00	4.72E-01	1.05E+00	3.24E+00	4.03E-05	5.80E-01	3.35E-02	3.39E-02	3.08E-01	3.49E-03	3.45E-01	4.08E-03
6	ML1_Nov_C	6.67	4	10.8	1.82E+00	2.00E-01	1.50E-01	6.07E-02	9.81E-01	4.03E-05	2.68E-01	1.46E-01	3.54E-03	1.48E-02	1.28E-03	1.64E-01	6.67E-03
7	ML2_Aug_A	6.22	8.1	9.9	7.00E-01	8.26E-02	6.58E-02	6.91E-02	4.49E-01	0.037094	5.04E-02	2.37E-02	7.28E-04	7.34E-03	3.60E-04	0.206512	8.15E-03
8	ML2_Aug_B	6.68	4	9	6.30E+00	2.52E-01	4.94E-01	1.46E-01	2.50E+00	4.03E-05	5.53E-02	3.38E-02	4.92E-02	2.86E-02	1.61E-03	2.92E-01	#no conv
9	ML2_Aug_C	7.48	4	9.1	3.00E+00	1.78E-01	2.30E-01	6.65E-02	1.30E+00	4.03E-05	3.82E-02	1.13E-01	2.73E-03	1.72E-02	1.28E-03	2.88E-01	3.30E-02
10	ML2_Nov_A	6.22	8.11	9.9	1.11E+00	7.46E-02	9.08E-02	8.47E-02	6.27E-01	0.037094	1.84E-01	2.13E-02	2.12E-04	4.22E-03	3.60E-04	0.206512	8.15E-03
11	ML2_Nov_B	6.68	4	9	5.36E+00	3.21E-01	3.75E-01	1.28E-01	2.21E+00	4.03E-05	1.74E-01	3.77E-02	5.29E-02	5.71E-02	1.61E-03	2.92E-01	#no conv
12	ML2_Nov_C	7.48	4	9.1	2.83E+00	1.82E-01	2.18E-01	4.70E-02	1.16E+00	4.03E-05	1.30E-01	1.02E-01	2.55E-03	9.15E-03	1.28E-03	2.88E-01	3.30E-02

Table A.7: Input data for SOLUTION_SPREAD datablock in PHREEQC for speciation model.

Sample	Goethite	Pyrite	Pyrochroite	Quartz	Muscovite	Montmor-Ca	Montmor-Mg	Diopside	$CO_2(g)$	$O_2(g)$	Hedenbergite
ML1 Aug A	6.35E+00	-1.00E+03	-6.98E+00	6.17E-01	-1.00E+03	-1.00E+03	-1.00E+03	-1.14E+01	-1.72E+00	-3.12E+01	-1.19E+01
ML1 Aug B	6.24E+00	-1.00E+03	-5.42E+00	8.94E-01	1.08E+01	6.52E+00	6.47E+00	-6.40E+00	-1.56E+00	-4.28E+01	-6.49E+00
ML1 Aug C	3.93E+00	-1.00E+03	-7.68E+00	5.52E-01	7.44E+00	4.18E+00	4.13E+00	-1.00E+01	-1.74E+00	-4.48E+01	-1.04E+01
ML1 Nov A	6.38E+00	-1.00E+03	-6.95E+00	6.17E-01	-1.00E+03	-1.00E+03	-1.00E+03	-1.20E+01	-1.47E+00	-3.16E+01	-1.18E+01
ML1 Nov B	6.87E+00	-1.00E+03	-5.49E+00	8.94E-01	1.06E+01	6.53E+00	6.48E+00	-6.38E+00	-1.68E+00	-4.28E+01	-5.85E+00
ML1 Nov C	4.51E+00	-1.00E+03	-7.44E+00	5.52E-01	7.33E+00	4.19E+00	4.14E+00	-1.00E+01	-1.71E+00	-4.48E+01	-9.82E+00
ML2 Aug A	5.38E+00	-1.00E+03	-8.98E+00	6.74E-01	6.51E+00	3.60E+00	3.56E+00	-1.23E+01	-1.68E+00	-3.04E+01	-1.36E+01
ML2 Aug B	4.41E+00	-1.00E+03	-6.34E+00	8.46E-01	-1.00E+03	-1.00E+03	-1.00E+03	-8.79E+00	-1.21E+00	-4.53E+01	-9.09E+00
ML2 Aug C	5.99E+00	-1.00E+03	-5.97E+00	8.37E-01	1.01E+01	6.75E+00	6.71E+00	-6.12E+00	-2.33E+00	-4.21E+01	-6.96E+00
ML2 Nov A	5.13E+00	-1.00E+03	-9.54E+00	6.74E-01	6.55E+00	3.64E+00	3.59E+00	-1.20E+01	-1.48E+00	-3.04E+01	-1.37E+01
ML2 Nov B	4.76E+00	-1.00E+03	-6.30E+00	8.46E-01	-1.00E+03	-1.00E+03	-1.00E+03	-8.95E+00	-1.28E+00	-4.53E+01	-8.79E+00
ML2 Nov C	5.71E+00	-1.00E+03	-6.00E+00	8.37E-01	9.95E+00	6.74E+00	6.70E+00	-6.19E+00	-2.36E+00	-4.21E+01	-7.28E+00

Sample	Montmor-Na	$Fe(OH)_3$	Ankerite	Albite	Calcite	Clinochlore-14A	$(OH)_2(am)$	Anorthite	Pyrolusite	Maximum_Microcline
ML1 Aug A	-1.00E+03	1.06E+00	-1.57E+01	-1.00E+03	-2.20E+00	-1.00E+03	-7.85E+00	-1.00E+03	-7.31E+00	-1.00E+03
ML1 Aug B	6.05E+00	9.15E-01	-1.05E+01	1.54E+00	3.73E-01	-7.07E+00	-6.44E+00	-2.85E+00	-1.15E+01	5.02E+00
ML1 Aug C	3.53E+00	-1.38E+00	-1.41E+01	-9.19E-01	-1.31E+00	-1.58E+01	-8.64E+00	-5.25E+00	-1.47E+01	1.99E+00
ML1 Nov A	-1.00E+03	1.09E+00	-1.53E+01	-1.00E+03	-1.97E+00	-1.00E+03	-7.83E+00	-1.00E+03	-7.44E+00	-1.00E+03
ML1 Nov B	6.06E+00	1.55E+00	-1.03E+01	1.54E+00	2.51E-01	-7.00E+00	-6.51E+00	-2.84E+00	-1.16E+01	4.83E+00
ML1 Nov C	3.55E+00	-8.00E-01	-1.37E+01	-8.76E-01	-1.29E+00	-1.56E+01	-8.41E+00	-5.27E+00	-1.45E+01	1.89E+00
ML2 Aug A	2.90E+00	5.46E-02	-1.70E+01	-1.62E+00	-2.46E+00	-2.21E+01	-1.00E+01	-6.84E+00	-8.89E+00	1.60E+00
ML2 Aug B	-1.00E+03	-9.23E-01	-1.20E+01	-1.00E+03	-4.43E-01	-1.00E+03	-7.42E+00	-1.00E+03	-1.37E+01	-1.00E+03
ML2 Aug C	6.08E+00	6.52E-01	-1.20E+01	1.05E+00	-1.97E-01	-5.59E+00	-7.05E+00	-2.42E+00	-1.17E+01	3.94E+00
ML2 Nov A	2.89E+00	-1.89E-01	-1.66E+01	-1.69E+00	-2.14E+00	-2.16E+01	-1.06E+01	-6.74E+00	-9.43E+00	1.67E+00
ML2 Nov B	-1.00E+03	-5.74E-01	-1.21E+01	-1.00E+03	-5.57E-01	-1.00E+03	-7.38E+00	-1.00E+03	-1.36E+01	-1.00E+03
ML2 Nov C	6.08E+00	3.80E-01	-1.23E+01	1.06E+00	-2.70E-01	-5.70E+00	-7.08E+00	-2.46E+00	-1.17E+01	3.79E+00

Table A.8: Output results from PHREEQC speciation model for mineral saturation indexes.

	Delta change (mol)					Concentration (mol)	
	$CO_2(g)$	Calcite	$Fe(OH)_3$	$Mn(OH)_2$	Quartz	Fe^{2+} (mol)	Mn (mol)
C1	1.58E-02	7.16E-05	-1.00E-02	6.70E-06	-1.69E-06	1.01E-02	8.53E-07
C2	7.39E-02	7.80E-05	-4.83E-02	7.27E-06	-2.66E-06	4.84E-02	2.76E-07

Table A.9: Output of PHREEQC reaction model with addition of chemical deicers. The output results show the molar change in amount of minerals and $CO_2(g)$. For minerals, negative change indicates a dissolution and a positive value indicates precipitation. For $CO_2(g)$ a positive value indicates an increase in $CO_2(g)$ and a negative value decrease in $CO_2(g)$.

Borehole	Sampling depth (range)	Depth (avg)	Clay	Silt	Sand	Very fine	Fine	Medium	Coarse	Gravel	Dominant Size
ENGM-BR29-ML1	1.4-1.6	1.50	3.54	24.81	71.65	8.0155	59.7948	2.7096	1.1316	0	Fine sand
	2.5-2.7	2.60	5.61	61.91	32.49	9.91	22.54	0.04	0	0	Silt
	3.6-3.85	3.73	3.56	15.06	76.59	1.85	26.47	23.23	25.04	4.8	Fine sand
	5.15-5.4	5.28	3.22	13.3	83.28	1.76	24.66	35.24	21.62	0.21	Medium
	6.15-6.4	6.28	2.6	9.6	83.44	0.73	9.03	24.24	49.45	4.36	Coarse sand
	6.95-7.2	7.08	2.31	9.07	69.31	0.74	8.11	15.57	44.89	19.31	Coarse sand
	12-13	12.50	0.43	1.44	79.44	0.06	1.45	12.86	65.05	18.7	Coarse sand
	14-15	14.50	1.44	7.08	91.48	1.8472	24.0026	17.7135	47.9165	0	Coarse sand
	20-21	20.50	2.11	12.02	85.86	3.8	60.93	17.87	3.26	0	Fine sand
	23-24	23.50	1.25	4.56	94.2	1.1	48.09	34.84	10.16	0	Fine sand
ENGM-BR29-JORDB	2.75-3	2.88	2.48	12.6	84.41	2.54	69.53	11	1.34	0.52	Fine sand
	4-4.25	4.13	2.65	10.18	74.04	0.81	9.24	18.36	45.62	13.14	Coarse sand
	6.6-6.8	6.70	2.38	10.8	86.43	0.85	16.95	41.32	27.32	0.39	Medium sand
	8.2-8.4	8.30	4.74	26.7	68.57	3.21	50.15	13.17	2.04	0	Fine sand
	11.4-11.65	11.53	1.64	7.33	91.03	1.03	26.59	56.1	7.32	0	Medium sand
ENGM-BR29-JORDC	2.25-2.55	2.40	2.14	9.47	87.77	1.83	62.96	21.35	1.63	0.61	Fine sand
	4-4.25	4.13	4.19	16.41	50.14	1.17	11.56	12.14	25.27	29.25	Gravel
	7.1-7.2	7.15	3.96	17.71	66.53	1.3	15.54	21.34	28.35	11.81	Coarse sand
ENGM-BR29-ML2	2.4-2.55	2.48	3.13	27.24	69.62	8.43	61.09	0.1	0	0	Fine sand
	4-4.2	4.10	2.41	13.86	67.98	2.96	34.51	13.13	17.38	15.75	Fine sand
	6-6.4	6.20	3.58	15.29	65.94	1.75	20.43	23.58	20.18	15.19	Medium sand
	8.5-8.75	8.63	2.08	9.34	77.35	0.77	10.41	27.73	38.45	11.23	Coarse sand
	12.25-12.5	12.38	2	8.18	89.4	0.61	18.04	41.91	28.84	0.42	Medium sand
	16-17	16.50	2.96	15.83	81.21	7.11	73.42	0.68	0	0	Fine sand
	20-21	20.50	2.8	14.3	82.9	4	55.9	17.3	5.7	0	Fine sand
	23-24	23.50	2.68	14.17	83.15	5.6	76.81	0.74	0	0	Fine sand

Table A.10: Grain size characterization based on laboratory analysis using a diffraction analyzer.

Borehole	Sampling depth (range)	Depth (avg)	Kmin (m/s)	Kmax (m/s)	Sediment characterization
ML1	5.15-5.4	5.275	2.01E-07	3.01E-07	Medium
ML1	6.15-6.4	6.275	6.93E-07	1.04E-06	Coarse sand
ML1	6.95-7.2	7.075	1.24E-06	1.87E-06	Coarse sand
ML1	12-13	12.5	1.43E-04	2.15E-04	Coarse sand
ML1	14-15	14.5	1.07E-06	1.60E-06	Coarse sand
ML1	20-21	20.5	7.51E-06	1.13E-05	Fine sand
ML1	23-24	23.5	3.65E-06	5.47E-06	Fine sand
JordB	6.6-6.8	6.7	4.40E-07	6.60E-07	Medium sand
JordB	8.2-8.4	8.3	3.13E-08	4.69E-08	Fine sand
JordB	11.4-11.65	11.525	3.98E-06	5.98E-06	Medium sand
JordC	7.1-7.2	7.15	4.40E-07	6.60E-07	Coarse sand
ML2	6-6.4	6.2	1.01E-07	1.52E-07	Medium sand
ML2	8.5-8.75	8.625	1.06E-06	1.58E-06	Coarse sand
ML2	12.25-12.5	12.375	2.23E-06	3.34E-06	Medium sand
ML2	16-17	16.5	5.36E-07	8.05E-07	Fine sand
ML2	20-21	20.5	3.82E-07	5.73E-07	Fine sand
ML2	23-24	23.5	6.41E-07	9.62E-07	Fine sand

Table A.11: Hydraulic conductivities calculated for sediment samples from the saturated zone for boreholes ML1, ML2, JordC and JordB. Hydraulic conductivity was calculated using the Hazen equation with an empirical coefficient of 1 (K_{min}) and 1.5(K_{max}). Grain sediment characterization is also included.

Date	Well	GW level to TOC (m)	Hydraulic head (m.a.s.l.)
13.10.2021	ML1A	6.17	194.393
23.11.2021	ML1A	6.2	194.363
05.04.2022	ML1A	6.58	193.983
13.10.2021	ML1B	6.17	194.373
23.11.2021	ML1B	6.17	194.373
05.04.2022	ML1B	6.54	194.003
13.10.2021	ML1C	6.23	194.362
23.11.2021	ML1C	6.25	194.342
05.04.2022	ML1C	6.65	193.942
22.09.2021	ML2A	7.92	193.508
23.11.2021	ML2A	7.76	193.668
05.04.2022	ML2A	8.18	193.248
22.09.2021	ML2B	7.97	193.492
23.11.2021	ML2B	7.79	193.672
05.04.2022	ML2B	8.21	193.252
22.09.2021	ML2C	7.98	193.448
23.11.2021	ML2C	7.81	193.618
05.04.2022	ML2C	8.22	193.208

Table A.12: Manual groundwater measurements for multiwell ML1 and ML2. Data includes depth measured using a Water Level Meter to the top of casing (TOC) which is below the surface and hydraulic head relative to surface elevation (m.a.s.l.).

Borehole	Avg Depth	Quartz	K-feldspar	Plagioclase	Amphibole	Muscovite	Chlorite	Calcite	Ankerite	Total
ML1	1.5	59	5	20	3	7	5	1	0	100
	2.6	58	6	18	6	6	6		0	100
	3.725	63	5	16	2	9	5	0	0	100
	5.275	63	5	14	2	10	7	0	0	100
	6.275	60	6	15	2	9	6	1	1	100
	7.075	58	6	18	1	10	6	0	0	100
	12.5	60	6	15	2	9	5	3	1	100
	23.5	59	7	14	3	10	4	2	1	100
ML2	2.475	58	6	18	3	11	4	0	0	100
	4.1	59	6	14	3	13	3	0	1	100
	8.625	60	6	14	2	12	5	0	1	100
	12.375	61	4	13	2	11	5	3	1	100
	23.5	57	5	17	3	11	4	2	0	100
JordB	2.875	63	5	16	2	9	4	0	0	100
	4.125	58	7	16	2	10	7	1	1	100
	6.7	61	5	15	2	11	5	0	0	100
	11.525	59	7	17	2	9	5	2	1	100
JordC	2.4	60	6	16	4	11	3	0	0	100
	4.125	69	3	13	1	8	4	0	1	100
	7.15	60	8	16	1	9	4	0	0	100

Table A.13: Results from XRD analysis for boreholes ML1, ML2, JordB and JordC.

Well	Average Depth	Wt. % <125	Crystalline Fe (g/kg dried soil)	Crystalline Mn (g/kg dried soil)	Amorphous Fe (g/kg dried soil)	Amorphous Mn (g/kg dried soil)
ML2	4.1	34.32	6.86E-02	0.00E+00	1.59E+00	1.37E-02
	6.2	27.69	9.58E-01	-5.54E-03	2.73E+00	1.72E-01
	8.63	15.13	6.96E-01	-6.05E-03	1.50E+00	1.04E-01
	12.38	13.95	-1.48E-01	1.40E-03	9.39E-01	2.65E-02
	23.5	60.34	-7.24E-01	1.81E-02	1.25E+00	3.62E-02
ML1	3.73	29.34	1.42E+00	2.05E-02	3.42E+00	2.35E-02
	5.28	26.13	6.87E-01	0.00E+00	2.53E+00	1.57E-02
	6.28	15.58	-1.14E-01	-3.12E-03	4.31E+00	1.40E-02
	7.08	15.07	3.27E-01	-1.51E-03	2.11E+00	3.92E-02
	12.5	2.24	-3.29E-01	-2.22E-02	6.42E-01	3.29E-02
	23.5	17.67	-1.71E-01	4.42E-03	3.48E-01	1.24E-02

Table A.14: Average amorphous and crystalline iron and manganese based on oxalate and DCB extraction, where g/kg dried soil values are based on fraction of bulk sediment less than 125 micrometers.

Listing A.1: Speciation PHREEQC

```
PHASES
Ankerite #emperical equation taken from webmineral.com
   CaFe0.6Mg0.3Mn0.1(CO3)2 = Ca+2 + 0.6Fe+2 + 0.3Mg+2 + 0.1Mn+2 + 2CO3-2
   log_k -7.53 #equilibrium constant of dolomite, neutral mechanism

Pyrochroite #Equation and equilibrium constant from Phreeqc.dat
      Mn(OH)2 + 2 H+ = Mn+2 + 2 H2O
      -log_k 15.2

USER_PUNCH 1
-headings Sample_ref
-start
10 PUNCH Description
-end

SELECTED_OUTPUT 1
-file Speciation_redox.txt
-simulation true
-state true
-solution true
-step  true
-charge_balance
-ionic_strength
-high_prec true
-temp
-percent_error
-alkalinity
-totals Na Mg K Ca N(+5) N(-3) S(6) Cl Mn Fe Si O(0) # mol/kgw, and since
    ↪ density of water is 1kg/l = mol/l
-saturation_indices Goethite Pyrite Pyrochroite Quartz Muscovite Montmor-Ca
    ↪ Montmor-Mg Montmor-Na Fe(OH)3 Ankerite Albite Calcite Clinochlore-14A Mn(
    ↪ OH)2(am) Anorthite Pyrolusite Maximum_Microcline
Hedenbergite Diopside CO2(g) O2(g)

PRINT
-Alkalinity

SOLUTION_SPREAD
-units mmol/liter

Number Description pH pe temp Alkalinity Na Mg K Ca N(5) S(6) Cl Mn Fe N(-3) Si
    ↪ Al
1 ML1_Aug_A 6.76 7.17 12.3 2.10E+00 1.44E+00 1.56E-02 1.46E+00 7.73E-02
    ↪ 0.043544946 1.27E-01 2.06E-02 6.55E-03 3.22E-02 4.88E-03 2.07E-01 #no
    ↪ conv
2 ML1_Aug_B 7.22 4 10 9.90E+00 1.09E+00 4.53E-01 1.66E+00 3.24E+00 4.03194E-05
    ↪ 4.13E-02 3.67E-02 4.01E-02 8.24E-02 3.49E-03 3.45E-01 4.08E-03
3 ML1_Aug_C 6.67 4 10.8 1.70E+00 1.78E-01 1.32E-01 7.42E-02 9.73E-01 4.03194E-05
    ↪  9.35E-02 1.58E-01 2.00E-03 3.76E-03 1.28E-03 1.64E-01 6.67E-03
4 ML1_Nov_A 6.76 7.09 12.3 3.78E+00 1.79E+00 4.42E-03 2.64E+00 7.93E-02
```

```
        ↪ 0.043544946 2.23E-01 1.77E-02 7.55E-03 3.51E-02 4.88E-03 2.07E-01 #no
        ↪ conv
5 ML1_Nov_B 7.22 4 10 7.65E+00 1.09E+00 4.72E-01 1.05E+00 3.24E+00 4.03194E-05
        ↪ 5.80E-01 3.35E-02 3.39E-02 3.08E-01 3.49E-03 3.45E-01 4.08E-03
6 ML1_Nov_C 6.67 4 10.8 1.82E+00 2.00E-01 1.50E-01 6.07E-02 9.81E-01 4.03194E-05
        ↪  2.68E-01 1.46E-01 3.54E-03 1.48E-02 1.28E-03 1.64E-01 6.67E-03
7 ML2_Aug_A 6.22 8.10 9.9 7.00E-01 8.26E-02 6.58E-02 6.91E-02 4.49E-01
        ↪ 0.037093843 5.04E-02 2.37E-02 7.28E-04 7.34E-03 3.60E-04 0.206512257 8.15
        ↪ E-03
8 ML2_Aug_B 6.68 4 9 6.30E+00 2.52E-01 4.94E-01 1.46E-01 2.50E+00 4.03194E-05
        ↪ 5.53E-02 3.38E-02 4.92E-02 2.86E-02 1.61E-03 2.92E-01 #no conv
9 ML2_Aug_C 7.48 4 9.1 3.00E+00 1.78E-01 2.30E-01 6.65E-02 1.30E+00 4.03194E-05
        ↪ 3.82E-02 1.13E-01 2.73E-03 1.72E-02 1.28E-03 2.88E-01 3.30E-02
10 ML2_Nov_A 6.22 8.11 9.9 1.11E+00 7.46E-02 9.08E-02 8.47E-02 6.27E-01
        ↪ 0.037093843 1.84E-01 2.13E-02 2.12E-04 4.22E-03 3.60E-04 0.206512257 8.15
        ↪ E-03
11 ML2_Nov_B 6.68 4 9 5.36E+00 3.21E-01 3.75E-01 1.28E-01 2.21E+00 4.03194E-05
        ↪ 1.74E-01 3.77E-02 5.29E-02 5.71E-02 1.61E-03 2.92E-01 #no conv
12 ML2_Nov_C 7.48 4 9.1 2.83E+00 1.82E-01 2.18E-01 4.70E-02 1.16E+00 4.03194E-05
        ↪  1.30E-01 1.02E-01 2.55E-03 9.15E-03 1.28E-03 2.88E-01 3.30E-02

end
```

Listing A.2: Reaction Filter A PHREEQC

```
PHASES
#Ankerite #emperical equation taken from webmineral.com
#CaFe0.6Mg0.3Mn0.1(CO3)2 = Ca+2 + 0.6Fe+2 + 0.3Mg+2 + 0.1Mn+2 + 2CO3-2

#Deicers
Acetate
CH3COO- + H2O = HCO3- + CH4

Propionate
CH3CH2COO- + 4H2O = CH4 + H+ + 2HCO3- + 3H2

Formate
CHO2- = CO2 + H+ + 2e-

 PRINT
-alkalinity # To see in*.pqo the aq. species that contribute to alkalinity

USER_PUNCH 1
-headings Sample_ref
-start
10 PUNCH Description
-end

SELECTED_OUTPUT 1
-file Deicers_ML1Nov_F1_3.txt
-high_precision true
```

```
-charge_balance
-water density
-ionic_strength
-temp
-percent_error
-alkalinity
-pH
-pe
-totals Na Mg K Ca N(5) S(6) Cl Mn Fe N(-3)


EQUILIBRIUM_PHASES 1
Fe(OH)3 1.09 10 #SI and amount of moles/L
Mn(OH)2(am) -7.83 10 #SI and amount of moles/L
#Pyrolusite -7.44 10
Calcite -1.97 10
Quartz 0.62 10
CO2(g) -1.47 10
END

SOLUTION_SPREAD 1
# 1514 solution density at in situ P & T
-units mmol/kgw

Number Description pH pe temp Alkalinity Na Mg K Ca N(5) S(6) Cl Mn Fe N(-3) Si
1 ML1_Nov_1 6.76 7.09 12.3 3.78E+00 1.79E+00 4.42E-03 2.64E+00 7.93E-02
    ↪ 0.043544946 2.23E-01 1.77E-02 7.55E-03 3.51E-02 4.88E-03 2.07E-01
End

USE solution 1
USE equilibrium_phases 1

REACTION
#Detection levels in BR29 on 12.02.2020
Acetate 1.34E-03
Formate 8.45E-04
Propionate 1.31E-06

#Detection levels in BR29 on 4.4.2019
#Acetate 6.79E-04
#Formate 2.82E-03
#Propionate 3.15E-03

1 mole in 1 steps

END
```

Listing A.3: Reaction Filter B PHREEQC

```
PHASES
```

```
#Deicers
Acetate
CH3COO- + H2O = HCO3- + CH4

Propionate
CH3CH2COO- + 4H2O = CH4 + H+ + 2HCO3- + 3H2

Formate
CHO2- = CO2 + H+ + 2e-

 PRINT
-alkalinity # To see in*.pqo the aq. species that contribute to alkalinity

USER_PUNCH 1
-headings Sample_ref
-start
10 PUNCH Description
-end

SELECTED_OUTPUT 1
-file Deicers_ML1Nov_F2.txt
-high_precision true
-charge_balance
-water density
-ionic_strength
-temp
-percent_error
-alkalinity
-pH
-pe
#-totals Na Mg K Ca N(5) S(6) Cl Mn Fe N(-3)
-mol CO2(g) Calcite Fe(OH)3 Mn(OH)2(am) Quartz

EQUILIBRIUM_PHASES 1
Fe(OH)3 1.55 10 #SI and amount of moles/L
Mn(OH)2(am) -6.51 10 #SI and amount of moles/L
Calcite 0.251 10
Quartz 0.894 10
CO2(g) -1.68 10
END

SOLUTION_SPREAD 1
# 1514 solution density at in situ P & T
-units mmol/kgw

Number Description pH pe temp Alkalinity Na Mg K Ca N(5) S(6) Cl Mn Fe N(-3) Si
    ↪ Al
1 ML1_Nov_2 7.22 4 10 7.65E+00 1.09E+00 4.72E-01 1.05E+00 3.24E+00 1.14E-02 5.80
    ↪ E-01 3.35E-02 3.39E-02 3.08E-01 3.49E-03 3.45E-01 4.08E-03
End
```

```
USE solution 1
USE equilibrium_phases 1

REACTION
#Detection levels in BR29 on 12.02.2020
#Acetate 1.34E-03
#Formate 8.45E-04
#Propionate 1.31E-06

#Detection levels in BR29 on 4.4.2019
Acetate 6.79E-04
Formate 2.82E-03
Propionate 3.15E-03

1 mole in 1 steps

END
```

Bibliography

P. Aagaard, K. Tuttle, N.O. Kitterød, H French, and K. Rudolph-Lund. The moreppen field station at gardermoen, s.e. norway. a research station for geophysical, geological and hydrological studies. In P. Aagaard and K.J. Tuttle, editors, *'Proceedings to the Jens-Olaf Englund Seminar Protection of Groundwater Resources against Contaminants': 16-18 September 1996, Quality Airport Hotel, Gardermoen*, chapter 1, pages 1–8. 1996.

University of Maryland AgroEcoLab. Protocol for oxalate and total al and fe extraction in soils, 2018. URL https://static1.squarespace.com/static/5ffd807f8c82102fb895216b/t/600077cadf80a433129ec815/1610643402394/AgroEcoLabMethod_Oxalate%26TotalAl%26FeextractionSOIL_13August2018.pdf.

C Anthony J Appelo and Dieke Postma. *Geochemistry, groundwater and pollution*. CRC press, 2004.

Hamidi A Aziz and Paul G Smith. The influence of ph and coarse media on manganese precipitation from water. *Water Research*, 26(6):853–855, 1992.

Lieve Balcaen, Eduardo Bolea-Fernandez, Martín Resano, and Frank Vanhaecke. Inductively coupled plasma–tandem mass spectrometry (icp-ms/ms): A powerful and universal tool for the interference-free determination of (ultra) trace elements–a tutorial review. *Analytica chimica acta*, 894:7–19, 2015.

Leif Basberg, Peter Engesgaard, and Atle Dagestad. Geochemical modelling of natural geo-/hydrochemical stratification dominated by pyrite ocidation and calcite dissolution in a glaciofluvial quaternary deposit, gardermoen, norway. 1998.

Simon J Blott and Kenneth Pye. Gradistat: a grain size distribution and statistics package for the analysis of unconsolidated sediments. *Earth surface processes and Landforms*, 26(11):1237–1248, 2001.

Valter Boero and U Schwertmann. Iron oxide mineralogy of terra rossa and its genetic implications. *Geoderma*, 44(4):319–327, 1989.

Gijs Breedveld. Degradation capacity in groundwater at gardermoen. Technical Report 2001344-1, NGI, 2001.

Peter Brouwer. Theory of xrf. *Almelo, Netherlands: PANalytical BV*, 2006.

R Buamah, B Petrusevski, D De Ridder, TSCM Van de Wetering, and JC Shippers. Manganese removal in groundwater treatment: practice, problems and probable solutions. *Water Science and Technology: Water Supply*, 9(1):89–98, 2009.

Andrei A Bunaciu, Elena Gabriela UdriŞTioiu, and Hassan Y Aboul-Enein. X-ray diffraction: instrumentation and applications. *Critical reviews in analytical chemistry*, 45(4):289–299, 2015.

Francis H Chapelle. *Ground-water microbiology and geochemistry*. John Wiley & Sons, 2000.

Claudio Colombo, Giuseppe Palumbo, Ji-Zheng He, Roberto Pinton, and Stefano Cesco. Review on iron availability in soil: interaction of fe minerals, plants, and microbes. *Journal of soils and sediments*, 14(3):538–548, 2014.

Rochelle M Cornell, Udo Schwertmann, et al. *The iron oxides: structure, properties, reactions, occurrences, and uses*, volume 2. Wiley-vch Weinheim, 2003.

Charles Curtis. Mineralogical consequences of organic matter degradation in sediments: inorganic/organic diagenesis. In *Marine clastic sedimentology*, pages 108–123. Springer, 1987.

Atle Dagestad. *In situ luftinjeksjon i grunnvannssonen som opprensningstiltak i akviferen ved Gardermoen, Sørøst Norge*. PhD thesis, Norwegian University of Science and Technology, 1999.

Arlene K Darke and Mark R Walbridge. Estimating non-crystalline and crystalline aluminum and iron by selective dissolution in a riparian forest soil. *Communications in Soil Science and Plant Analysis*, 25(11-12):2089–2101, 1994.

Braja M Das and Nagaratnam Sivakugan. *Fundamentals of geotechnical engineering*. Cengage Learning, 2016.

J Di-Ruggiero and AM Gounot. Microbial manganese reduction mediated by bacterial strains isolated from aquifer sediments. *Microbial ecology*, 20(1):53–63, 1990.

C Di Stefano, V Ferro, and S Mirabile. Comparison between grain-size analyses using laser diffraction and sedimentation methods. *Biosystems engineering*, 106(2):205–215, 2010.

Joe Boris Dixon, Sterling Barg Weed, and RL Parpitt. Minerals in soil environments. *Soil Science*, 150(2):562, 1990.

Nicola Doebelin and Reinhard Kleeberg. Profex: a graphical user interface for the rietveld refinement program bgmn. *Journal of applied crystallography*, 48(5):1573–1580, 2015.

Jeffrey Evans, Daniel Ruffing, and David Elton. *Fundamentals of Ground Improvement Engineering*. CRC Press, 2021.

Anne Kristine French, Helen K. og Sœvik. Jern- og mangankonsentrasjoner i grunnvannet på gardermoen - mulige årsaker og langtidseffekter. Technical Report 101/2005, Jordforsk, 2005.

Av Helen K French. Transport and degradation of de-icing chemicals in the unsaturated zone–15 years of research at gardermoen. *Vann*, 43(4), 2008.

Helen K French and Sjoerd EATM van der Zee. Improved management of winter operations to limit subsurface contamination with degradable deicing chemicals in cold regions. *Environmental science and pollution research*, 21(15):8897–8913, 2014.

HK French, SEATM Van der Zee, and A Leijnse. Transport and degradation of propyleneglycol and potassium acetate in the unsaturated zone. *Journal of contaminant hydrology*, 49(1-2):23–48, 2001.

HK French, H-O Eggestad, J Øvstedal, and P-E Jahren. Climate conditions and consequences for de-icing operations as exemplified by the situation on a motorway and airport at gardermoen, norway. *Hydrology Research*, 41(3-4):269–281, 2010.

James S Fritz. Ion chromatography. *Analytical Chemistry*, 59(4):335A–344A, 1987.

Dirk Goossens. Techniques to measure grain-size distributions of loamy sediments: a comparative study of ten instruments for wet analysis. *Sedimentology*, 55(1):65–96, 2008.

Anne-Monique Gounot. Microbial oxidation and reduction of manganese: consequences in groundwater and applications. *FEMS Microbiology reviews*, 14(4):339–349, 1994.

K. Grotthing. private communication, May 2022.

Deeksha Grover. *Genesis of iron oxides in unsaturated porous media*. Oregon State University, 2010.

Mona C. Hansen, Gijs Breedveld, and Helen French. Vurdering av endringer i grunnvannskjemi på osl fra 1999 til 2019. Technical Report 201905083-01-R, Norges Geotekniske Institutt, 2020a.

Mona C. Hansen, Helen French, and Joris Stuurop. Modellering av grunnvannstrœmning i br29 området. Technical Report 201905083-02-R, Norges Geotekniske Institutt, 2020b.

Allen Hazen. Some physical properties of sand and gravel with special reference to their use in filtration. *24th Ann, Rep., Mass. State Board of Health, Boston, 1892*, 1892.

Pasi P Hellstén, Jani M Salminen, Kirsten S Jørgensen, and Taina H Nystén. Use of potassium formate in road winter deicing can reduce groundwater deterioration. *Environmental science & technology*, 39(13):5095–5100, 2005.

Gorm Heron, Catherine Crouzet, Alain CM Bourg, and Thomas H Christensen. Speciation of fe (ii) and fe (iii) in contaminated aquifer sediments using chemical extraction techniques. *Environmental science & technology*, 28(9):1698–1705, 1994.

T. Holm. Groundwater quality at gardermoen. evaluation of water quality from an environmental monitoring programme. Technical Report AN-R-0035-E02, Oslo Airport, 2000.

JR Howell. Effects of microbial iron oxide reduction on ph and alkalinity in anaerobic bicarbonate-buffered media: implications for metal mobility. *Mineralogical Magazine*, 62(2): 657–658, 1998.

Christopher G Hubbard, L Jared West, Katherine Morris, Bernd Kulessa, Diana Brookshaw, Jonathan R Lloyd, and Samuel Shaw. In search of experimental evidence for the biogeobattery. *Journal of Geophysical Research: Biogeosciences*, 116(G4), 2011.

Rasmus Jakobsen and Dieke Postma. Redox zoning, rates of sulfate reduction and interactions with fe-reduction and methanogenesis in a shallow sandy aquifer, rømø, denmark. *Geochimica et Cosmochimica Acta*, 63(1):137–151, 1999.

Dorthe L Jensen, Jens K Boddum, Sabine Redemann, and Thomas H Christensen. Speciation of dissolved iron (ii) and manganese (ii) in a groundwater pollution plume. *Environmental science & technology*, 32(18):2657–2664, 1998.

Per Jørgensen and Svein Roar Østmo. Hydrogeology in the romerike area, southern norway. 1990.

Per Jørgensen, Svein Roar Østmo, and Arne O Stuanes. Aqueous geochemistry of the romerike area, southern norway. 1990.

Hassan Khozyem, Ali Hamdan, Abdel Aziz Tantawy, Ashraf Emam, and Eman Elbadry. Distribution and origin of iron and manganese in groundwater: case study, balat-teneida area, el-dakhla basin, egypt. *Arabian Journal of Geosciences*, 12(16):1–16, 2019.

Nils-Otto Kitterød. Focused flow in the unsaturated zone after surface ponding of snowmelt. *Cold regions science and technology*, 53(1):42–55, 2008.

P. I. Kraft and Roger Roseth. Rensing av avisingsmidler i jord - en sammenstilling av jordforsknotatene 14 - 32/99 til osl, gardermoen. Technical report, Norsk institutt for bioøkonomi, 1999.

Ole Larsen, Dieke Postma, and Rasmus Jakobsen. The reactivity of iron oxides towards reductive dissolution with ascorbic acid in a shallow sandy aquifer (rømø, denmark). *Geochimica et Cosmochimica Acta*, 70(19):4827–4835, 2006.

Fei Li, Liangquan Ge, Zhuoyao Tang, Yi Chen, and Jing Wang. Recent developments on xrf spectra evaluation. *Applied Spectroscopy Reviews*, 55(4):263–287, 2020.

J-L Loizeau, Didier Arbouille, Sergio Santiago, and J-P Vernet. Evaluation of a wide range laser diffraction grain size analyser for use with sediments. *Sedimentology*, 41(2):353–361, 1994.

Oddvar Longva. *Ullensaker 1915 II. Beskrivelse Til Kvartaergeologisk Kart M 1: 50 000 (med Fargetrykt Kart).* Norges Geologiske Undersøkelse, 1987.

Oddvar Longva and Morten K Thoresen. The age of the hauerseter delta. *Norsk geologisk tidsskrift*, 69:131–134, 1989.

Ida Lønne. Sedimentary facies and depositional architecture of ice-contact glaciomarine systems. *Sedimentary Geology*, 98(1-4):13–43, 1995.

Derek R Lovley. Microbial reduction of iron, manganese, and other metals. *Adv. Agron.*, 54: 175–231, 1995.

Derek R Lovley. Microbial fe (iii) reduction in subsurface environments. *FEMS Microbiology Reviews*, 20(3-4):305–313, 1997a.

Derek R Lovley and Steve Goodwin. Hydrogen concentrations as an indicator of the predominant terminal electron-accepting reactions in aquatic sediments. *Geochimica et cosmochimica acta*, 52(12):2993–3003, 1988.

Derek R Lovley and Elizabeth JP Phillips. Organic matter mineralization with reduction of ferric iron in anaerobic sediments. *Applied and environmental microbiology*, 51(4):683–689, 1986.

Derek R Lovley and Elizabeth JP Phillips. Manganese inhibition of microbial iron reduction in anaerobic sediments. *Geomicrobiology Journal*, 6(3-4):145–155, 1988.

DR Lovley. Potential for anaerobic bioremediation of btex in petroleum-contaminated aquifers. *Journal of Industrial Microbiology and Biotechnology*, 18(2-3):75–81, 1997b.

Scot T Martin. Precipitation and dissolution of iron and manganese oxides. *Environmental catalysis*, 1:61–82, 2005.

T Matsunaga, G Karametaxas, HR Von Gunten, and PC Lichtner. Redox chemistry of iron and manganese minerals in river-recharged aquifers: A model interpretation of a column experiment. *Geochimica et Cosmochimica Acta*, 57(8):1691–1704, 1993.

Carl O Moses, D Kirk Nordstrom, Janet S Herman, and Aaron L Mills. Aqueous pyrite oxidation by dissolved oxygen and by ferric iron. *Geochimica et Cosmochimica Acta*, 51(6): 1561–1571, 1987.

William D Nesse. *Introduction to mineralogy*. Number 549 NES. Oxford Univ. Press, 2012.

Geological Survey of Norway (NGU). Datasett og nedlasting, 2021. URL https://www.ngu.no/emne/datasett-og-nedlasting.

Yasmina Ourradi. In-situ removal of iron and manganese from groundwater. Master's thesis, 2021.

James L Palandri and Yousif K Kharaka. A compilation of rate parameters of water-mineral interaction kinetics for application to geochemical modeling. Technical report, Geological Survey Menlo Park CA, 2004.

D. L. Parkhurst and C. A. J. Appelo. *Description of input and examples for PHREEQC version 3–A computer program for speciation, batch-reaction, one-dimensional transport, and inverse geochemical calculations*, 2013. URL http://pubs.usgs.gov/tm/06/a43.

BM Petrunic, KTB MacQuarrie, and TA Al. Reductive dissolution of mn oxides in river-recharged aquifers: a laboratory column study. *Journal of Hydrology*, 301(1-4):163–181, 2005.

Jeffrey E Post. Manganese oxide minerals: Crystal structures and economic and environmental significance. *Proceedings of the National Academy of Sciences*, 96(7):3447–3454, 1999.

Pu Qian. On-line computer aided multi-component analysis using organic elemental analyzer. *Computers & Chemistry*, 24(6):627–633, 2000.

Christina K Remucal and Matthew Ginder-Vogel. A critical review of the reactivity of manganese oxides with organic contaminants. *Environmental Science: Processes & Impacts*, 16(6):1247–1266, 2014.

Thilo Rennert, Jan Dietel, Stefan Heilek, Reiner Dohrmann, and Tim Mansfeldt. Assessing poorly crystalline and mineral-organic species by extracting al, fe, mn, and si using (citrate-) ascorbate and oxalate. *Geoderma*, 397:115095, 2021.

I Reyes and J Torrent. Citrate-ascorbate as a highly selective extractant for poorly crystalline iron oxides. *Soil Science Society of America Journal*, 61(6):1647–1654, 1997.

Eric E Roden and John M Zachara. Microbial reduction of crystalline iron (iii) oxides: influence of oxide surface area and potential for cell growth. *Environmental Science & Technology*, 30(5):1618–1628, 1996.

T Schoenberg, S Veltman, and M Switzenbaum. Kinetics of anaerobic degradation of glycol-based type i aircraft deicing fluids. *Biodegradation*, 12(1):59–67, 2001.

U Schwertmann. Differenzierung der eisenoxide des bodens durch extraktion mit ammoniumoxalat-lösung. *Zeitschrift für Pflanzenernährung, Düngung, Bodenkunde*, 105(3):194–202, 1964.

UTRM Schwertmann and Reginald M Taylor. Iron oxides. *Minerals in soil environments*, 1:379–438, 1989.

Michael John Singer and Peter Janitzky. *Field and laboratory procedures used in a soil chronosequence study*. Number 1648. US Government Printing Office, 1986.

Britha Skarstad. Undersökelse av lösmassene på moreppen, gardermoen- fysisk sammenset-ning, mineralogi og vannkjemi. Technical report, Hovedoppgave ved Institute for jord og vannfag. Norges LandbrukshÖskole, 1996.

AK Søvik and P Aagaard. Spatial variability of a solid porous framework with regard to chemical and physical properties. *Geoderma*, 113(1-2):47–76, 2003.

Claudette Spiteri, Pierre Regnier, Caroline P Slomp, and Matthew A Charette. ph-dependent iron oxide precipitation in a subterranean estuary. *Journal of geochemical exploration*, 88(1-3):399–403, 2006.

Anja Sundal. Chemical characteristics of deep groundwater in the gardermoen aquifer: Controlling processes and residence times. Master's thesis, 2006.

Anja Sundal, Matthias S Brennwald, Per Aagaard, and Rolf Kipfer. Noble gas composition and 3h/3he groundwater ages in the gardermoen aquifer, norway: Improved understanding of flow dynamics as a tool for water management. *Science of The Total Environment*, 660:1219–1231, 2019.

Olof Tamm. Eine methode zur bestim mung der anorganischen komponenten des gelkomplexes im boden. *Meddel. Statens Skogsforsoksanst.*, 19:385–404, 1922.

K. Tuttle. *Sedimentological and hydrogeological characterisation of a raised icecontact delta - the Preboreal deltacomplex at Gardermoen, southeastern Norway*. PhD thesis, University of Oslo, Blindern, 1997.

Kevin J Tuttle, Svein Roar Øustmo, and Bj örn G Andersen. Quantitative study of the distributary braidplain of the preboreal ice-contact gardermoen delta complex, southeastern norway. *Boreas*, 26(2):141–156, 1997.

S Veltman, T Schoenberg, and MS Switzenbaum. Alcohol and acid formation during the anaerobic decomposition of propylene glycol under methanogenic conditions. *Biodegradation*, 9(2):113–118, 1998.

Ann L Walker. The effects of magnetite on oxalate-and dithionite-extractable iron. *Soil Science Society of America Journal*, 47(5):1022–1026, 1983.

Bente Wejden and Jarl Øvstedal. Contamination and degradation of de-icing chemicals in the unsaturated and saturated zones at oslo airport, gardermoen, norway. In *Urban Groundwater Management and Sustainability*, pages 205–218. Springer, 2006.

Terry R West and Abdul Shakoor. *Geology applied to engineering*. Waveland Press, 2018.

Scott C Wilschefski and Matthew R Baxter. Inductively coupled plasma mass spectrometry: introduction to analytical aspects. *The Clinical Biochemist Reviews*, 40(3):115, 2019.

Weilie Zhou, Robert Apkarian, Zhong Lin Wang, and David Joy. Fundamentals of scanning electron microscopy (sem). In *Scanning microscopy for nanotechnology*, pages 1–40. Springer, 2006.